

DEVELOPING OPTICAL ALGORITHMS TO ADVANCE AIRBORNE MEASUREMENTS
OF AEROSOL AND METEOROLOGICAL PROPERTIES

by

Sanja Dmitrovic

Copyright © Sanja Dmitrovic 2024

A Dissertation Submitted to the Faculty of the

JAMES C. WYANT COLLEGE OF OPTICAL SCIENCES

In Partial Fulfillment of the Requirements

For the Degree of

DOCTOR OF PHILOSOPHY


In the Graduate College

THE UNIVERSITY OF ARIZONA

2024

THE UNIVERSITY OF ARIZONA
GRADUATE COLLEGE

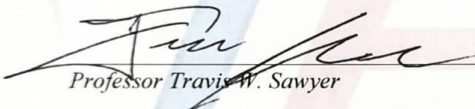
As members of the Dissertation Committee, we certify that we have read the dissertation prepared by **Sanja Dmitrovic**, titled *Developing Optical Algorithms to Advance Airborne Measurements of Aerosol and Meteorological Properties* and recommend that it be accepted as fulfilling the dissertation requirement for the Degree of Doctor of Philosophy.



Professor Armin Sorooshian Date: 4/26/2024



Professor Thomas D. Milster Date: 4/26/2024



Professor Travis W. Sawyer Date: 4/26/2024

Final approval and acceptance of this dissertation is contingent upon the candidate's submission of the final copies of the dissertation to the Graduate College.

I hereby certify that I have read this dissertation prepared under my direction and recommend that it be accepted as fulfilling the dissertation requirement.



Professor Armin Sorooshian
Dissertation Committee Chair
Wyant College of Optical Sciences Date: 4/26/2024

ACKNOWLEDGEMENTS

I would first like to thank Armin Sorooshian for supporting me through this Ph.D. both professionally and personally. His guidance and mentorship allowed me to persevere through this degree and become a more curious and independent researcher. He has also supported me when times became tough, which has helped me become a stronger person. This degree has been quite a journey, but Armin has always picked me back up on my worst days and helped me get to the finish line.

I also want to express my gratitude to Tom Milster who was my MS advisor and now serves on my dissertation committee. He taught me the rigorous fundamentals of optics and inspired me to pursue a doctorate. His lessons on both optics and life have become an invaluable part of my journey.

I next want to show gratitude to my collaborators at the NASA Langley Research Center. Not only did they teach me a lot about science, but also have always welcomed and supported me on a personal level. I really enjoyed my visit over to the center and hope to come again someday.

I would also like to thank my research group for their friendship and support. My sense of community with this group is what made the Ph.D. not just a job, but a journey with a lot of laughter and enjoyment. I want to congratulate those who are graduating with me and wish the remaining members success in finishing their degrees.

I am also grateful to my friends for lifting me up and making my time in graduate school an overall happy experience. Hard work needs to be balanced with shenanigans, which my friends definitely helped me with. Now that I'm finally done with school, I hope I can visit them more often now.

Next, I want to thank Claire for always being by my side. Some of my happiest memories have been with you (i.e., Cedar Fun Center) and I hope we make many more when we move to Las Vegas. You inspire me to be a better person every day and am very lucky to have met you.

Lastly, I want to thank my parents, Ruza and Branko, for staying by my side during this whole journey. Since day one, they did everything in their power to help me achieve my dreams. When I was in second grade, I said I would go to NASA to become an astrophysicist or an aerospace engineer. I did not end up becoming either of those things, but I worked with NASA Langley

throughout my Ph.D. and will now be a software engineer with NASA Goddard after graduation. Without the love and support of my parents, I would've never accomplished these dreams. I wish my father could've been here to celebrate these achievements, but I'm sure he is watching over me every step of the way. One day, I will tell him all about it. Until then, Tat.

DEDICATION

To my parents, Claire, and my bebe bois and girls.

Table of Contents

ABSTRACT	8
CHAPTER 1: INTRODUCTION	10
1.1 WHAT IS THE MARINE ATMOSPHERIC BOUNDARY LAYER?	10
1.2 NASA ACTIVATE MISSION DESCRIPTION	12
1.2.1 HU-25 FALCON INSTRUMENTATION	14
1.2.2 KING AIR INSTRUMENTATION	19
1.3 EXPLANATION OF DISSERTATION FORMAT	24
CHAPTER 2: STUDY DESCRIPTIONS	25
2.1 HSRL-2 RETRIEVALS OF OCEAN SURFACE WIND SPEED	25
2.2 EXTERNAL CLOSURE OF IN-SITU AND REMOTE SENSING AMBIENT AEROSOL DATA	27
APPENDIX A: HIGH SPECTRAL RESOLUTION LIDAR – GENERATION 2 (HSRL-2) RETRIEVALS OF OCEAN SURFACE WIND SPEED: METHODOLOGY AND EVALUATION	29
1 Introduction	31
2 Methods	32
2.1 ACTIVATE Mission Description	32
2.2 Dropsondes	34
2.3 HSRL-2 Instrument Description	34
2.4 HSRL-2 Surface Wind Speed Retrieval Method	35
2.5 Collocation and Statistical Procedures	41
3 Results and Discussion	43
3.1 Case Studies	43
3.1.1 Research Flight 29 on 28 August 2020	43
3.1.2 Research Flight 14 on 1 March 2020	44
3.2 HSRL-2 – Dropsonde Comparisons	45
4. Conclusions	51
Data Availability	52
Author Contribution	52
Competing Interests	53
Disclaimer	53
Acknowledgements	53
Financial support	53
References	53

APPENDIX B: CLOSING THE GAP BETWEEN IN-SITU AND REMOTELY SENSED AEROSOL PARTICLE PROPERTIES	61
1 Introduction.....	62
2 Methods.....	64
2.1 ACTIVATE Mission Description	64
2.2 Remote Sensing Instrument Descriptions	65
2.3 In-Situ Instrument Descriptions	66
2.4 In Situ Aerosol Retrieval Algorithm (ISARA) Description	68
2.5 Collocation Process and Statistical Validation	72
3 Results and Discussion.....	73
4 Conclusions.....	77
Code Availability	77
Data Availability.....	78
Author Contribution.....	78
Competing Interests.....	78
Disclaimer	78
Acknowledgements	78
References	78
APPENDIX C: AUTHOR’S PUBLICATIONS.....	84
DISSERTATION REFERENCES.....	87

ABSTRACT

The marine atmospheric boundary layer (MABL), the layer between the ocean and free troposphere, hosts a suite of important atmospheric processes such as heat and temperature flux, gas exchange of carbon dioxide and water vapor, cloud evolution, and aerosol particle transport. To measure these complex processes and provide a complete picture of the MABL, organizations such as the National Aeronautics and Space Administration (NASA), the National Oceanic and Atmospheric Administration (NOAA), and the Office of Naval Research (ONR) conduct airborne field campaigns that use a multitude of in-situ and remote sensing platforms. This dissertation introduces two studies that aim to improve airborne measurements of 1) ocean surface wind speeds and 2) atmospheric aerosol particles. Both of these studies focus on the in-situ and remote sensing instruments used in NASA's Aerosol Cloud Meteorology Interactions over the western Atlantic Experiment (ACTIVATE) field campaign that took place from 2020 – 2022.

The first study of this dissertation introduces a new 10 m ocean surface wind speed product from the High Spectral Resolution Lidar – generation 2 (HSRL-2) developed at the NASA Langley Research Center (LaRC) and evaluates it using coincident dropsonde surface wind speed data collected during the NASA ACTIVATE field campaign. The HSRL-2 directly retrieves vertically resolved aerosol backscatter and extinction profiles without relying on an assumed lidar ratio or other external aerosol constraints, enabling accurate estimates of the attenuation of the atmosphere and direct retrieval of surface wind speed through probing the variance of ocean wave slopes (i.e., wave-slope variance). The important findings from this study are 1) HSRL-2 surface wind speed retrieval accuracy is $0.15 \text{ m s}^{-1} \pm 1.80 \text{ m s}^{-1}$, 2) dropsonde surface wind speed measurements most closely match with the Hu et al. (2008) wind speed-wave-slope variance model for surface wind speeds below 7 m s^{-1} , showing that this model is best to use for HSRL-2 retrievals, 3) the fine horizontal spatial resolution of the HSRL-2 (0.5 s or $\sim 75 \text{ m}$ along track) provides near-continuous profiles of surface wind speed over time, allowing for the instrument to probe MABL processes such as sea surface temperature (SST) dynamics and cloud evolution, and 4) the HSRL-2 can detect the ocean surface in broken cloud scenes, showing that the retrievals are not limited to aerosol-free conditions, thus enabling substantial retrievals in scenes with high cloud fraction over the northwest Atlantic.

The second study focuses on improving airborne measurements of atmospheric aerosol particles through evaluation of the following microphysical and optical property data: aerosol number concentration (N_a), aerosol effective radius (r_{eff}), aerosol extinction at 532 nm (ϵ_{532nm}), and single scattering albedo (SSA) at 555 nm. A rigorous comparison analysis between ACTIVATE's in-situ and remote sensing instruments (i.e., external closure) is conducted to see if measurements of the aforementioned aerosol data agree with one another. It is difficult to perform closure between these two instrument platforms because in-situ instruments provide dry ($\sim 20\%$ relative humidity (RH)) aerosol measurements while remote sensors retrieve these data at ambient RH conditions. Also, in-situ instruments can only sample fine-mode particles due to the sampling inlet of the aircraft only allowing particles with diameters $< 5 \mu\text{m}$ to pass through; this is problematic for intercomparisons with remote sensors that retrieve information about particles extending into coarser sizes. To overcome these limitations, the In Situ Aerosol Retrieval Algorithm (ISARA) is introduced, a forward optical algorithm that adjusts dry in-situ aerosol data into ambient data for both fine- and coarse-mode particles. This study demonstrates that for marine environments, appropriate a priori assumptions for coarse-mode aerosol allow for consistent closure between in-situ measurements and lidar and polarimetric retrievals of total (fine- + coarse-mode) aerosol properties. The second main finding is that it is possible to systematically close in-situ and polarimeter aerosol data, which has not been shown in the literature to date.

Overall, it is hoped that optical technologies and algorithms can continue to advance our knowledge of the atmosphere by providing state-of-the-art measurements of critical MABL parameters.

CHAPTER 1: INTRODUCTION

1.1 WHAT IS THE MARINE ATMOSPHERIC BOUNDARY LAYER?

The marine atmospheric boundary layer (MABL) is the layer of the free troposphere in direct contact with the earth's ocean (Palm et al., 1998). This interface is critical to study because it hosts important processes such as transfer of sensible and latent heat, exchange of gases such as carbon dioxide and water vapor, transport of natural and anthropogenic (human-made) aerosol particles, and formation of clouds and precipitation (Neukermans et al., 2018) (Fig. 1).

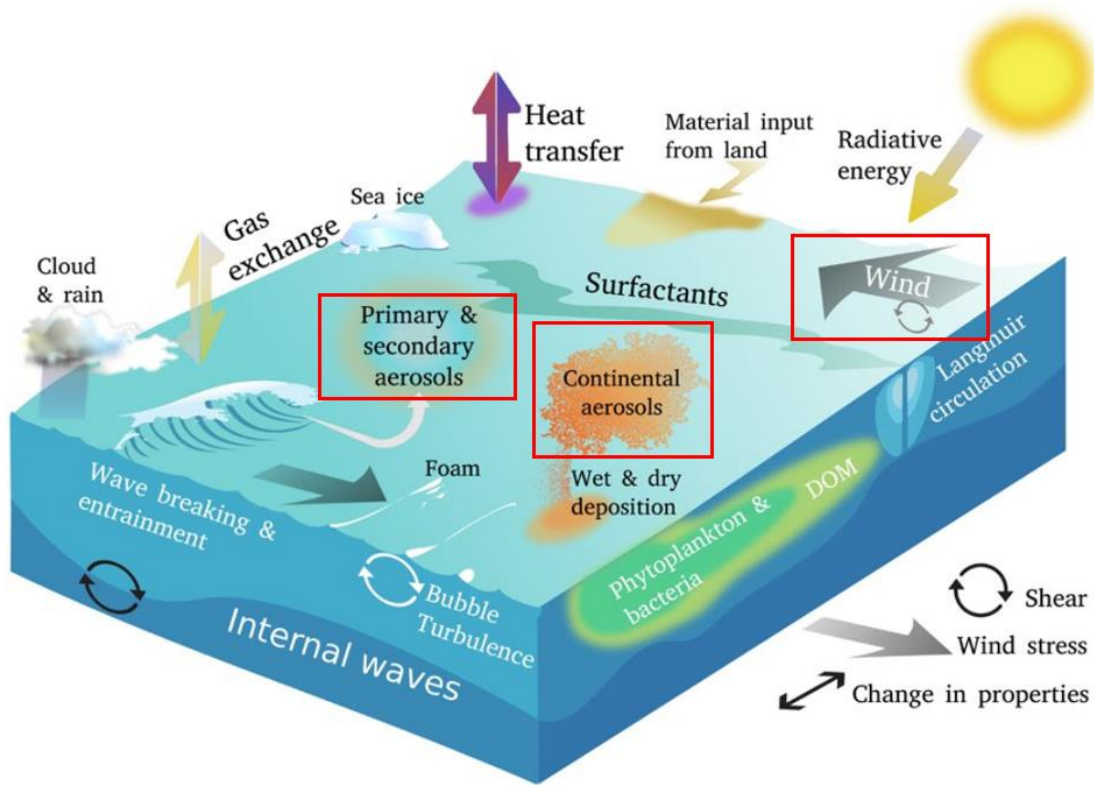


Figure 1: Summary of interactions between ocean and free troposphere at MABL interface (adapted from Neukermans et al. (2018)). Red boxes indicate atmospheric variables relevant to this dissertation.

A combination of model predictions from numerical weather prediction (NWP) models and real observations (i.e., instrument measurements) is used to rigorously characterize these various MABL interactions and consequently understand large-scale phenomena such as climate change and weather across the globe (Carvalho, 2019; Paiva et al., 2021). However, measuring these atmospheric parameters can be difficult due to the non-linear, turbulent nature of the MABL and the host of MABL processes occurring at differing spatial and temporal scales from one another (Garbe et al., 2014). Also, MABL interactions cannot be measured in isolation because these

atmospheric processes are coupled with one another and therefore make up a larger, complex atmospheric system (Fernández et al., 2023). Due to these complexities, airborne field campaigns hosted by organizations such as the National Aeronautics and Space Administration (NASA), the National Oceanic and Atmospheric Administration (NOAA), and the Office of Naval Research (ONR) deploy diverse suites of in-situ and remote sensing instruments that attempt to resolve these various spatiotemporal scales and probe the feedback systems between coupled atmospheric processes (Neukermans et al., 2018). These measurements are then assimilated into the NWP models mentioned previously to improve global projections of the state of the MABL.

This dissertation focuses on measuring 1) horizontal surface winds (i.e., surface winds hereafter) and 2) aerosol particles (red boxes in Fig. 1). The first study of this dissertation describes the use of the High Spectral Resolution Lidar (HSRL) technique to make high spatial and temporal resolution retrievals of surface wind speeds. Surface winds through their speeds are crucial to measure because they are one of the main drivers of MABL transport mechanisms (Garbe et al., 2014). For example, surface wind speeds (standardly measured at 10 m above sea level) are a critical parameter for modelling sea salt aerosol emissions from the ocean surface (Reid et al., 2001) and in studies of cloud microphysics (Colón-Robles et al., 2006) because these winds drive increases in sea salt particle concentrations and activation of these particles into cloud droplets. Surface wind speed is also the main variable used to calculate gas transfer velocity, which describes the velocity of gas entering and exiting the MABL (Prytherch and Yelland, 2021). This study focuses on lidar surface wind speed retrievals since they have the advantage of providing higher spatial resolution measurements compared to microwave instruments such as scatterometers (Neukermans et al., 2018). However, the main limitation of lidar surface wind retrievals is that they have difficulty accounting for atmospheric attenuation by aerosols (described in Chapter 2.1 and Appendix A).

The second study details how to improve measurements of various microphysical and optical properties of atmospheric aerosol particles. Atmospheric aerosols, technically defined as a suspension of solid particles or liquid droplets in air, are important because these particles scatter and absorb solar radiation, significantly affecting the Earth's radiation budget and ultimately the state of its climate (Papadimas et al., 2012). Aerosol particles also alter climate via cloud formation because they act as the seeds (called cloud condensation nuclei, CCN) by which cloud droplets (and consequently clouds) are formed (Twomey et al., 1984). Although numerous studies have

investigated the role of aerosols in MABL processes, aerosol-radiation and aerosol-cloud interactions are a major source of uncertainty in projections of future changes in Earth's radiative forcing and therefore the state of climate change (Field et al., 2014). The reason for this uncertainty is that aerosol particles are diverse in size and shape. They range from 1 nm to even 100 μm and can exist as single particles or aggregates of various aerosol species (Wiedensohler et al., 2013). Smoke aerosol tends to be spherical in shape while dry sea salt and dust can be cubes or other irregular shapes (Gui et al., 2022; Kahnert and Kanngießer, 2023). Although there have been significant advancements in measuring these diverse particles, there is still difficulty resolving all of these complexities leading to inaccuracies in the data.

The two studies in this dissertation aim to solve some of these complexities and ultimately improve airborne in-situ and remote sensing measurements of surface wind speed and aerosol particle properties.

1.2 NASA ACTIVATE MISSION DESCRIPTION

Both studies in this dissertation rely on surface wind speed data and aerosol data from the NASA Aerosol Cloud meTeorology Interactions oVer the western ATlantic Experiment (ACTIVATE) field campaign. Two aircraft deployed from the NASA Langley Research Center (LaRC) in Hampton, VA flew in spatial and temporal coordination to survey aerosol-cloud-meteorology interactions in the MABL over the Western North Atlantic region (Sorooshian et al., 2023). For most of the flights, a “stacked” flight strategy called a statistical survey was developed, where a low-flying (< 5 km) HU-25 Falcon aircraft measured aerosol, cloud, and meteorological properties directly (in-situ) in and just above the MABL while a high-flying (~ 9 km) King Air aircraft provided simultaneous remote sensing retrievals and dropsonde measurements of these same properties (Fig. 2) (Sorooshian et al., 2023). This strategy is used to provide complete column information of these various atmospheric parameters throughout the troposphere (Sorooshian et al., 2023). Descriptions of the Falcon and King Air instruments relevant to this dissertation are provided in Chapters 1.3 and 1.4.

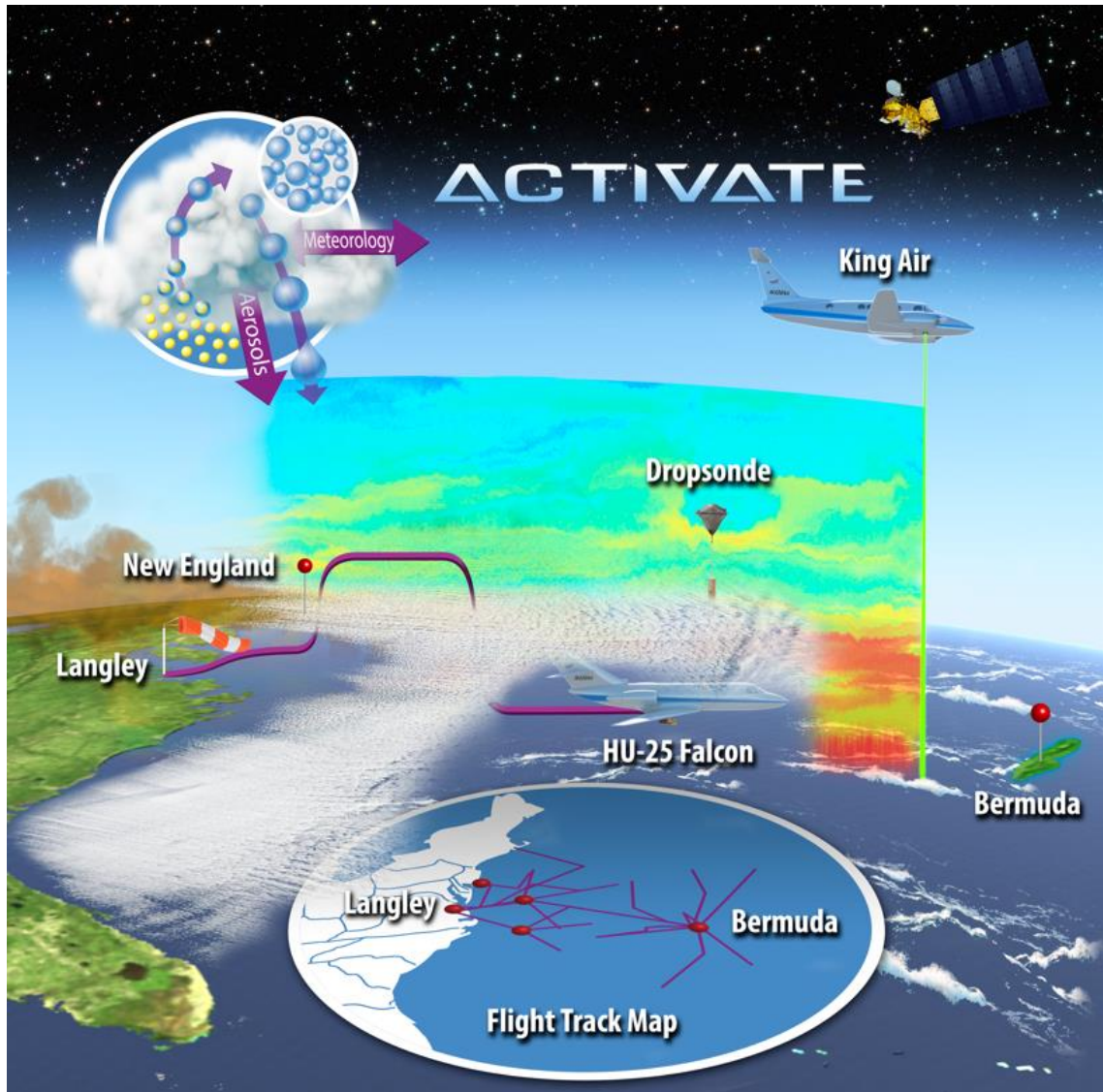


Figure 2: Visualization of NASA ACTIVATE's joint-flight strategy.

In total, ACTIVATE featured 179 flights total with 162 of them being the joint statistical surveys over six deployments. The six deployments occurred during the following dates:

1. 14 February – 12 March 2020
2. 13 August – 30 September 2020
3. 27 January – 2 April 2021
4. 13 May – 30 June 2021
5. 30 November 2021 – 29 March 2022
6. 3 May 2022 – 18 June 2022.

Note that the final half of the sixth deployment included flights based out of Bermuda to survey clean marine conditions. A complete description of the ACTIVATE mission and its data set are described in Sorooshian et al. (2023).

Now, a broad overview of the instruments housed on the HU-25 Falcon and King Air will be introduced. Then, the instruments relevant to the two studies in this dissertation will be discussed in more detail.

1.2.1 HU-25 FALCON INSTRUMENTATION

The low-flying HU-25 Falcon aircraft housed a diverse set of probes and instruments that measured aerosol, cloud, gas, and meteorological properties in-situ throughout the ACTIVATE campaign (Fig. 3). The following discussion is adapted from Sorooshian et al. (2023).

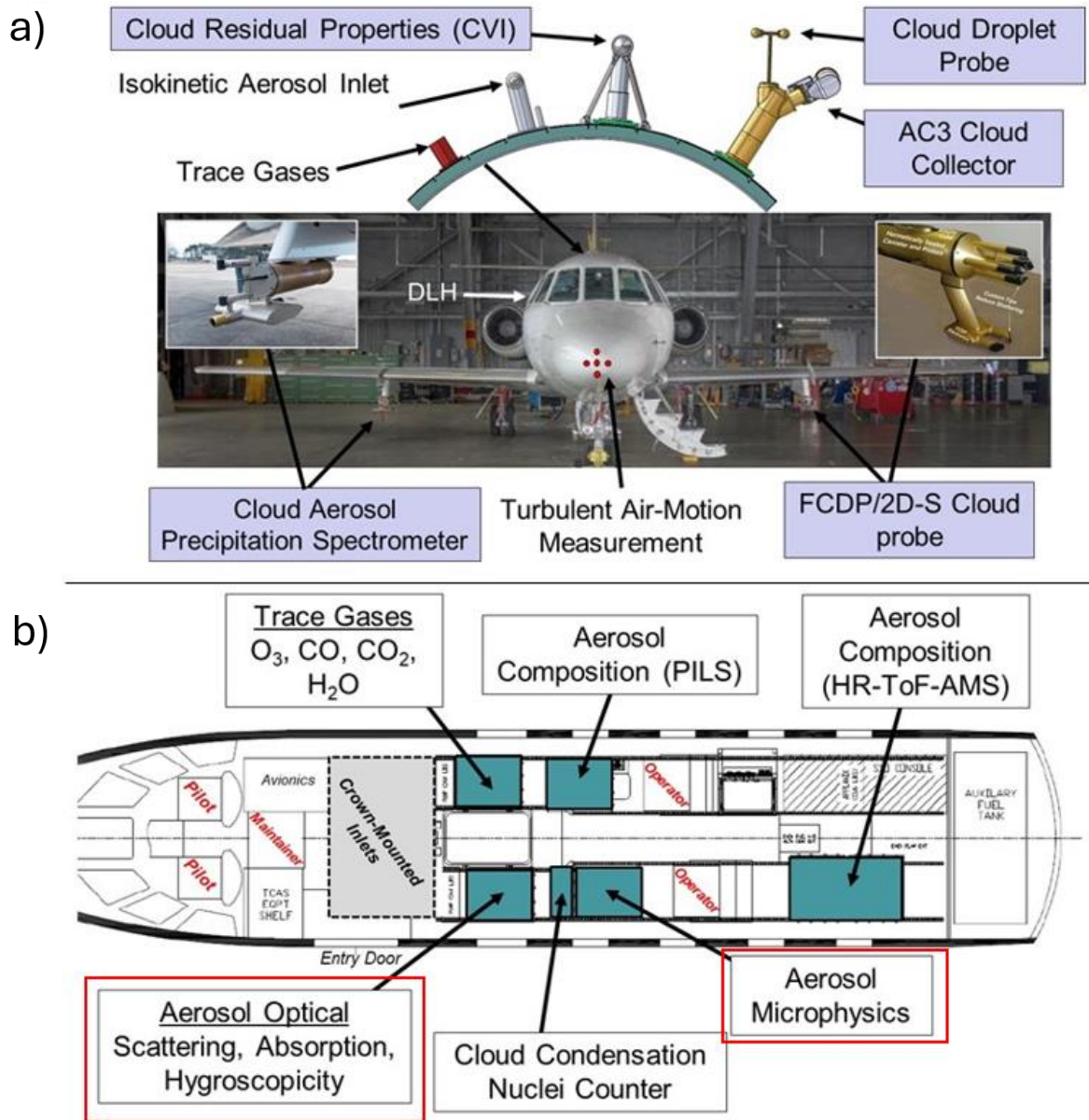


Figure 3: a) Exterior probes and b) interior instrument layout of ACTIVATE's HU-25 Falcon Aircraft (Sorooshian et al., 2023). Red boxes indicate instruments relevant to this dissertation.

Although all the Falcon's instruments provided important measurements for ACTIVATE, the instruments relevant to this dissertation are now described more in detail (red boxes in Fig. 3). First, the instruments related to aerosol microphysics are described. Measurements of aerosol number concentration and size distribution are taken by a TSI Laser Aerosol Spectrometer (LAS) and a TSI Scanning Mobility Particle Sizer (SMPS) (Fig. 4).

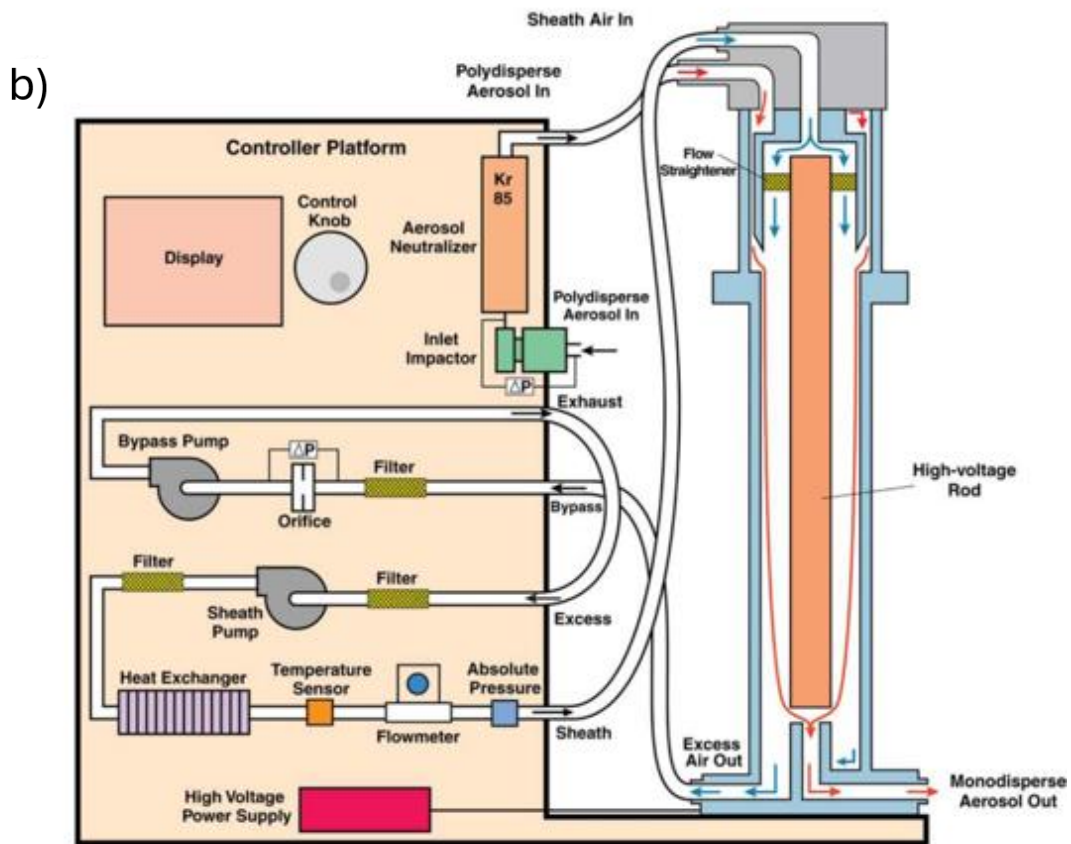
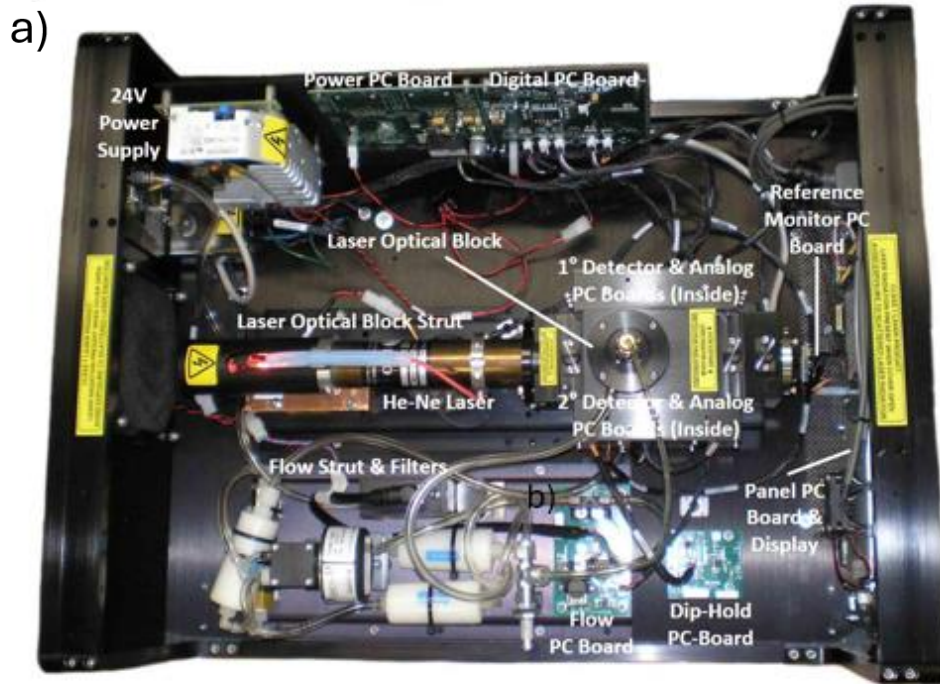


Figure 4: a) Internal layout of TSI 3340 Laser Aerosol Spectrometer (LAS) (TSI, Inc., 2015) and b) schematic of TSI Scanning Mobility Particle Sizer (SMPS) internal layout (TSI, Inc., 2009).

The LAS measures concentrations of aerosol particles with diameters (D) from 94 to 7500 nm based on their optical diameters at a 1 Hz temporal resolution while the SMPS measures particles with D of 2.97 to 94 nm by their electrical mobility diameters at 45 s temporal resolution. Note that these particles are dried with a 6” Perma Pure Monotube Dryer 700 or heated using ram heating during ACTIVATE flights when sampled through the aircraft inlet, so particle D changes as a result. Therefore, the range of D listed refers to dry diameter after sampling. Chapter 2.2 and Appendix B provide an explanation of why drying aerosol particles can introduce limitations in the resulting measurements.

The next set of instruments described are dedicated to measuring aerosol optics. In ACTIVATE, there are two primary instruments that measure aerosol scattering and absorption: the TSI-3563 Nephelometer and the Radiance Research Particle Soot Absorption Photometer (PSAP) (Fig. 5).

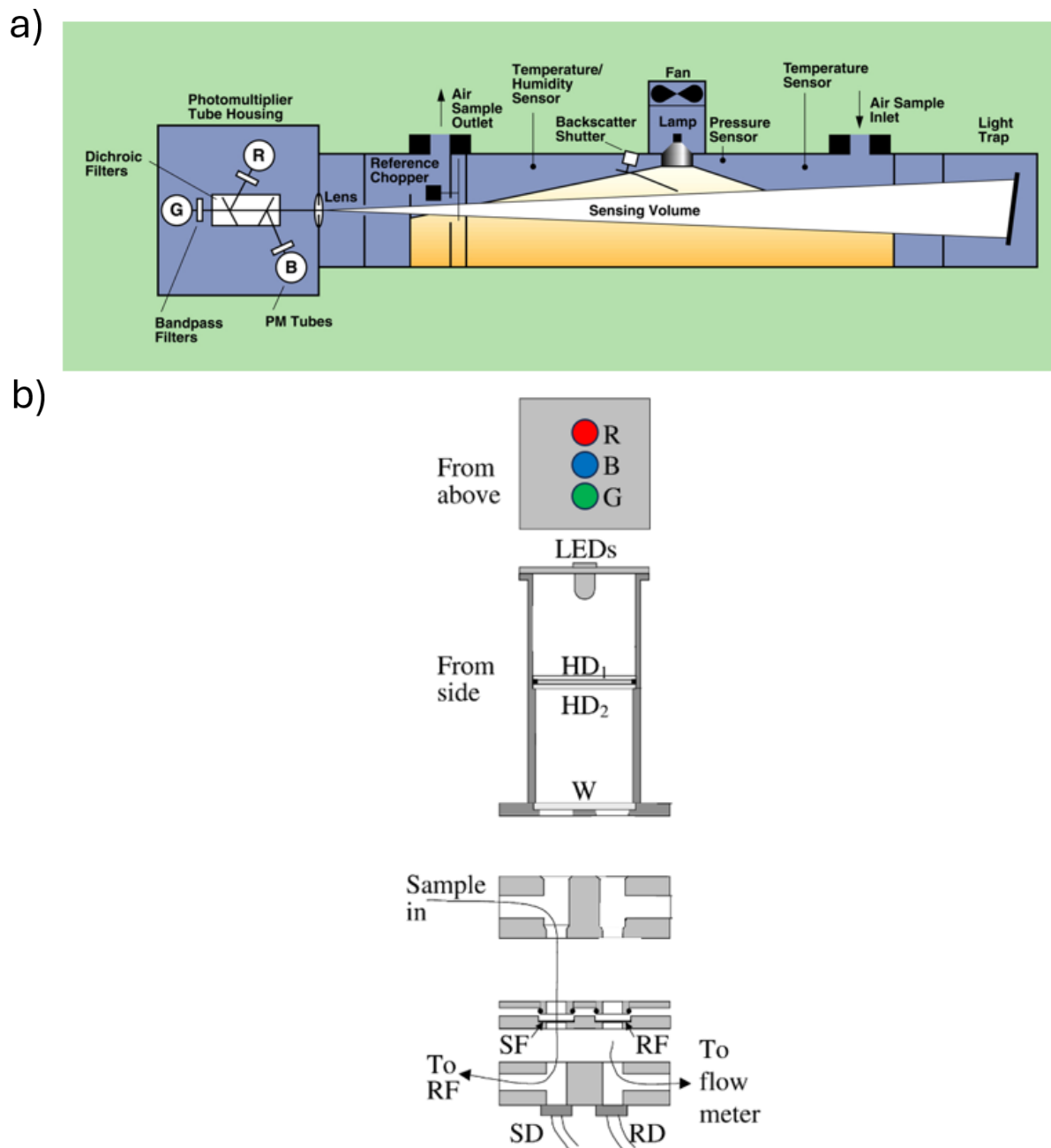


Figure 5: a) Schematic of the TSI-3563 Nephelometer system (adapted from Uin (2016)) and b) Schematic of Radiance Research PSAP optical layout. HD is holographic diffuser, W is window, SF is sample filter, RF is reference filter, SD is signal detector, and RD is reference detector (adapted from Virkkula et al. (2005)).

The TSI-3563 Nephelometer measures scattering coefficients at 450, 550, and 700 nm while the Radiance Research PSAP measures absorption coefficients at 470, 532 and 660 nm. Scattering measurements were made using two nephelometers in parallel, one dry (~20% RH) and one wet (~85% RH). This parallel deployment allows for scattering coefficients to be adjusted to any RH up to saturation (99% RH). The measurements from the nephelometer and PSAP are also used to

calculate other optical parameters such as aerosol extinction (scattering plus absorption) and single scattering albedo (ratio of scattering to extinction). However, error can be introduced into these calculations because the nephelometer and PSAP operate at slightly different wavelengths from one another. Also, these two instruments operate under the assumption of spherical Mie theory, so calculations for cubic or other irregularly-shaped particles may be inaccurate (i.e., dry sea salt, dust).

Also, it is crucial to note that the aircraft sampling inlet has a cutoff D of 5 μm . Therefore, all of the microphysical and optical measurements described are limited to particles $< 5 \mu\text{m}$ in diameter. As a result, these in-situ instruments cannot measure a significant portion of an important class of aerosol particles known as supermicrometer aerosols, which can include large dust, sea salt, and bioaerosol particles (Schlosser et al., 2020; Huang et al., 2024). The second study of this dissertation (Chapter 2.2, Appendix B) proposes an alternative method to calculate aerosol microphysical and optical properties to account for the important issues of aerosol drying, aerosol shape irregularity, and exclusion of particles above 5 μm in diameter.

1.2.2 KING AIR INSTRUMENTATION

The King Air was the high-flying aircraft that contained ACTIVATE's remote sensors and was responsible for launching dropsonde weather devices (Fig. 6).

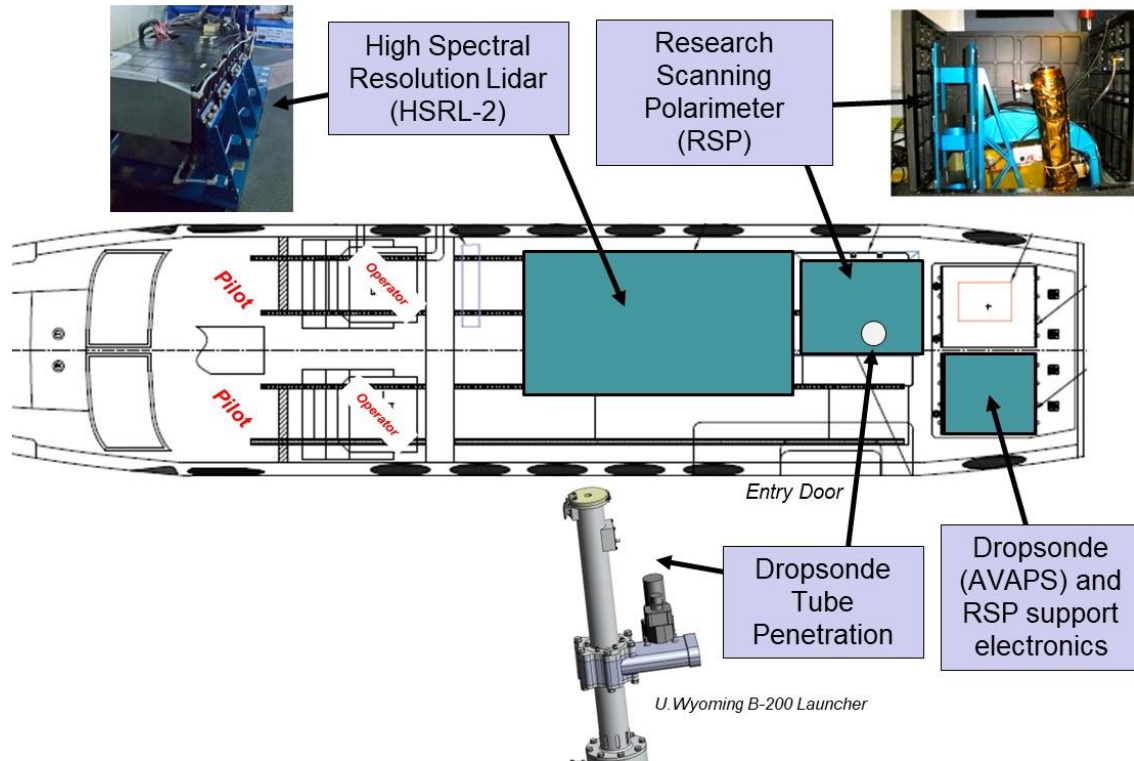


Figure 6: Interior instrument layout of King Air aircraft, which housed ACTIVATE's remote sensors and dropsondes (Sorooshian et al., 2023).

Each instrument is now described in detail. The High Spectral Resolution Lidar – generation 2 (HSRL-2) is an airborne nadir-viewing lidar instrument that has been used in campaigns such as ACTIVATE, the Cloud, Aerosol and Monsoon Processes Philippines Experiment (CAMP²Ex), and the Deriving Information on Surface Conditions from Column and VERTically Resolved Observations Relevant to Air Quality (DISCOVER-AQ) campaign (Fig. 7) (Hair et al., 2008; Sawamura et al., 2017; Burton et al., 2016; Reid et al., 2023; Sorooshian et al., 2023).

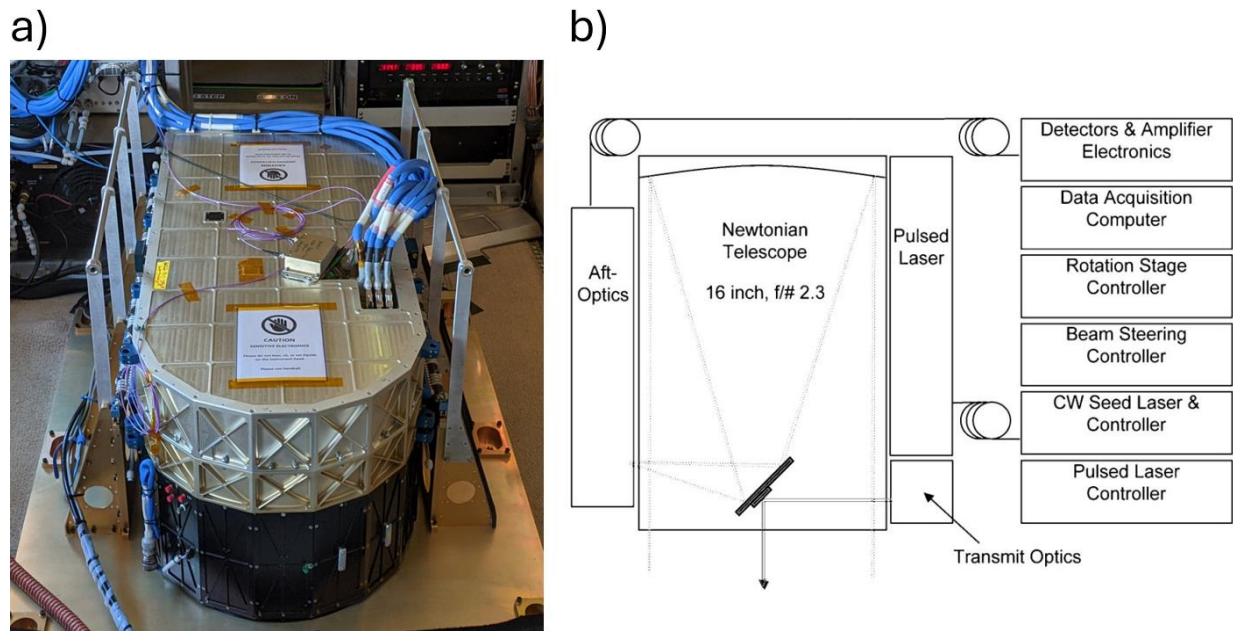


Figure 7: a) Outer view (Aknan, 2024) and b) basic inner layout of HSRL-2 instrument (Hair et al., 2008).

This instrument uses an Nd:YAG laser to make vertically resolved retrievals of aerosol properties such as aerosol backscatter and depolarization at three wavelengths (355, 532, and 1064 nm), aerosol extinction at two wavelengths (355 and 532 nm) (Hair et al., 2008; Burton et al., 2018), and aerosol classification (Burton et al., 2012) (Fig. 7). In addition to these aerosol products, other retrieval capabilities include retrievals of atmospheric mixed layer height (Scarino et al., 2014), ocean subsurface particulate backscatter and attenuation coefficients (Schulien et al., 2017), cloud optical properties (in development), and 10 m surface wind speeds. Details of the laser receiver optics and detectors are described in detail in Hair et al. (2008).

What makes the HSRL-2 unique is that it can measure aerosol backscatter and extinction separately, which proves difficult for standard elastic backscatter lidar such as the one onboard the NASA Cloud-Aerosol Lidar and Infrared Pathfinder Satellite Observation (CALIPSO) satellite (Hair et al., 2008). More details of why this capability is important are explained in the ocean wind speed retrieval study detailed in Chapter 2.1 and Appendix A. The second study, located in Chapter 2.2 and Appendix B, features a comparison between in-situ and HSRL-2 aerosol extinction at 532 nm.

In contrast, the Research Scanning Polarimeter (RSP) is a passive polarimetric remote sensor that uses four polarimetric azimuths and nine spectral channels (410 – 2250 nm) to make highly

accurate multispectral and hyperangular photopolarimetric retrievals of aerosol and cloud properties (Cairns et al., 1999; Cairns et al., 2003) (Fig. 8).

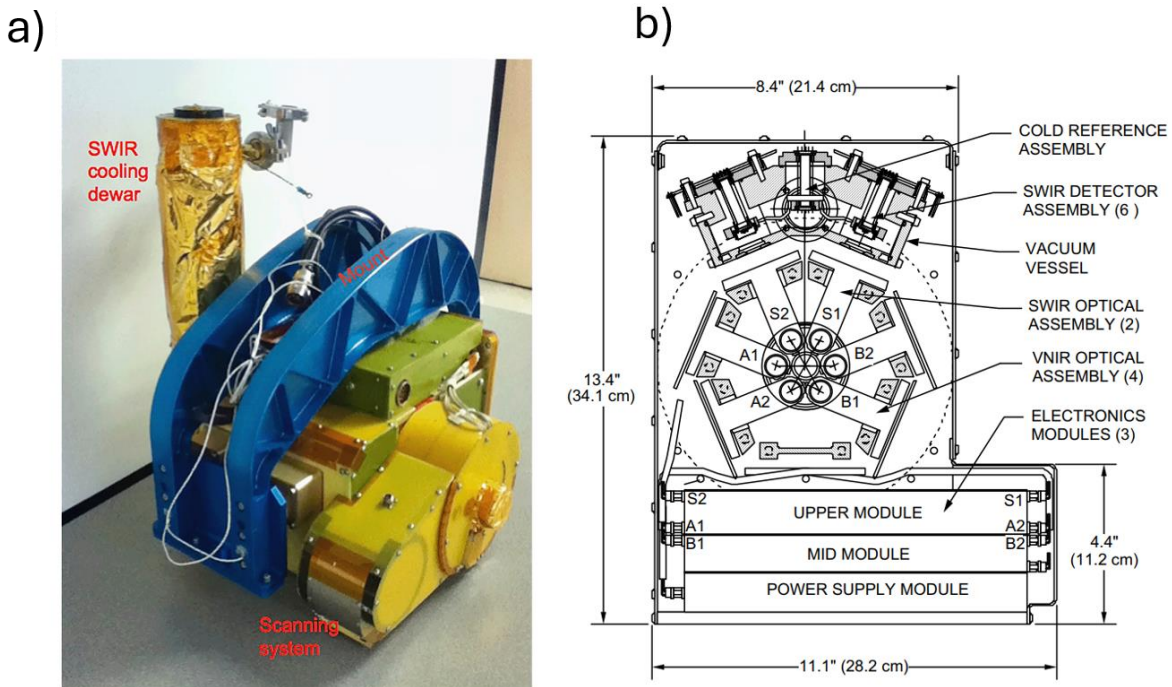


Figure 8: a) Outer view (Schmunk, 2023) and b) basic inner layout of RSP instrument (Cairns et al., 2003).

The aerosol products, relevant to the study detailed in Chapter 2.2 and Appendix B, are based on an optimal estimate algorithm called Research Scanning Polarimeter Microphysical Aerosol Properties (RSP-MAPP) (Stamnes et al., 2018). Fine- and coarse-mode aerosol optical and microphysical properties are retrieved using seven of the RSP's spectral channels with over 100 viewing angles between $\pm 55^\circ$. As a result, the RSP provides column-averaged retrievals of various aerosol optical properties such as single scattering albedo (SSA) and microphysical ones such as aerosol effective radius (r_{eff}).

Lastly, the King Air launches weather devices known as dropsondes that vertically sample various atmospheric parameters as it descends to the ocean surface (Fig. 9). ACTIVATE specifically launched NRD41 mini sondes using the National Center for Atmospheric Research (NCAR) Airborne Vertical Atmospheric Profiling System (AVAPS) (Vömel et al., 2023).



Figure 9: Picture of NCAR AVAPS NRD41 dropsonde when launched from aircraft (Vömel and Dunion, 2023).

A variable number of dropsondes were launched per flight, usually 3 to 4 for routine flights, with more being launched for specific targeted flight opportunities. With response times much less than 1 second, AVAPS samples position, wind speed (Vömel and Dunion, 2023), and state variables such as pressure, temperature, and humidity all the way to ~6 m above the ocean surface. The data are then post-processed via NCAR's Atmospheric Sounding Processing Environment (ASPEN) software where any spurious data are removed including any data returned from the ocean surface itself (Martin and Suhr, 2021). More details on the AVAPS system and its usage on other aircraft and missions can be found in Vömel et al. (2021) and Vömel and Dunion (2023) and details of its usage in ACTIVATE specifically can be found in Vömel et al. (2023).

1.3 EXPLANATION OF DISSERTATION FORMAT

The first study discussed in this dissertation is “High Spectral Resolution Lidar – generation 2 (HSRL-2) Retrievals of Ocean Surface Wind Speed: Methodology and Evaluation”, which has been accepted for publication to Atmospheric Measurement Techniques (AMT) on 15 April 2024. This paper introduces a new airborne ocean surface wind speed product from NASA Langley Research Center’s (LaRC’s) High Spectral Resolution Lidar – generation 2 (HSRL-2). This work details the algorithm of how the lidar retrieves surface wind speeds followed by how this product is evaluated using ACTIVATE data.

The second study presented is “Closing the gap between in-situ and remotely sensed aerosol particle properties”, which will be submitted to AMT. This work focuses on enabling comparison of ambient measurements of aerosol optical and microphysical properties between ACTIVATE’s in-situ and remote sensing instruments using the In Situ Aerosol Retrieval Algorithm (ISARA). First, the ISARA methodology is described in detail and then the process of performing external closure of ambient aerosol properties between ACTIVATE’s in-situ instruments and remote sensors is introduced and evaluated.

Summaries of these two studies are found in Chapters 2.1 and 2.2, respectively. The manuscripts themselves are in Appendix A and B, respectively. Appendix C lists all of the author’s publications while enrolled as a Ph.D. student in the Sorooshian Group at the University of Arizona.

CHAPTER 2: STUDY DESCRIPTIONS

2.1 HSRL-2 RETRIEVALS OF OCEAN SURFACE WIND SPEED

As mentioned in Chapter 1, ocean surface winds are the main driver of MABL processes such as heat fluxes, gas exchange, aerosol transport, and cloud formation. To quantify the influence of these surface winds on these atmospheric phenomena, it is typical to measure their speeds using various surface (buoy and ship anemometers) and remote sensing (radiometers, scatterometers, lidar) instrument suites (Bourassa et al., 2019). However, this study discusses how to specifically use lidar to obtain accurate surface wind speed measurements.

Historically, satellite lidar systems such as the one onboard the NASA Cloud-Aerosol Lidar and Infrared Pathfinder Satellite Observation (CALIPSO) satellite have been used to provide horizontally-resolved surface wind speed data although these systems are typically dedicated to measuring aerosol and cloud parameters (Hu et al., 2008; Venkata and Reagan, 2016). The underlying principle of lidar surface wind speed retrievals was first derived by Cox and Munk (1954), where bidirectional reflectance measurements of sea-surface glint are used to establish a Gaussian relationship between surface wind speeds and the distribution of wind-driven wave slopes. where U is wind speed and σ^2 is the wave-slope variance. To probe these surface wave slopes, lidar instruments emit laser pulses into the atmosphere and measure the reflectance (or backscatter) of those laser pulses from particles, molecules, and the ocean surface. The magnitude of the measured signal is then used to estimate the variance of the wave-slope distribution (i.e., wave-slope variance) and therefore surface wind speed. This phenomenon described by the following linear relationship (Cox and Munk, 1954):

$$U = \left(\frac{\langle \sigma^2 \rangle - .003}{.00512} \right). \quad (1)$$

More parameterizations such as Wu (1990) and Hu et al. (2008) have been developed since the original model proposed by Cox and Munk (1954) to account for atmospheric attenuation, but they cannot directly account for atmospheric attenuation by aerosols and therefore have difficulty in calibrating the measured ocean surface reflectance accurately. Therefore, assumptions must be made on the contribution of this attenuation to the lidar signal.

This study addresses retrieving surface wind speed directly from a lidar without other assumptions or external constraints by employing the high-spectral-resolution lidar (HSRL) technique through NASA Langley Research Center's (LaRC's) airborne High Spectral Resolution Lidar – generation 2 (HSRL-2) instrument (Hair et al., 2008). The HSRL-2 can directly measure vertically resolved aerosol backscatter and extinction profiles without relying on an assumed lidar ratio or other external aerosol constraints, enabling accurate estimates of the attenuation of the atmosphere. Therefore, the surface reflectance can be directly determined, providing a measure of the wave-slope variance and thus surface wind speed. This algorithm is evaluated using dropsonde data from the NASA ACTIVATE mission detailed in Chapter 1.2.

The main findings from this study are:

1. The overall HSRL-2 retrieval accuracy is calculated to be $0.15 \text{ m s}^{-1} \pm 1.80 \text{ m s}^{-1}$.
2. Dropsonde surface wind speed measurements most closely match with the Hu et al. (2008) wind speed – wave-slope variance model than the Cox and Munk (1954) and Wu (1990) models for surface wind speeds below 7 m s^{-1} .
3. HSRL-2 retrievals are more accurate in the summer than in winter. However, the HSRL-2 still provides substantial and accurate surface wind speed data in winter despite this season's substantial cloud cover and aerosol loadings.
4. The high horizontal spatial resolution of the HSRL-2 of 0.5 s or $\sim 75 \text{ m}$ along track allows the instrument to probe the fine-scale variability of surface wind speeds over time, which allows for observation of MABL phenomena such as SST dynamics and cloud evolution.
5. The HSRL-2 can detect the surface in broken cloud scenes, showing that the retrievals are not limited to aerosol-free conditions.

2.2 EXTERNAL CLOSURE OF IN-SITU AND REMOTE SENSING AMBIENT AEROSOL DATA

As discussed in Chapter 1, atmospheric aerosol particles critically influence the state of the MABL directly (i.e., scattering and absorption of solar radiation) and indirectly (i.e., cloud formation). Therefore, it is important for field campaigns to measure the various microphysical and optical properties of these aerosol particles to better understand how they influence the atmosphere. To ensure quality of these aerosol data sets, flight scientists typically perform verification (i.e., “closure”) analysis by comparing data sets between different instrument platforms within a field campaign. However, closure analysis has become increasingly difficult to perform partly due to i) aerosol chemistry research transitioning deeper into complex organic species that are more difficult to measure than inorganic species and ii) organizations deploying more diverse sets of field campaign instruments that use differing calibration standards (Wilson and Jonsson, 2011). However, what makes closure most difficult is that in-situ instruments typically use heaters or dryers to control the relative humidity (RH) of the air sample containing aerosol particles, in contrast to remote sensors that retrieve data from aerosol particles in ambient air conditions and therefore do not alter the RH of the sampled particles. Therefore, the in-situ data represent aerosol particles with significantly different shapes, sizes, and compositions (and consequently optical behavior) than what are represented by the remote sensing data.

To address these challenges and ultimately promote more rigorous field campaign data quality assurance, this second study focuses on performing external closure between ACTIVATE’s in-situ and remote sensing platforms using an open-source codebase called the In Situ Aerosol Retrieval Algorithm (ISARA) developed in coordination with the Office of Naval Research. This algorithm uses ACTIVATE’s in-situ data to model ambient aerosol optical properties at any RH until saturation (99%) at any user-specified wavelength. What is unique about this algorithm is that it considers the contribution of particles of $D > 5 \mu\text{m}$ (i.e., coarse-mode aerosol) when calculating ambient aerosol properties, which is generally a limitation in similar algorithms (i.e., Sawamura et al., 2017).

The main findings of this study are:

1. Assumptions on the contribution of coarse-mode aerosol to ambient aerosol properties generally lead to at least partial successful closure between in-situ and remote sensing measurements.
2. Systematic closure is possible between in-situ measurements and RSP retrievals, which has not been shown in the literature to date. Despite lower performance with these retrievals in terms of goodness of fit compared to the HSRL-2 results, ISARA-calculated measurements show identical or near-identical mean errors to RSP retrievals.

**APPENDIX A: HIGH SPECTRAL RESOLUTION LIDAR – GENERATION
2 (HSRL-2) RETRIEVALS OF OCEAN SURFACE WIND SPEED:
METHODOLOGY AND EVALUATION**

The following article has been accepted by the journal Atmospheric Measurement Techniques (AMT) on 15 April 2024.

High Spectral Resolution Lidar – generation 2 (HSRL-2) Retrievals of Ocean Surface Wind Speed: Methodology and Evaluation

Sanja Dmitrovic¹, Johnathan W. Hair², Brian L. Collister², Ewan Crosbie^{2,3}, Marta A. Fenn², Richard A. Ferrare², David B. Harper², Chris A. Hostetler², Yongxiang Hu², John A. Reagan⁴, Claire E. Robinson^{2,3,+}, Shane T. Seaman², Taylor J. Shingler², Kenneth L. Thornhill^{2,3}, Holger Vömel⁵, Xubin Zeng⁶, Armin Sorooshian^{1,6,7}

¹James C. Wyant College of Optical Sciences, University of Arizona, Tucson, AZ 85721, USA

²NASA Langley Research Center, Hampton, VA 23681, USA

³Analytical Mechanics Associates, Hampton, VA 23666, USA

⁴Department of Electrical and Computer Engineering, University of Arizona, Tucson, AZ 85721, USA

⁵National Center for Atmospheric Research, Boulder, CO 80307, USA

⁶Department of Hydrology and Atmospheric Sciences, University of Arizona, Tucson, AZ 85721, USA

⁷Department of Chemical and Environmental Engineering, University of Arizona, Tucson, AZ 85721, USA

⁺Deceased

Correspondence to: Armin Sorooshian (armin@arizona.edu)

Abstract. Ocean surface wind speed (i.e., wind speed 10 m above sea level) is a critical parameter used by atmospheric models to estimate the state of the marine atmospheric boundary layer (MABL). Accurate surface wind speed measurements in diverse locations are required to improve characterization of MABL dynamics and assess how models simulate large-scale phenomena related to climate change and global weather patterns. To provide these measurements, this study introduces and evaluates a new surface wind speed data product from NASA Langley Research Center’s nadir-viewing High Spectral Resolution Lidar – generation 2 (HSRL-2) using data collected as part of NASA’s Aerosol Cloud meTeorology Interactions oVer the western ATlantic Experiment (ACTIVATE) mission. The HSRL-2 can directly measure vertically resolved aerosol backscatter and extinction profiles without additional constraints or assumptions, enabling the instrument to accurately derive atmospheric attenuation and directly determine surface reflectance (i.e., surface backscatter). Also, the high horizontal spatial resolution of the HSRL-2 retrievals (0.5 s or ~75 m along track) allows the instrument to probe the fine-scale spatial variability of surface wind speeds over time along the flight track and breaks in broken cloud fields. A rigorous evaluation on these retrievals is performed by comparing coincident HSRL-2 and National Center for Atmospheric Research (NCAR) AVAPS dropsonde data, owing to the joint deployment of these two instruments on ACTIVATE’s King Air aircraft. These comparisons show correlations of 0.89, slopes of 1.04 and 1.17, and y-intercepts of -0.13 m s^{-1} and -1.05 m s^{-1} for linear and bisector regressions, respectively and the overall accuracy is calculated to be $0.15 \text{ m s}^{-1} \pm 1.80 \text{ m s}^{-1}$. It is also shown that the dropsonde surface wind speed data most closely follows the HSRL-2 distribution of wave-slope variance using the distribution proposed by Hu et al. (2008) than the ones proposed by Cox and Munk (1954) and Wu (1990) for surface wind speeds below 7 m s^{-1} , with this category comprising most of the ACTIVATE data set. The retrievals are then evaluated separately for surface wind speeds below 7 m s^{-1} and between 7 m s^{-1} and 13.3 m s^{-1} and show that the HSRL-2 retrieves surface wind speeds with a bias of $\sim 0.5 \text{ m s}^{-1}$ and an error of $\sim 1.5 \text{ m s}^{-1}$, a finding not apparent in the cumulative comparisons. Also, it is shown that the HSRL-2 retrievals are more accurate in the summer

($-0.18 \text{ m s}^{-1} \pm 1.52 \text{ m s}^{-1}$) than winter ($0.63 \text{ m s}^{-1} \pm 2.07 \text{ m s}^{-1}$), but the HSRL-2 is still able to make numerous, ($N = 236$) accurate retrievals in the winter. Overall, this study highlights the abilities and assesses the performance of the HSRL-2 surface wind speed retrievals and it is hoped that further evaluation of these retrievals will be performed using other airborne and satellite data sets.

1 Introduction

The layer between the ocean and free troposphere, known as the marine atmospheric boundary layer (MABL), hosts various processes such as the modulation of sensible and latent heat fluxes, the exchange of gases such as carbon dioxide, the evolution of clouds, and the transport of aerosol particles (Neukermans et al., 2018). Improved characterization of MABL dynamics is required to accurately simulate large-scale phenomena related to climate change and global weather patterns (Paiva et al., 2021). This characterization relies on a combination of global numerical weather prediction (NWP) models and real observations (Carvalho, 2019). One of the most influential parameters that drive these MABL processes is ocean surface wind speeds or wind speeds at 10 m above sea level (hereafter called surface wind speeds). Therefore, instruments such as lidar are used to provide accurate surface wind speed measurements in various geographical locations to improve estimations of the MABL state globally. For instance, satellite lidar systems that measure aerosol and cloud vertical distributions, such as the lidar on board the NASA Cloud-Aerosol Lidar and Infrared Pathfinder Observation (CALIPSO) satellite, also have the capability to provide horizontally-resolved surface wind speed data. The underlying principle of lidar surface wind speed retrievals was first derived by Cox and Munk (1954), where bidirectional reflectance measurements of sea-surface glint are used to establish a Gaussian relationship between surface wind speeds and the distribution of wind-driven wave slopes. To probe these surface wave slopes, lidar instruments emit laser pulses into the atmosphere and measure the reflectance (or backscatter) of those laser pulses from particles, molecules, and the ocean surface. The magnitude of the measured signal is then used to estimate the variance of the wave-slope distribution (i.e., wave-slope variance) and therefore surface wind speed. Note that reflectance and backscatter are used interchangeably throughout this paper.

Although many studies have expanded upon the original Cox-Munk relationship (e.g., Hu et al., 2008; Josset et al., 2008; Josset et al., 2010a; Kiliyanpilakkil and Meskhidze, 2011; Nair and Rajeev, 2014; Murphy and Hu, 2021; Sun et al., 2023), these parameterizations do not account for atmospheric attenuation by aerosols and therefore have difficulty in calibrating the measured ocean surface reflectance accurately. This presents a difficulty for elastic backscatter lidars like CALIPSO, for which the signal is typically calibrated high in the atmosphere where molecular backscatter dominates and aerosol backscatter is insignificant or can be accurately estimated. The problem lies in the transfer of this calibration to the ocean surface, which entails accounting for the attenuation of the transmitted and backscattered light by the intervening atmosphere between the calibration region and the ocean surface. If coincident aerosol optical depth (AOD) data are available (e.g., from MODIS in the case of CALIPSO detailed in Josset et al. (2008)) then they may be used to estimate the intervening attenuation and transfer the calibration. However, such data from passive sensors including MODIS are only available during daytime, are typically not produced in the vicinity of clouds and may have unacceptably high uncertainties for accurately accounting for aerosol attenuation. Estimation of the attenuation from the lidar data alone requires an assumption of the aerosol extinction-to-backscatter ratio (or

“lidar ratio”), so errors in the assumed value can lead to an incorrect estimate of attenuation, especially when AOD is high. Because of this, the surface wind speed estimates in Hu et al. (2008) were limited to scenes with no clouds and negligible aerosol loading.

This study addresses retrieving surface wind speed directly from a lidar without other assumptions or external constraints by employing the high-spectral-resolution lidar (HSRL) technique through NASA Langley Research Center’s (LaRC’s) airborne High Spectral Resolution Lidar – generation 2 (HSRL-2) instrument (Hair et al., 2008). The HSRL-2 can directly measure vertically resolved aerosol backscatter and extinction profiles without relying on an assumed lidar ratio or other external aerosol constraints, enabling accurate estimates of the attenuation of the atmosphere. Therefore, the surface reflectance can be directly determined, providing a measure of the wave-slope variance and thus surface wind speed. Note that the HSRL-2 operates at a nadir-viewing geometry, which is detailed more in Sect. 2.4. At nadir or near-nadir incidence angles, the surface contribution of the lidar surface backscatter signal is the largest and is therefore sensitive to changes in wind speed (Josset et al., 2008; Josset et al., 2010a; Josset et al., 2010b), making it possible to introduce relatively simplified models of sea surface reflectance. However, Li et al. (2010) demonstrated that at the higher incidence angle lidar systems ($> 15^\circ$), the sensitivity of the lidar surface signal would rapidly decrease as these highly non-nadir incidences shift the signal towards a subsurface contribution rather than a surface one. A more recent lidar study based on the highly non-nadir ($\sim 37^\circ$) Aeolus UV HSRL lidar (Labzovskii et al., 2023) indirectly confirms this phenomenon by showing low agreement between passive remote sensing reflectivity and Aeolus surface reflectivity parameters over water surfaces such as oceans. For these reasons, an opportunity to retrieve ocean surface wind speeds using lidar ocean backscattering has been shown to be effective only for nadir or near-nadir lidar systems such as the HSRL-2.

This study details the HSRL-2’s surface wind speed retrieval methodology and evaluates this surface wind speed product through comparison with measurements from National Center for Atmospheric Research (NCAR) Airborne Vertical Atmospheric Profiling System (AVAPS) dropsondes. This work leverages an extensive data set from NASA’s Aerosol Cloud meteorology Interactions over the western ATLantic Experiment (ACTIVATE) mission, which had multiple scientific and technological objectives described in Sect. 2.1 (Sorooshian et al., 2019). The mission consisted of six deployments between 2020 and 2022 and featured the joint deployment of the HSRL-2 and dropsonde launcher on one of its two aircraft to enable direct comparison between the two instrument data sets. The mission, dropsonde and HSRL-2 instrumentation, HSRL-2 algorithm, and the methods and results of using/evaluating the HSRL-2 and dropsonde surface wind speed data sets are all detailed in the following discussion.

2 Methods

2.1 ACTIVATE Mission Description

The HSRL-2 ocean surface wind speed product is assessed during the ACTIVATE campaign, which is a NASA Earth Venture Suborbital-3 (EVS-3) mission. The primary aim of ACTIVATE is to improve knowledge of aerosol-cloud-meteorology interactions, which are linked to the highest uncertainty among components contributing to total anthropogenic radiative forcing (Bellouin et al., 2020). There are three major scientific objectives: (i) characterize

interrelationships between aerosol particle number concentration (N_a), CCN concentration, and cloud drop number concentration (N_d) with the goal of decreasing uncertainty in model parameterizations of droplet activation; (ii) advance process-level knowledge and simulation of cloud microphysical and macrophysical properties, including the coupling of aerosol effects on clouds and cloud effects on aerosol particles; and (iii) assess remote sensing capabilities to retrieve geophysical variables related to aerosol-cloud interactions. This study focuses on the third objective, which has already received attention with ACTIVATE data for retrievals other than ocean surface wind speeds (Schlosser et al., 2022; Van Diedenhoven et al., 2022; Chemyakin et al., 2023; Ferrare et al., 2023). ACTIVATE built a high volume of flight data statistics over the Western North Atlantic Ocean (WNAO) by flying six deployments across three years (2020 – 2022), with a winter and summer deployment each year (Sorooshian et al., 2023). Winter deployments included the following date ranges: 14 February – 12 March (2020), 27 January – 2 April (2021), 30 November 2021 – 29 March (2022). Summer deployments were as follows: 13 August – 30 September (2020), 13 May – 30 June (2021), 3 May – 18 June (2022). Across all three years, 90 King Air flights during the winter deployment were performed with 373 dropsondes launched while 78 flights during the summer deployment took place with 412 dropsondes launched.

Two NASA Langley aircraft flew in spatial and temporal coordination for the majority of the total flights (162 of 179). A “stacked” flight strategy was developed where a low-flying (< 5 km) HU-25 aircraft collected in situ data in and just above the MABL while a high-flying (~9 km) King Air aircraft simultaneously provided remote sensing retrievals and dropsonde measurements in the same altitude range. In doing so, the stacked aircraft would simultaneously obtain data relevant to aerosol-cloud-meteorology interactions in the same column of the atmosphere and provide a complete picture of the lower troposphere (Sorooshian et al., 2019). In situ measurements of gases, particles, meteorological variables, and cloud properties were conducted by the HU-25 Falcon. The King Air’s payload included the NASA Goddard Institute for Space Studies (GISS) Research Scanning Polarimeter (RSP) and the two instruments relevant to this work: the NASA LaRC HSRL-2 and the NCAR AVAPS dropsondes (Sorooshian et al., 2023). An advantage of the joint deployment of HSRL-2 and AVAPS dropsondes on the King Air is that the data are spatially synchronized at launch, with wind drift of the dropsondes during descent accounted for with procedures summarized in Sect. 2.2.

The rationale to fly over the WNAO in different seasons was to collect data across a wide range of aerosol and meteorological regimes, with the latter promoting a broad range of cloud conditions (Painemal et al., 2021). A significant meteorological feature is the North Atlantic Oscillation, which is the oscillation between the Bermuda-Azores High (high pressure system) and the Icelandic Low (low pressure system) (Lamb and Pepler, 1987). In the summer, the Bermuda-Azores High is at its peak and introduces easterly and southwesterly trade winds (Sorooshian et al., 2020). Starting in the fall, the Icelandic Low becomes prominent and introduces westerly winds in the boundary layer. The balancing act between these pressure systems dictates the climate of the North Atlantic and the prevailing transport processes (Li et al., 2002; Creilson et al., 2003; Christoudias et al., 2012). These transport processes that vary seasonally explain why winter flights coincided with more offshore (westerly) flow containing aerosol types impacted by anthropogenic influence (e.g., Corral et al., 2022), whereas summer flights included more influence from wildfire emissions and African dust among other sources both natural and anthropogenic in nature (Mardi et al., 2021; Aldhaif et al., 2020). Winds and turbulence tend to be stronger in the winter due to higher temperature gradients

between the air and the ocean (Brunke et al., 2022), resulting in a higher fraction of available aerosol particles in the MABL that activate into cloud droplets in winter coinciding with cold air outbreaks as compared to summer (Dadashazar et al., 2021b; Kirschler et al., 2022; Painemal et al., 2023). Therefore, this study region allows the HSRL-2 surface wind speed retrievals to be evaluated in various meteorological and aerosol loading conditions.

2.2 Dropsondes

The AVAPS system deployed during the ACTIVATE mission utilized the newer, more reliable NRD41 mini sondes. Their smaller form factor along with updates to their launching hardware increased reliability for launches since these instruments could be used with more aircraft and launcher configurations (Vömel and Dunion, 2023). A variable number of dropsondes were launched per flight, usually 3 to 4 for routine flights, with more being launched for specific targeted flight opportunities. With response times much less than 1 second, AVAPS samples position, wind speed (with 0.5 m s^{-1} uncertainty) (Vömel and Dunion, 2023), and state variables such as pressure, temperature, and humidity all the way to ~ 6 m above the ocean surface. The data are then post-processed via NCAR's Atmospheric Sounding Processing Environment (ASPEN) software where any spurious data are removed including any data returned from the ocean surface itself (Martin and Suhr, 2021). More details on the AVAPS system and its usage on other aircraft and missions can be found in (Vömel et al., 2021) and details of its usage in ACTIVATE specifically can be found in Vömel and Dunion (2023). Not many studies exist on surface wind speed validation of aircraft instruments with dropsondes (Bedka et al., 2021), so this study also highlights the potential of using dropsondes to validate aircraft surface wind speed data.

2.3 HSRL-2 Instrument Description

The NASA LaRC HSRL-2 is an airborne lidar instrument designed to enable vertically resolved retrievals of aerosol properties such as aerosol backscatter and depolarization at three wavelengths (355, 532, and 1064 nm), aerosol extinction at two wavelengths (355 and 532 nm) (Hair et al., 2008; Burton et al., 2018), and aerosol classification (Burton et al., 2012). In addition to these aerosol products, other retrieval capabilities include retrievals of atmospheric mixed layer height (Scarino et al., 2014), ocean subsurface particulate backscatter and attenuation coefficients (Schulien et al., 2017), cloud optical properties (in development), and 10 m surface wind speeds, the latter of which is the focus of this study. Details of the laser receiver optics and detectors are described in detail in Hair et al. (2008). This analysis utilizes the 532 nm data channels that include a total scattering channel (both molecular and particulate scattering), molecular scattering only, and the cross polarized channel, which are internally calibrated during flight. Key to determining the optical transmission and subsurface signals is a molecular channel that filters essentially all the particulate and specular scattering using the iodine notch filter as described in Hair et al. (2008), determining both the laser transmission down to the surface and correction of the subsurface scattering contribution to the integrated surface backscatter signal.

The laser is a custom built 200 Hz repetition rate Nd:YAG laser emitting at 1064 nm, which is converted to both the second and third harmonic wavelengths of 532 nm and 355 nm, respectively. The output laser energies are nominally 34 mJ (1064 nm), 11 mJ (532 and 355 nm each) and each is set to a divergence ($1/e^2$) of approximately 0.8 mrad, giving a beam footprint diameter on the ocean surface of ~ 7 m for the nominal 9 km King Air flight altitude. The

telescope is set to a full field of view of 1 mrad, giving a viewing footprint diameter of 9 m at the ocean surface at nominal flight altitude. All three wavelengths are transmitted coaxially with the telescope through a fused silica window in the bottom of the aircraft are actively boresighted to the receiver. The HSRL-2 incorporates high speed photomultiplier tubes (PMTs) and custom amplifiers to allow data collection at 120 MHz sampling rates with 40 MHz bandwidths. Data are sampled at 120 MHz (1.25 m in the atmosphere and 0.94 m in the ocean) with 16-bit digitizers and single-shot profiles are summed over 100 laser shots during 0.5 s which is the fundamental acquisition interval before storing to a disk. The aircraft incorporates an Applanix Inertial Navigation System (INS) to record the aircraft altitude at 0.5 s time intervals corresponding to each 100-shot data profile.

2.4 HSRL-2 Surface Wind Speed Retrieval Method

As mentioned in the previous section, a lidar system emits laser pulses into the atmosphere and the backscattered light from particles (aerosols) and molecules is collected with a telescope and imaged onto optical detectors where the generated analog electrical signal is digitally sampled as a function of time. Backscatter is also received from the reflection of the laser pulse off the ocean surface and is referred to as the “surface return” signal. To derive surface wind speeds, the surface backscattered (180°) reflected radiance (β_{surf} , units sr^{-1}) is estimated from the surface return signal and related to the wave-slope variance (σ^2), as detailed in Josset et al. (2010b), through

$$\beta_{surf} = \frac{C_F}{4\pi\sigma^2 \cos^5(\theta)} e^{-\frac{\tan^2(\theta)}{\sigma^2}}, \quad (1)$$

where C_F is the Fresnel coefficient and is set to 0.0205 as given in Venkata and Reagan (2016) and θ is the angle of incidence of the laser with the ocean surface. As noted in the Introduction, the HSRL-2 is operated in a nadir-only viewing geometry (i.e., not scanning). However, there is a small offset from this nadir incidence angle due to the pitch and roll angles of the King Air aircraft. This offset angle is measured by the Applanix INS and is then used in Eq. 1 to derive the wave-slope variance. The median pitch and roll angles depend on the flight conditions (e.g., wind and fuel loads), but ranged from 2 - 5° for pitch and $< 1^\circ$ for roll during ACTIVATE flights. The surface wind speed data are screened to limit the pitch and roll to less than $\pm 3^\circ$ from the median values, resulting in HSRL-2 incidence angles of $< 3^\circ$ for roll and $< 8^\circ$ for pitch. This screening effectively selects cases where the aircraft is flying straight and level legs.

The mean wind speed at 10 m above the sea surface (U) is then derived using a piecewise empirical relationship between surface wind speed and wave-slope variance from Hu et al. (2008), where:

$$U = \left(\frac{\langle \sigma^2 \rangle}{0.0146} \right)^2, \langle \sigma^2 \rangle < 0.0386, U < 7 \text{ m s}^{-1}, \quad (2.1)$$

$$U = \left(\frac{\langle \sigma^2 \rangle - 3.0E-3}{5.12E-3} \right), 0.0386 \leq \langle \sigma^2 \rangle < 0.0711, 7 \text{ m s}^{-1} \leq U < 13.3 \text{ m s}^{-1}, \quad (2.2)$$

$$U = 10 \left(\frac{\langle \sigma^2 \rangle + 0.084}{0.138} \right), \langle \sigma^2 \rangle \geq 0.0711, U \geq 13.3 \text{ m s}^{-1}. \quad (2.3)$$

The relationships shown in Eqs. 2.1 – 2.3 were derived by Hu et al. (2008) using the comparisons between AMSR-E surface wind speeds and CALIPSO backscatter reflectance mentioned in Sect. 1 and agree identically with the Cox-

Munk relationship for surface wind speeds between 7 m s^{-1} and 13.3 m s^{-1} and the log-linear relationship proposed by Wu (1990) for surface wind speeds above 13.3 m s^{-1} .

With respect to surface wind speed retrievals, the HSRL-2 instrument offers two major advantages over standard backscatter lidars such as CALIPSO: 1) it can account for atmospheric attenuation between the aircraft and the surface so retrievals can be performed without constraining the retrieval to low AOD conditions (i.e., negligible aerosol loading) or assuming the lidar ratio, and 2) it has high vertical resolution sampling (1.25 m) that enables accurate correction for ocean subsurface scattering, which makes a small but non-negligible contribution to the measured surface return. The equations for the HSRL-2 532-nm measurement channels are:

$$P_{mol}(r) = G_{mol} \frac{1}{r^2} F(r) \beta_m^{\parallel}(r) T^2(r), \quad (3.1)$$

$$P_{tot}(r) = G_{mol} G_{i2} \frac{1}{r^2} \left[\left(\beta_p^{\parallel}(r) + \beta_m^{\parallel}(r) \right) + G_{dep} \left(\beta_p^{\perp}(r) + \beta_m^{\perp}(r) \right) \right] T^2(r) \quad (3.2)$$

where P_x is the total measured signal per sampling interval by the lidar and r denotes the range from the lidar. Here the *mol* subscript denotes the measured signal on the molecular channel, for which all particulate backscatter and the surface return is blocked by an iodine vapor filter. The *tot* subscript denotes the “total” backscatter calculated from the sum of two measurement channels, the co-polarized channel and the cross-polarized channel. These channels are essentially elastic backscatter lidar channels similar to the 532 nm channels on CALIPSO, in that they measure attenuated backscatter from both molecules and particles. The co-polarized channel measures backscatter that is polarized parallel to the linear polarization of the transmitted laser pulses, and the cross-polarized channel measures backscatter with polarization perpendicular to the laser pulses. The volume backscatter coefficient, β (units $\text{m}^{-1} \text{sr}^{-1}$), is separated into components arising from either molecular scattering (m) or particulate scattering (p) and by polarization parallel (\parallel) and perpendicular (\perp) to the laser. The combined collection efficiency, optical efficiency, and the overall electronic gain for the signals is denoted by G_x . The T^2 factor is the two-way transmission of the atmosphere, which accounts for both molecular and particulate scattering and absorption between the lidar and range r . A full description of the instrument channels are described in Hair et al. (2008).

Eqs. 3.1 and 3.2 are generalized such that the backscatter coefficients and transmission factors can be either from the atmosphere or ocean, depending on the altitude (or depth) of the scattering volume. Also, the transmission of the molecular backscatter through the iodine vapor filter, F , is based on either the atmosphere (*atm*) or the ocean (*ocn*) scattering regions, as they have different backscatter spectra and thus different iodine filter transmission factors, both of which are determined by laboratory calibrations and modeled molecular scattering spectra (Hair et al., 2008). Calibration operations are conducted during each flight to provide the relative gain ratios between the molecular (*mol*) and co-polarized (*par*) channels, G_{i2} , and between the co-polarized and cross-polarized (*per*) channels, G_{dep} , such that

$$G_{i2} = \frac{G_{par}}{G_{mol}}, \quad G_{dep} = \frac{G_{per}}{G_{par}}. \quad (4)$$

After the internal gain ratios (Eq. 4) are applied, the two signals (Eqs. 3.1 and 3.2) have the same relative gain. As will be shown below, the retrieval implements ratios of these two signals, and therefore neither the absolute gain nor any other absolute calibration factor is required to determine the surface backscatter.

To calculate the surface backscatter, the overall system response must be accounted for. The measured signal (P) is the convolution of the normalized system response, (L), with the ideal measured signal (i.e., infinite detection bandwidth and delta-function-like laser pulse), this signal being the gain-scaled (G), range-scaled ($\frac{1}{r^2}$), attenuated (T^2) backscatter coefficient (β , units $m^{-1}sr^{-1}$), which can be written as

$$P_{ideal}(r) = G \frac{1}{r^2} \beta(r) T^2(r). \quad (5a)$$

$$P(r) = G \int_{-\infty}^{\infty} L(r - \rho) P_{ideal}(\rho) d\rho. \quad (5b)$$

The system response includes the impact of the laser's temporal pulse shape, detector response, and analog electronic filter response.

To account for different scattering media and to better understand how the system response impacts the surface backscatter calculation, it is helpful to separate the total scattering channel, $P_{tot}(r)$, into three contributions: atmosphere [*atm*], surface [*surf*], and ocean [*ocn*] as follows:

$$P_{tot}(r) = P_{tot}^{atm}(r) + P_{tot}^{ocn}(r) + P_{tot}^{surf}(r). \quad (6)$$

Using Eq. 6, the last term in Eq. 7, $P_{tot}^{surf}(r)$, can be written as

$$P_{tot}^{surf}(r) = G_{mol} G_{i2} \int_{-\infty}^{\infty} L(r - \rho) \frac{1}{\rho^2} \beta_{surf} \delta(\rho - r_s) T^2(\rho) d\rho \quad (7a)$$

$$P_{tot}^{surf}(r) = G_{mol} G_{i2} L(r - r_s) \frac{1}{r_s^2} \beta_{surf} T^2(r_s) \quad (7b)$$

where the range to the ocean surface is r_s and the volume backscatter coefficient for the ocean surface is represented as $\beta_{surf} \delta(\rho - r_s)$ (units $m^{-1} sr^{-1}$), where $\delta(\rho - r_s)$ is the Dirac delta function centered at r_s . Figure 1 illustrates the vertical distributions of the measured signals P_{tot} (black) and P_{mol} (blue) along with the P_{tot}^{surf} (green) component of P_{tot} . Note that zero altitude is the location of the ocean surface.

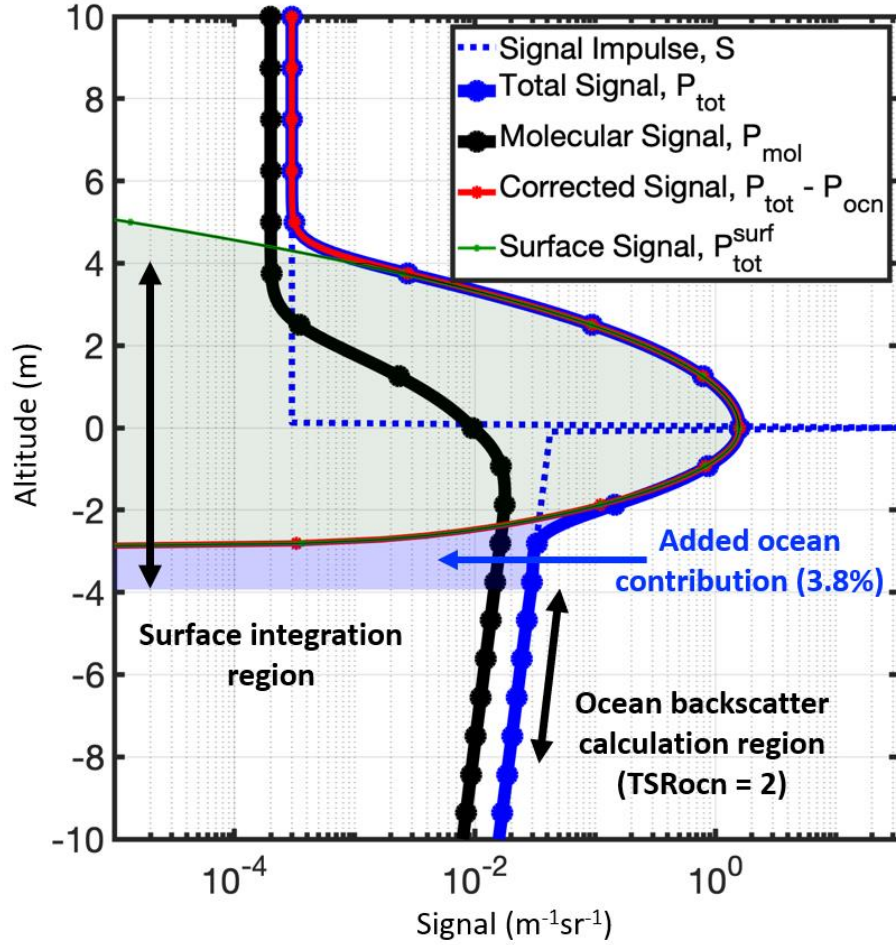


Figure 1: Visualization of HSRL-2 measurement signals as described in Eqs. 5 – 7. Dashed line denotes ideal total backscatter signal from the atmosphere, surface reflection, and the ocean subsurface. Blue and black lines denote measured signals from total and molecular scattering channels, respectively. Red and green lines show the ocean corrected signal and the ocean surface backscatter, respectively. Dots indicate the altitudes of digitized samples. The sampling rate is 120 MHz, resulting in a vertical spacing of 1.25 m in the atmosphere and 0.94 m in the ocean.

It is seen from Fig. 1 and Eq. 7b that the surface component P_{tot}^{surf} of the measured signal P_{tot} is not localized to the surface but is instead spread above and below the surface via convolution with the system response function. The atmosphere and ocean components of P_{tot} are also impacted by the convolution as is P_{mol} . Rearranging Eq. 7 and integrating the total surface backscatter component over the full vertical extent of the system response function (i.e., to $\pm Dz$), the surface response function can be eliminated in the representation of β_{surf} as shown in Eq. 8.

$$\beta_{surf} = \frac{1}{G_{mol} G_{i2}} \frac{r_s^2}{T^2(r_s)} \int_{r_s - \Delta z}^{r_s + \Delta z} P_{tot}^{surf}(r) dr \quad (8)$$

Of course, the measurement that can be accessed is P_{tot} , not the surface component P_{tot}^{surf} . If P_{tot} were substituted for P_{tot}^{surf} in Eq. 9, β_{surf} would be overestimated due to the contribution of ocean subsurface backscatter. The atmospheric contribution is negligible (i.e., $<0.05\%$) and can be ignored. The magnitude of the contribution of the ocean subsurface scattering depends on the level of ocean particulate (hydrosol) and as well as molecular seawater backscatter. The

magnitude of this scattering relative to the surface backscatter can impact the retrieved surface wind speed accuracy. For example, at $U = 7 \text{ m s}^{-1}$ and assuming pure seawater (i.e., no hydrosols), the integrated total surface signal would be 5.7% higher than the integrated surface backscatter. This results in a decrease of 0.75 m s^{-1} (-11% error) in the estimated surface wind speed. At a 20 m s^{-1} surface wind speed, the error in the calculated surface wind speeds results in a decrease by 2.7 m s^{-1} (-14% error). The ocean subsurface correction becomes less as the particulate scattering (or absorption) increases due to increased attenuation in the seawater and therefore contributes less over the integration window around the ocean surface. Therefore, the ocean subsurface contribution is higher for clear water compared to turbid water. For example, in the case illustrated in Fig. 1, the seawater particulate and molecular scattering are equal, resulting in a contribution of only 3.8% to the integrated surface backscatter as compared to the no particulate scattering noted above of 5.7%. The atmospheric signal contribution is much less (~ 100 times smaller) than the ocean subsurface signal and therefore its contribution is considered negligible. Fortunately, the high vertical resolution of the HSRL-2 instrument enables the ocean subsurface contribution to be estimated. The separation of the molecular signal also enables estimation of the two-way transmittance, T^2 , and gain factor, G_{mol} , in Eq. 8.

For the HSRL-2 instrument, the two-way transmittance is determined directly from the measured molecular channel, P_{mol} . The two-way total (particulate and molecular attenuation) transmittance to the surface can be calculated as follows,

$$T^2(r_{ns}) = \frac{1}{G_{mol}} \frac{\overline{P_{mol}(r_{ns})r_{ns}^2}}{F(r_{ns})\beta_m^{\parallel}(r_{ns})}, \quad (9)$$

where F is the iodine vapor filter function (known from lab and in-flight calibration), β_m^{\parallel} is the molecular backscatter coefficient for the atmosphere (computed from pressure and temperature data from a reanalysis model), and $\overline{P_{mol}(r_{ns})r_{ns}^2}$ is the range-scaled molecular channel signal near the ocean surface (where r_{ns} is the near-surface range). In practice, this is computed by averaging data from 60 m to 180 m above the surface. This range is somewhat arbitrary but is chosen as a balance between ensuring that the signal does not include any of the surface reflectance and low enough to capture most of the attenuation down to the surface. Substituting Eq. 9 into Eq. 8, one can solve for the surface backscatter,

$$\beta_{surf} = \frac{1}{G_{i2}} \frac{\int_{r_s-\Delta z}^{r_s+\Delta z} r^2 P_{tot}^{surf}(r) dr}{\frac{\overline{P_{mol}(r_{ns})r_{ns}^2}}{F(r_{ns})\beta_m^{\parallel}(r_{ns})}}. \quad (10)$$

To account for the ocean subsurface contributions to the measured signal, Eq. 5 can be rearranged as

$$P_{tot}^{surf}(r) = P_{tot} - P_{tot}^{atm}(r) - P_{tot}^{ocn}(r). \quad (11)$$

A benefit of the HSRL-2 retrieval algorithm is that one can use the molecular channel signal to determine the ocean signal near the surface (see Fig. 1). To determine the near-surface ocean signal, an estimate of the total ocean scattering ratio (TSR) is employed, which is the ratio of molecular + hydrosol backscatter divided by molecular backscatter. An estimate of the near-surface TSR, $(\overline{TSR_{ocn}})$ is computed using the quotient of the total and molecular channels ($P_{tot} /$

P_{mol}) averaged over a small range of depths just below the depth at which the surface signal response goes to zero, as follows:

$$\overline{TSR_{ocn}} \equiv \left(\frac{\beta_p + \beta_m}{\beta_m} \right) = \frac{F_{ocn}(r)}{G_{i2} \Delta r} \int_{r_s + \Delta z}^{r_s + 2\Delta z} \frac{P_{tot}(r)}{P_{mol}(r)} dr \quad (12)$$

where F_{ocn} accounts for the spectral transmission of the molecular seawater backscatter through the iodine vapor filter and is determined via in-flight and laboratory calibrations. The ocean subsurface component of the total channel backscatter is estimated as follows:

$$P_{tot}^{ocn}(r) = \overline{TSR_{ocn}} G_{i2} \frac{P_{mol}(r)}{F_{ocn}(r)}, \text{ below the surface } (r > r_s) \quad (13)$$

Here the assumption is that the TSR is vertically constant near the surface over the 0.5 s (~75 m horizontal resolution) integration of the lidar signals. Combining Eqs. 10, 11, and 13 and ignoring the atmospheric contribution P_{tot}^{atm} to the total channel signal, one can compute the absolute surface backscatter using the two measured channels as

$$\beta_{surf} = \frac{\int_{r_s - \Delta z}^{r_s + \Delta z} \left(\frac{P_{tot}(r)}{G_{i2}} - \overline{TSR_{ocn}} * P_{mol}(r) \right) r^2 dr}{\frac{P_{mol}(r_{ns}) r_{ns}^2}{F_{atm}(r_{ns}) \beta_m^{\parallel}(r_{ns})}}. \quad (14)$$

The use of the molecular channel in this way cancels out absolute system gain constant (G_{mol}), provides an estimate of the two-way transmittance of the atmosphere, and enables subtraction of ocean subsurface backscatter. It does not require precise knowledge of the system response function or any other assumptions. With Eq. 14, one can calculate the wave-slope variance through Eq. 2 and then use Eqs. 2.1 – 2.3 to derive surface wind speeds.

In addition to the specular reflection from the surface, whitecaps or sea foam can increase the lidar backscatter signal. As noted in Josset et al. (2010b), the contribution of scattering by the whitecaps on the ocean surface has been treated as Lambertian scattering. There is a wavelength dependence of the scattering at longer wavelengths due to the water absorption, based on measurements presented by Dierssen (2019) covering wavelengths from 0.4 – 2.5 μm . Measurements presented here are at 532 nm, a region of the visible spectrum where scattering from foam is relatively constant with wavelength. The contribution of whitecaps is typically modeled with a constant average reflectance and an effective area weighted fraction that varies with surface wind speed (Whitlock et al., 1982; Koepke, 1984; Gordon and Wang, 1994; Moore et al., 2000). Following Moore et al. (2000), we have estimated the average reflectance due to the whitecaps as a function of surface wind speed and the difference becomes $> 1 \text{ m s}^{-1}$ for surface wind speeds $> 15 \text{ m s}^{-1}$ based on this relationship. As presented below, there are limited data (49 data points) above 13.3 m s^{-1} that can be compared to the dropsonde surface wind speeds to evaluate this relationship. Moreover, since the correction depends on surface wind speed, an iterative calculation is required to use this relationship as the backscatter is dependent on wind speed.

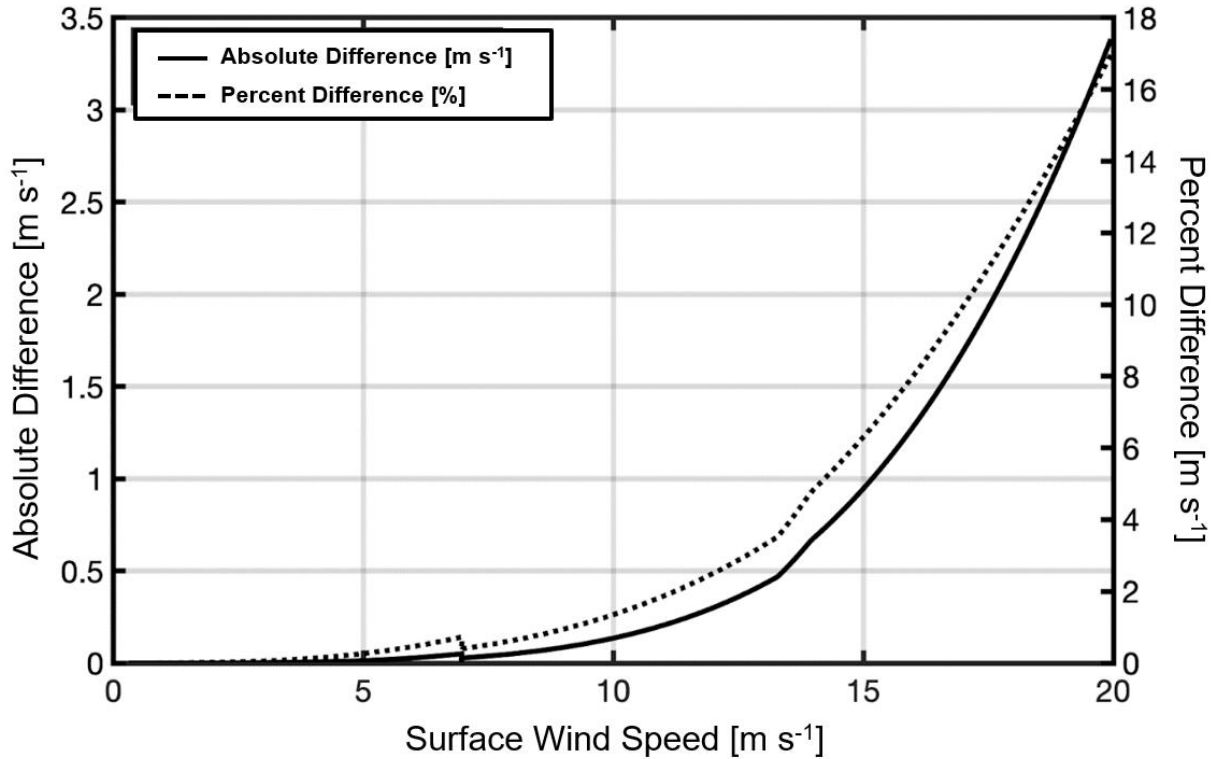


Figure 2. Estimated absolute difference in calculated surface wind speed if reflectance from whitecaps is not included. The lidar surface backscatter is higher than the specular reflectance if whitecaps are present, which results in a lower estimated surface wind speed if not accounted for in the retrieval.

Alternatively, Hu et al. (2008) used a full month of CALIPSO integrated surface depolarization ratio (ratio of the integrated cross polarized channel to the integrated co-polarized channel across the surface) and applied an empirical correction to the reflectance that was determined using AMSR-E data as the ground-truth data set to increase the correlation of the data sets. The correlation was based on much more data than the ACTIVATE matchups between HSRL-2 and dropsondes, limiting the utility of a similar analysis with the HSRL-2. In addition, there are significant differences in the configurations of CALIPSO and HSRL-2 that limit implementation of the same empirical relationship. First, CALIPSO's integrated surface depolarization includes the subsurface contributions due to its 30 m vertical resolution, whereas the HSRL-2 surface depolarization is integrated over only a few meters as shown in Fig. 1. Second, the CALIPSO data is based on global data, which is dominated by oligotrophic (clear) waters, whereas a significant fraction of the HSRL-2 - dropsonde comparisons are from eutrophic and mesotrophic waters near the coast and along the shelf. Third, there is a significant difference in footprint size between HSRL-2 and CALIPSO (8 m versus 90 m), with HSRL-2's instantaneous footprint area being greater than 2 orders of magnitude smaller and, considering HSRL-2's along-track averaging (100 laser shots) compared to CALIPSO's single shot data, greater than one order of magnitude smaller in terms of area over which surface depolarization is integrated.

2.5 Collocation and Statistical Procedures

Since surface wind speeds are the focus of this study, first the dropsonde wind speed data points closest to 10 m (altitude of $11.56 \text{ m} \pm 3.19 \text{ m}$ for the 577 points) above sea level are recorded for each launch (multiple launches per

flight) to allow meaningful comparison with the HSRL-2 surface wind speeds. Since one data point was taken per dropsonde for each flight, there are 160 recorded dropsonde measurements for 2020, 245 measurements for 2021, and 335 measurements for 2022. Then, the HSRL-2 surface wind speed retrieval closest in space and time to the corresponding dropsonde measurement is recorded. Collocation between the HSRL-2 and the dropsondes is constrained to below 30 km horizontally and below 15 minutes temporally to remove outliers while trying to maximize the number of data points to be used in the study. Further constraining these distance and time conditions would eliminate more data points with negligible improvement to the statistics as shown by Figs. S1 and S2 in the supplement. Due to missing data in the HSRL-2 data set and the removal of outliers based on collocation constraints, 577 data points are available for comparison between the dropsondes and the HSRL-2 (Fig. 3).

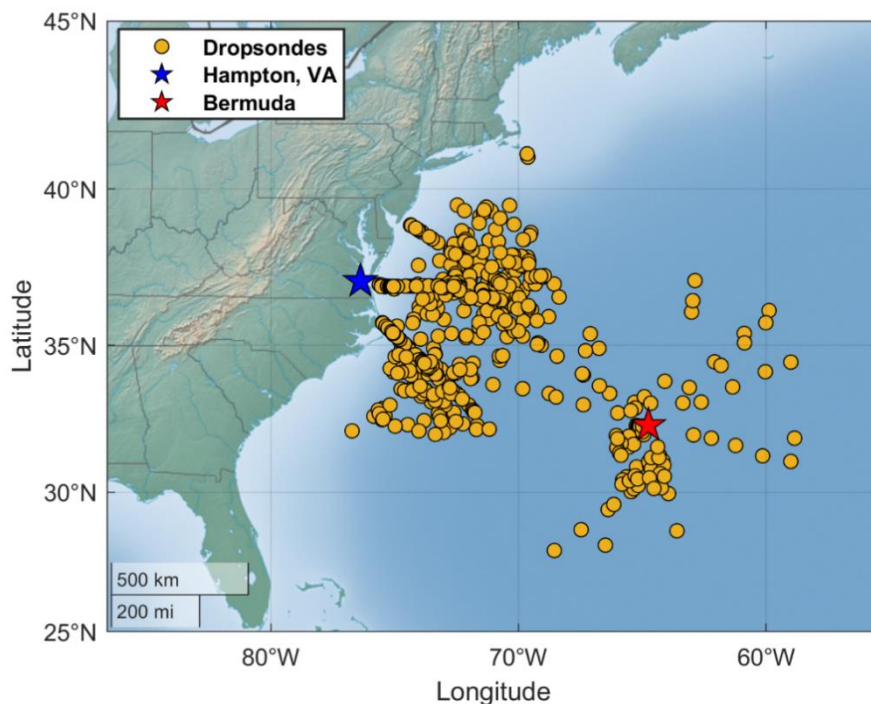


Figure 3: Map of 577 ACTIVATE dropsondes launched from the King Air between 2020 and 2022 that are used to evaluate the HSRL-2 surface wind speed retrievals introduced in this study.

After the surface wind speed data are prepared using the procedure above, scatterplots along with the correlation coefficient (r), linear regression, and ordinary least squares bisector regression (OLS-bisector) are used to visually demonstrate how well HSRL-2 surface wind speed data match dropsonde data and show any potential variability in the data. Since OLS-bisector is less common than linear regression, a brief explanation of their differences is provided. In linear regression, X is treated as the independent variable while Y is treated as the dependent variable. In other words, one observes how Y varies with changes to fixed X values. OLS-bisector is known as an errors-in-variable regression technique, where X and Y are both dependent variables and thus both subject to error. OLS-bisector regresses Y on X (standard OLS) and then regresses X on Y (inverse OLS), then bisects the angle of these two regression lines (Ricker, 1973). Although other errors-in-variable techniques exist (e.g., Deming regression, orthogonal distance regression), OLS-bisector is chosen because it calculates the error present in both data sets using

the bisector rather than assuming an error a priori like the examples mentioned (Wu and Yu, 2018). After performing these regressions, histograms of surface wind speed deltas, which are defined as HSRL-2 surface wind speed minus dropsonde surface wind speed, are created to show the distribution and spread of the data more easily. The mean and standard deviation (STD), of the surface wind speed deltas are computed and then used to define the mean error (mean \pm STD). This metric is used to evaluate how accurately the HSRL-2 retrieves surface wind speeds.

3 Results and Discussion

3.1 Case Studies

Before delving into the HSRL-2 – dropsonde surface wind speed intercomparisons in full statistical detail, surface wind speed data from two ACTIVATE research flights are analyzed: Research Flight 29 on 28 August 2020 and Research Flight 14 on 1 March 2020. These flights are analyzed to demonstrate the ability of the HSRL-2 to 1) provide profiles that show the spatial variability of surface wind speed over time, which are beneficial to observe phenomena like sea-surface temperature dynamics and cloud evolution and 2) sample the surface in broken cloud scenes, showing that the retrievals are not limited to cloud- and aerosol-free conditions like in Hu et al. (2008).

3.1.1 Research Flight 29 on 28 August 2020

Research Flight 29 was a near cloud-free day where an above average number of dropsondes were launched and ACTIVATE’s aircraft were coordinated with the CALIPSO satellite overpass. These conditions allow for the examination of how the high horizontal spatial resolution of the HSRL-2 (~75 m along track as mentioned in Sect. 2.4) influences its retrievals and how the data can be used to track sea surface temperature (SST) gradients common to the WNAO (Painemal et al., 2021) as seen in Fig. 4. Note that Fig. 4a uses SST data from Modern-Era Retrospective Analysis for Research and Applications, Version 2 (MERRA-2) (Gelaro et al., 2017) to contextualize the SST gradients present in the WNAO, and no comparisons with MERRA-2 surface wind speed data are performed in this study.

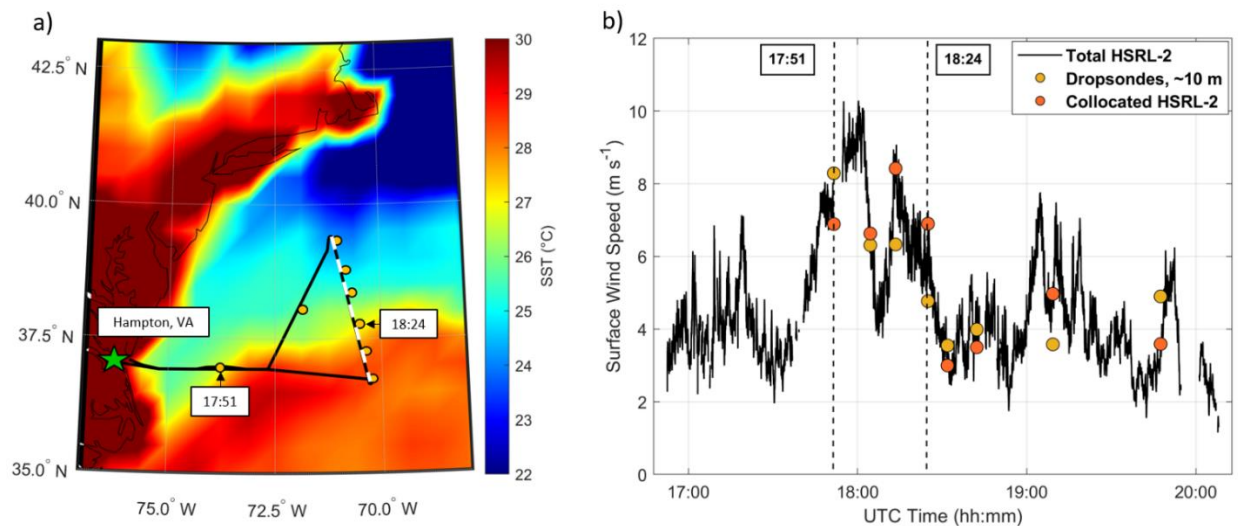


Figure 4: a) Flight map of King Air (black line) and dropsondes (dark yellow circles) overlaid onto map of MERRA-2 mean sea-surface temperature (SST) data (Gmao, 2015) for Research Flight 29 on 28 August 2020. White dashed line corresponds

to the CALIPSO overpass coincident with King Air flight path. Time stamps represent where the King Air crosses over sharp SST changes associated with the Gulf Stream. b) Time series of surface wind speed data from HSRL-2 and dropsondes for the same flight, where the black solid line signifies total HSRL-2 surface wind speed data and circles indicate collocated surface wind speed data points. Black dashed lines represent time stamps of interest as indicated in a).

It is seen that changes in the HSRL-2 surface wind speeds (Fig. 4b) correspond with changes in SST (Fig. 4a), especially seen at 17:51 and 18:24 (UTC throughout paper). As the aircraft approaches and crosses the SST boundary at 17:51 (i.e., SST increasing), there is a corresponding increase in surface wind speeds. The reverse observation can be seen when the aircraft approaches and crosses the boundary at 18:24 (i.e., SST decreasing), where surface wind speeds noticeably decrease. Although further analysis is needed to rigorously examine the relationship between surface wind speed and SST, these observations show that the HSRL-2 has the high horizontal spatial resolution needed to probe the fine-scale variability of surface wind speeds and has the potential to improve atmospheric modeling of MABL processes. These profiles capture the spatial gradients in surface wind speeds that would otherwise not be available with the dropsondes alone, since these instruments can only take point measurements as they drop vertically to the surface and therefore cannot provide the horizontal spatial extent like the derived HSRL-2 surface wind speed product can.

3.1.2 Research Flight 14 on 1 March 2020

Next, Research Flight 14 is shown in Fig. 5 to demonstrate the ability of the HSRL-2 to sample in broken cloud scenes. This flight along with the associated morning flight on 1 March 2020 have been the subject of several studies owing to its coincidence with cold air outbreak conditions (see cloud streets in Fig. 5a) and a flight strategy that allowed for detailed characterization of the evolving aerosol-cloud system as a function of distance offshore (Seethala et al., 2021; Chen et al., 2022; Li et al., 2022; Tornow et al., 2022; Sorooshian et al., 2023). The morning flight focused on a location with very detailed characterization including stacked level flight legs (i.e., termed a “wall”) with the Falcon flying below, in, and above clouds, with the King Air flying aloft to further characterize the same region. The afternoon flight consisted of both aircraft flying back to that same location, adjusting the sampling strategy to fly along the boundary layer wind direction in a quasi-Lagrangian fashion to keep studying the evolution of the air mass characterized in the morning. The afternoon flight is chosen because it shows the full range of cloud conditions from

clear to completely overcast. Therefore, the HSRL-2 surface wind speed retrievals are able to be evaluated in this range of conditions.

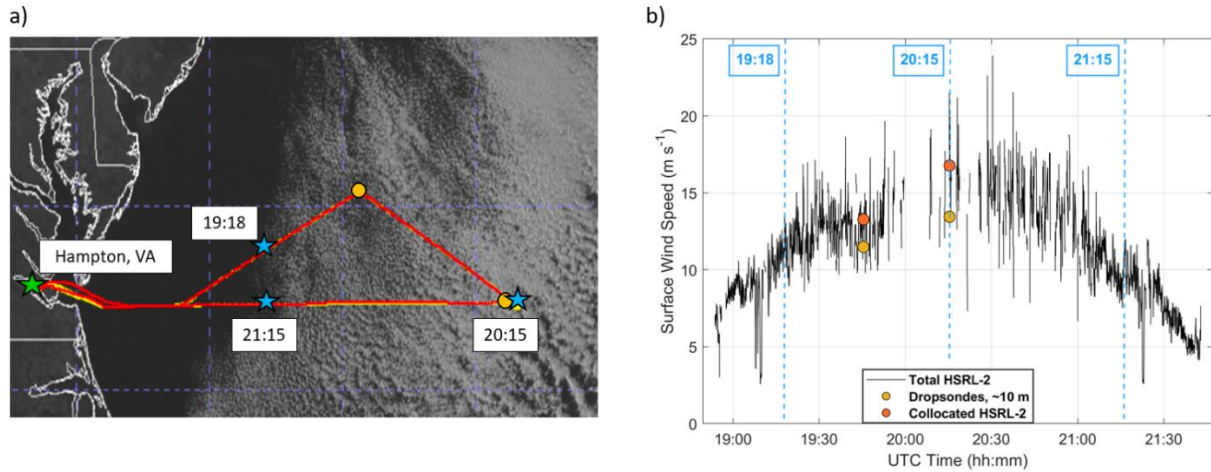


Figure 5: a) Flight map of the King Air (red line), Falcon (yellow line), and dropsondes (dark yellow circles) overlaid onto Geostationary Operational Environmental Satellite (GOES-16) cloud imagery for Research Flight 14 on 1 March 2020. Blue stars represent time stamps where the King Air crosses over from cloud-free to cloudy areas. b) Time series of surface wind speed data from HSRL-2 and dropsondes for the same flight, where lines signify total HSRL-2 surface wind speed data and circles indicate collocated surface wind speed data points. Blue dashed lines represent time stamps of interest as indicated in a).

As the aircraft approaches the cloud scene at 19:18, there is a noticeable and steady increase of HSRL-2 surface wind speeds. The reverse observation is seen when the aircraft approaches 21:15, where the HSRL-2 surface wind speeds start to decrease steadily. As highlighted in the 28 August 2020 case study, the high horizontal spatial resolution of the HSRL-2 retrievals enables these spatial gradients to be observed. Another important takeaway is the HSRL-2 is still able to sample the surface in cloud scenes, as seen by the almost complete surface wind speed profile in Fig. 5b. Although a gap in data occurs at 20:15 where cloud cover is most substantial, some retrievals are still present in that area. The reason is that the HSRL-2 can probe the surface through gaps between clouds, allowing for the surface wind speed retrievals to take place. Although the HSRL-2 retrievals would be unavailable in overcast cloud scenes, the ability of the instrument to sample the surface in broken cloud fields and not just aerosol- and cloud-free scenes is a significant benefit of the lidar and the HSRL technique.

3.2 HSRL-2 – Dropsonde Comparisons

Now, the collocated HSRL-2 retrievals and dropsonde measurements of surface wind speed are compared and the results are shown in Fig. 6.

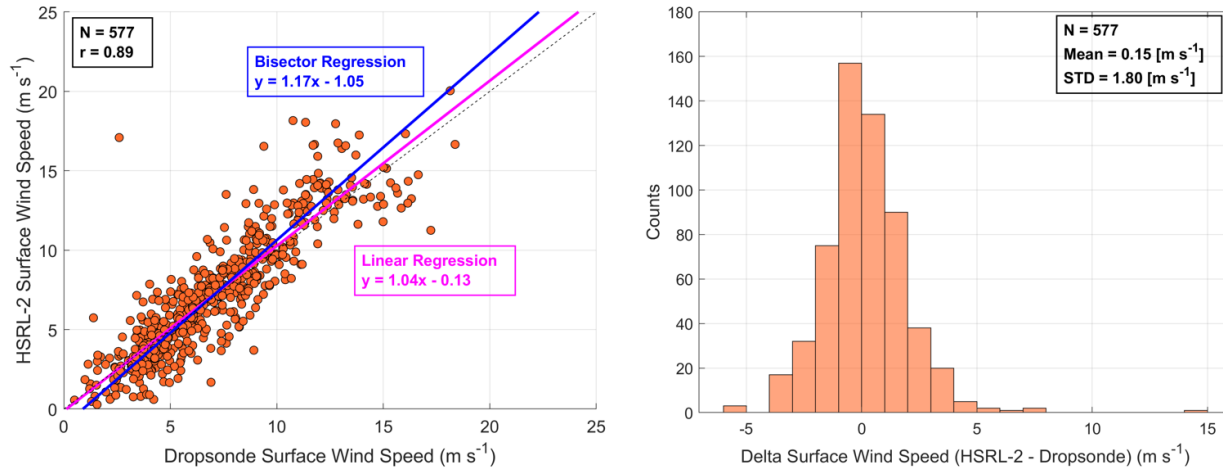


Figure 6: Scatterplots with associated histograms for HSRL-2 – dropsonde collocated surface wind speed data points using ACTIVATE’s 2020 – 2022 data set. N represents the number of data points.

The comparison yields correlation coefficients of 0.89, slopes of 1.04 and 1.17, and y-intercepts of -0.13 m s^{-1} and -1.05 m s^{-1} for linear and bisector regressions, respectively. Note that the correlation coefficients are the same for linear and bisector regressions throughout this analysis, so they are listed as one value throughout Sect. 3.2. Using the mean and STD values in the same figure, the mean error or accuracy of the HSRL-2 surface wind speed retrievals is $0.15 \text{ m s}^{-1} \pm 1.80 \text{ m s}^{-1}$. These results show that on average, the HSRL-2 slightly overestimates surface wind speeds and the estimation can be off by about 2 m s^{-1} in either direction.

Now that the HSRL-2 retrievals have been broadly evaluated, Fig. 7 shows how their accuracy varies per 1 m s^{-1} interval in surface wind speed. This plot also provides the opportunity to compare the Hu et al. (2008) model with the models proposed by Cox and Munk (1954) and Wu (1990) to see if some of the error in the HSRL-2 retrievals can be attributed to model characteristics.

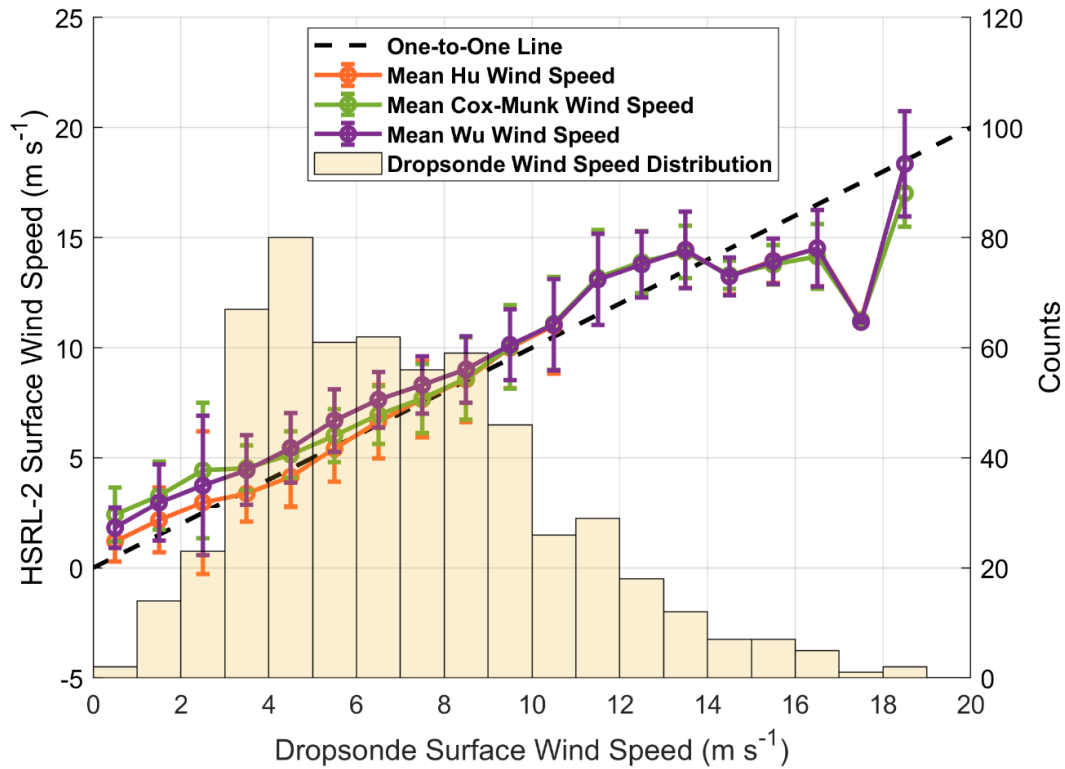


Figure 7: HSRL-2 surface wind speed using Hu, Cox-Munk, and Wu models versus mean dropsonde surface wind speed calculated per 1 m s^{-1} bin. A histogram of dropsonde surface wind speeds is also included to show their distribution.

It is seen that the mean Cox-Munk and Wu surface wind speed values are higher than the mean Hu values from 0 m s^{-1} to 7 m s^{-1} , showing that the Cox-Munk and Wu relationships overestimate dropsonde surface wind speeds more than the Hu relationship. The variability (i.e., STD) around the mean per bin is similar between the three models, which is 1.59 m s^{-1} for Hu, 1.43 m s^{-1} for Cox-Munk, and 1.55 m s^{-1} for Wu on average. Although similar, the STD of the Hu surface wind speeds found here is $\sim 0.4 \text{ m s}^{-1}$ lower than the one found in Fig. 6. This could be attributed to an STD not being able to be calculated for the 17 to 18 m s^{-1} bin since it only contained one point.

Although it is apparent Cox-Munk and Wu retrievals overestimate dropsonde observations for surface wind speeds below 7 m s^{-1} , it is still unclear which of the models perform better overall. Therefore, the y-axis from Fig. 7 is converted to wave-slope space and the result of this modification is shown in Fig. 8. HSRL-2 wave-slope is used because it directly reports the original measurements of surface reflectance rather than estimated values of surface wind speed. Using the original data ensures that uncertainty is coming from the actual HSRL-2 – dropsonde comparisons rather than from potential errors in the conversion from wave-slope to surface wind speed.

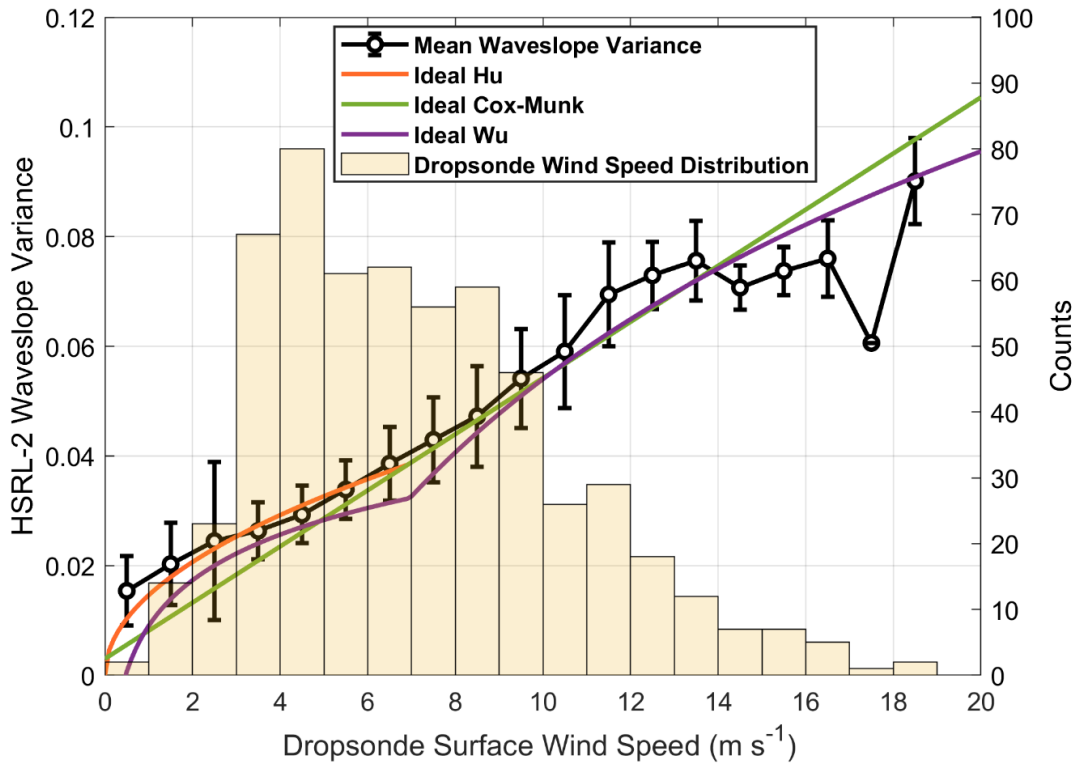


Figure 8: HSRL-2 wave-slope variance versus mean dropsonde surface wind speed calculated per 1 m s⁻¹ bin. Ideal Hu, Cox-Munk, and Wu distributions are included to show how well observed dropsonde data match with each parameterization. A histogram of dropsonde surface wind speeds is also included to show their distribution.

From Fig. 8, it is more easily seen how the dropsonde surface wind speed distribution compares with Hu, Cox-Munk, and Wu parameterizations. Dropsonde surface wind speeds match quite closely to Hu and Cox-Munk parameterizations as opposed to the Wu parameterization between 7 m s⁻¹ and 13.3 m s⁻¹, although some divergence is seen above ~10.5 m s⁻¹. However, a critical observation that is more apparent in Fig. 8 than Fig. 7 is how the dropsonde data most resemble the Hu distribution for surface wind speeds below 7 m s⁻¹. This improvement is substantial, especially since most of the surface wind speeds in ACTIVATE fall into this category. Surface wind speeds above 13.3 m s⁻¹ substantially diverge from all models, especially above 16 m s⁻¹. As mentioned previously, there are few surface wind speed observations in this category, so more measurements are necessary to make meaningful comparisons between the two data sets. Overall, Figs. 7 and 8 demonstrate the benefits of using the Hu parameterization in this study and why surface wind speeds above 13.3 m s⁻¹ are not the main focus of the comparisons in this section. Further analysis is warranted to rigorously compare the performance of various surface reflectance models and potentially apply corrections (i.e., whitecap correction for surface wind speeds above 13.3 m s⁻¹), but the

aim of this paper is to evaluate LARC's HSRL-2 surface wind speed retrieval algorithm using the available ground-truth dropsonde measurements.

Now that the Hu relationship has been deemed the more effective model through the preliminary analysis shown in Figs. 7 and 8, a more rigorous statistical analysis is performed for surface wind speeds 1) below 7 m s^{-1} and 2) between 7 m s^{-1} and 13.3 m s^{-1} to assess the overall accuracy of the HSRL-2 retrievals in these categories (Fig. 9).

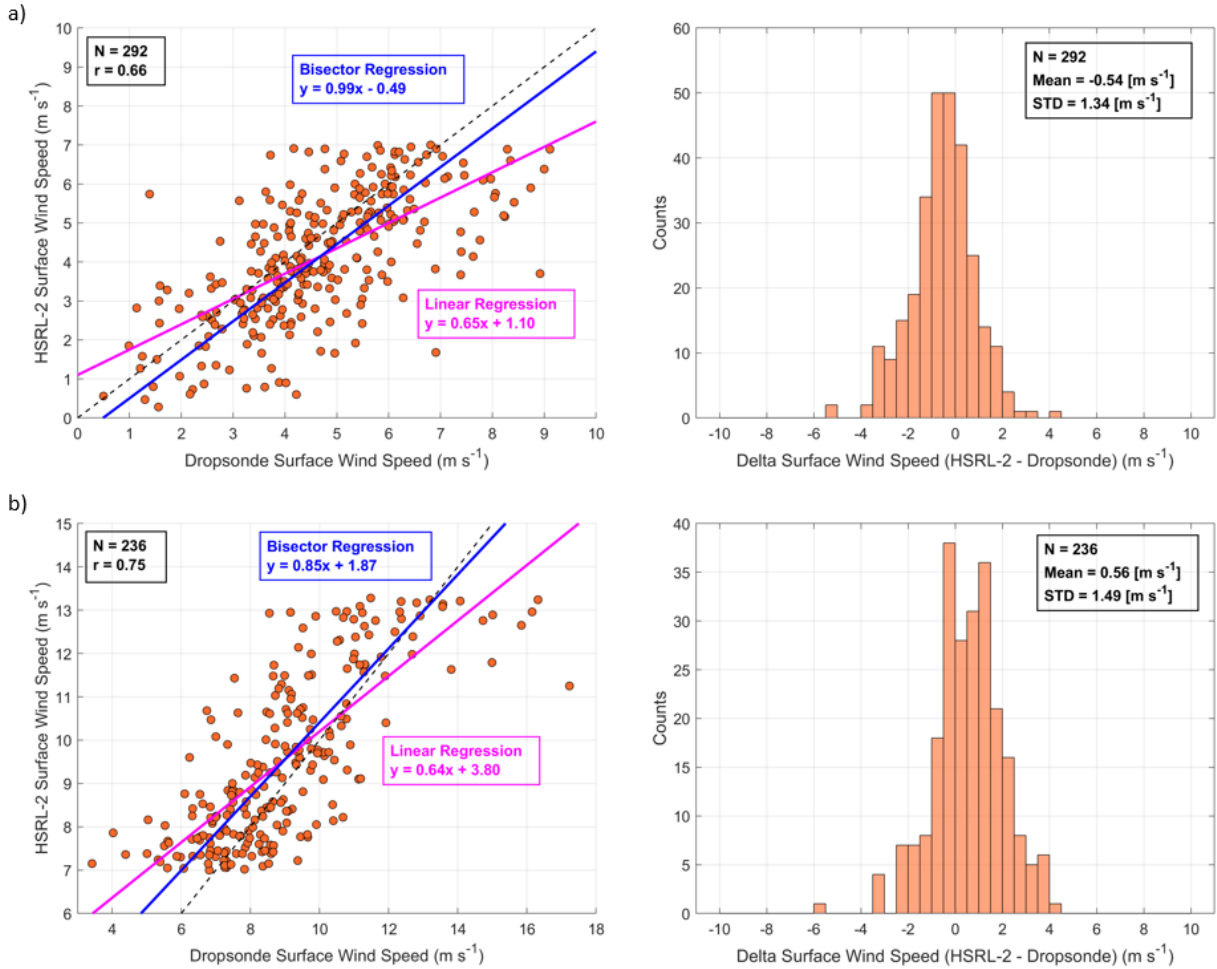


Figure 9: Scatterplots with associated histograms for HSRL-2 – dropsonde collocated surface wind speed data points for a) surface wind speeds $< 7 \text{ m s}^{-1}$ and b) surface wind speeds between 7 m s^{-1} and 13.3 m s^{-1} . Note that x- and y-axis ranges vary to better showcase results in individual panels. N represents the number of data points.

Intercomparisons for surface wind speeds below 7 m s^{-1} (Fig. 9a) show correlation coefficients of 0.66, slopes of 0.65 and 0.99, and y-intercepts of 1.10 m s^{-1} and -0.49 m s^{-1} for linear and bisector regressions, respectively. The accuracy of the HSRL-2 retrievals is calculated to be $-0.54 \text{ m s}^{-1} \pm 1.34 \text{ m s}^{-1}$, showing that the HSRL-2 on average underestimates surface wind speeds and this estimation could vary by $\pm 1.34 \text{ m s}^{-1}$. For surface wind speeds between 7 m s^{-1} and 13.3 m s^{-1} (Fig. 9b), correlation coefficients of 0.75, slopes of 0.64 and 0.85, and y-intercepts of 3.80 m s^{-1} and 1.87 m s^{-1} are reported for linear and bisector regressions, respectively. The mean error of $0.56 \text{ m s}^{-1} \pm 1.49 \text{ m s}^{-1}$ shows that the HSRL-2 overpredicts surface wind speeds by about $\sim 0.5 \text{ m s}^{-1}$ on average with a variability of $\pm \sim 1.5 \text{ m s}^{-1}$. Therefore, the means from both categories average out to $\sim 0 \text{ m s}^{-1}$ since they are approximately the same but in

opposite directions. Separating the data into these categories highlight an important result that could not be seen in the cumulative data (Fig. 6): one can expect bias of up to $\sim 0.5 \text{ m s}^{-1}$ in either direction and error of up to $\sim 1.5 \text{ m s}^{-1}$ on average for most HSRL-2 surface wind speed retrievals in ACTIVATE.

The data are then divided into winter and summer deployments (dates provided in Sect. 2.1) as shown in Fig. 10 to assess the HSRL-2's retrieval accuracy in different seasons.

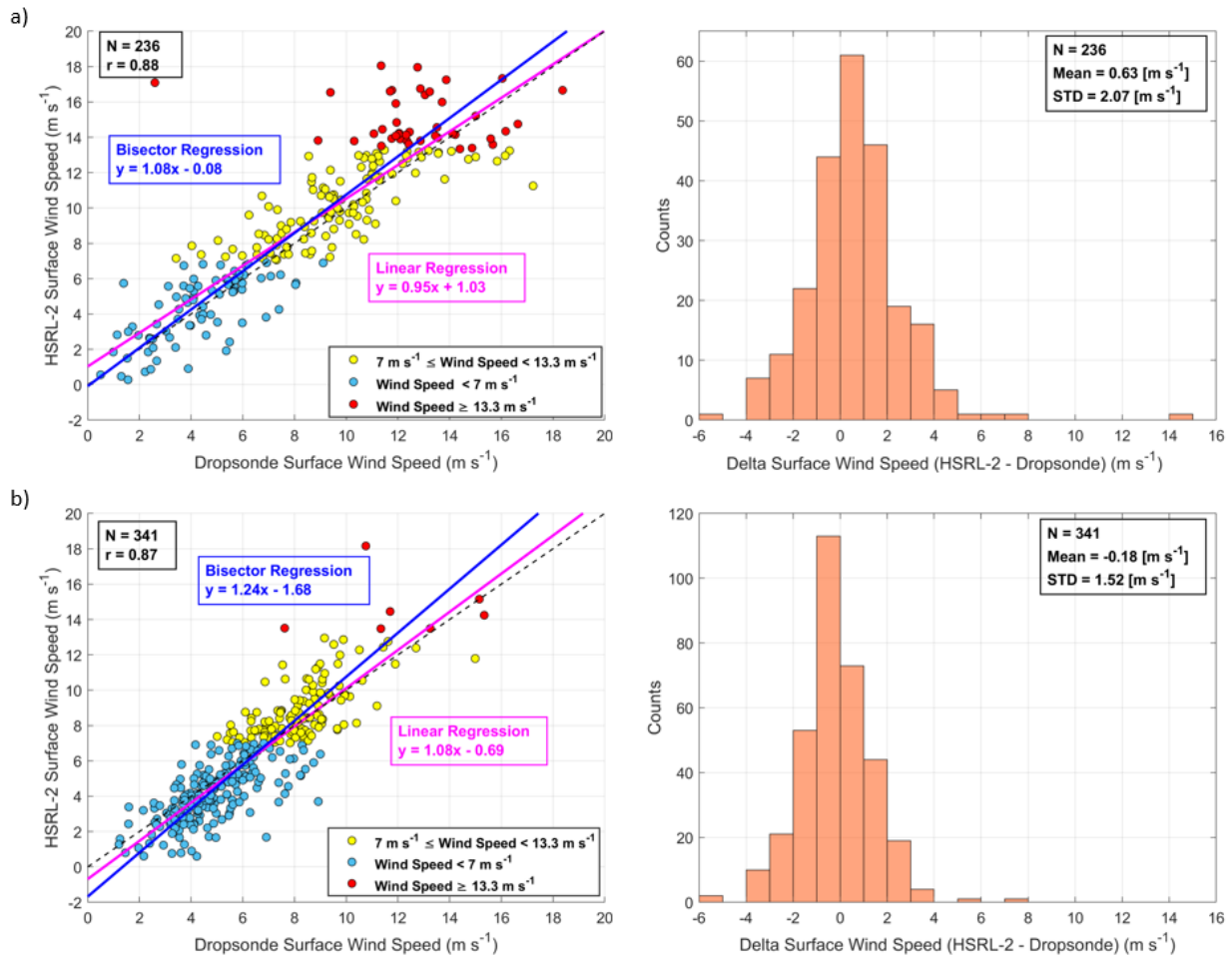


Figure 10: Scatterplots with associated histograms for HSRL-2 – dropsonde collocated surface wind speed data points for a) winter and b) summer deployments. Data are highlighted based on surface wind speed categories: $7 \text{ m s}^{-1} \leq \text{Wind Speed} < 13.3 \text{ m s}^{-1}$, Wind Speed $< 7 \text{ m s}^{-1}$, and Wind Speed $\geq 13.3 \text{ m s}^{-1}$. N represents the number of data points.

As seen in Fig. 10a, the winter surface wind speed intercomparisons show correlation coefficients of 0.88, slopes of 0.95 and 1.08, and y-intercepts of 1.03 m s^{-1} and -0.08 m s^{-1} for linear and bisector regressions, respectively. The summer surface wind speed intercomparisons (Fig. 10b) have correlations of 0.87, slopes of 1.08 and 1.24, and y-intercepts of -0.69 m s^{-1} and -1.68 m s^{-1} . Finally, the mean errors for winter and summer, respectively, are reported as $0.63 \text{ m s}^{-1} \pm 2.07 \text{ m s}^{-1}$ and $-0.18 \pm 1.52 \text{ m s}^{-1}$. It is seen that the error in the HSRL-2 estimations of surface wind speeds is larger for winter than summer, most likely due to the higher fraction of surface wind speeds above 13.3 m s^{-1} and lower fraction of them below 7 m s^{-1} in the winter. This observation makes sense because of the increased

presence of clouds, precipitation, and whitecaps for the higher surface wind speeds observed in the winter. These observations show that HSRL-2 retrievals of surface wind speed are more accurate in the summer over the winter. However, the HSRL-2 can still make numerous accurate retrievals as shown by the Fig. 10 and the 1 March 2020 research flight discussions. Caution must still be exercised when using data from days featuring turbulent meteorological conditions that could induce whitecaps and/or substantial cloud cover that could limit or even prevent the HSRL-2 from sampling the surface.

Statistics evaluating the HSRL-2 surface wind speed retrievals (Figs. 6, 9, 10) are summarized in Table 1 for convenience.

Table 1: Summary of all HSRL-2 – dropsonde surface wind speed comparison statistics shown in Figs. 6, 9, and 10. The two values for slope and y-intercept refer to those for the linear and bisector regressions, in that order. R values are the same for both linear and bisector regressions, so they are listed as one value.

	N	r	Slope	Y-intercept [m s ⁻¹]	Mean Error [m s ⁻¹]
Overall	577	0.89	1.04/1.17	-0.13/-1.05	0.15 ± 1.80
Wind Speed < 7 m s⁻¹	292	0.66	0.65/0.99	1.10/-0.49	-0.54 ± 1.34
7 m s⁻¹ ≤ Wind Speed < 13.3 m s⁻¹	236	0.75	0.64/0.85	3.80/1.87	0.56 ± 1.49
Winter	236	0.88	0.95/1.08	1.03/-0.08	0.63 ± 2.07
Summer	341	0.87	1.08/1.24	-0.69/-1.68	-0.18 ± 1.52

4. Conclusions

This study introduces a new 10 m surface wind speed product from NASA Langley Research Center’s (LaRC’s) nadir-viewing High Spectral Resolution Lidar – generation 2 (HSRL-2) instrument and demonstrates its use and accuracy. The HSRL-2 retrievals are evaluated using NCAR AVAPS dropsonde surface wind speed data collected during the NASA ACTIVATE field campaign. Comparisons of HSRL-2 and dropsonde surface wind speeds show correlations of 0.89, slopes of 1.04 and 1.17, y-intercepts of -0.13 m s⁻¹ and -1.05 m s⁻¹ for linear and bisector regressions, respectively. The accuracy of the HSRL-2 retrievals, as denoted by mean error, is calculated to be 0.15 m s⁻¹ ± 1.80 m s⁻¹. It is also observed that the dropsonde surface wind speed measurements most closely match with the Hu et al. (2008) wind speed – wave-slope variance model than the Cox and Munk (1954) and Wu (1990) models for surface wind speeds below 7 m s⁻¹, which is an important finding because most ACTIVATE surface wind speeds fall into this category. After this overview of model performance, the HSRL-2 retrievals for surface wind speeds separated into below 7 m s⁻¹ and between 7 m s⁻¹ and 13.3 m s⁻¹ categories are then evaluated in more detail. For surface wind speeds below 7 m s⁻¹, correlations of 0.66, slopes of 0.65 and 0.99, and y-intercepts of 1.10 m s⁻¹ and -0.49 m s⁻¹ are found and the accuracy of the retrievals is found to be -0.54 m s⁻¹ ± 1.34 m s⁻¹. Surface wind speeds between 7 m s⁻¹ and 13.3 m s⁻¹ show correlations of 0.75, slopes of 0.64 and 0.85, and y-intercepts of 3.80 m s⁻¹ and 1.87 m s⁻¹ and the retrieval accuracy is shown to be 0.56 m s⁻¹ ± 1.49 m s⁻¹. Statistics are not reported for surface wind speeds above 13.3 m s⁻¹ because there are too few points in this category to make meaningful comparisons. These results showcase an important observation not seen in the cumulative results, which is that the HSRL-2 estimates surface wind speeds with

a bias of $\pm \sim 0.5 \text{ m s}^{-1}$ and an error of $\pm \sim 1.5 \text{ m s}^{-1}$. Lastly, the data are divided into winter and summer deployments (dates denoted in Sect. 2.1) to assess how the HSRL-2 performs between seasons. The winter surface wind speed data comparisons show correlations of 0.88, slopes of 0.95 and 1.08, and y-intercepts of 1.03 m s^{-1} and -0.08 m s^{-1} and the summer data show correlations of 0.87, slopes of 1.08 and 1.24, and y-intercepts of -0.69 m s^{-1} and -1.68 m s^{-1} (linear and bisector regressions, respectively). The accuracy of the lidar retrievals is reported as $0.63 \text{ m s}^{-1} \pm 2.07 \text{ m s}^{-1}$ and $-0.18 \text{ m s}^{-1} \pm 1.52 \text{ m s}^{-1}$ for winter and summer, respectively. These findings show that HSRL-2 retrievals are more accurate in the summer than in winter, but still provide substantial ($N = 236$) and accurate surface wind speed data in winter as well.

This retrieval method offers a new path forward in airborne field work for the acquisition of surface wind speed data at a high spatial ($\sim 75 \text{ m}$ along track) and time (0.5 s) resolution, as demonstrated with two case study flights (Research Flight 29 on 28 August 2020 and Research Flight 14 on 1 March 2020). The high horizontal spatial resolution of the HSRL-2 allows it to probe the fine-scale variability of surface wind speeds over time. As a result, the instrument provides near-continuous profiles of surface wind speeds over time that correspond to MABL phenomena such as SST dynamics and cloud evolution. Another important conclusion about the HSRL-2 surface retrievals is that the instrument can detect the surface in broken cloud scenes and are not limited to aerosol-free conditions like in Hu et al. (2008). Overall, having such data can benefit model assimilation efforts and consequently several scientific applications related to air-sea interactions such as estimating heat fluxes, gas exchange, sea salt emissions and aerosol transport, and cloud life cycle.

Forthcoming work will continue assessments of surface wind speed measurements during ACTIVATE by comparing dropsonde data to in situ measurements taken by the Turbulent Air Motion Measurement System (TAMMS) onboard the Falcon aircraft at its various altitude flight legs (between 120 m and 5 km) (Thornhill et al., 2003). Additional work is also warranted to assess the surface wind speed retrievals performed by ACTIVATE's other remote sensor, the Research Scanning Polarimeter (RSP), to fully demonstrate ACTIVATE's remote sensing capabilities.

Data Availability

ACTIVATE airborne data are available through <https://asdc.larc.nasa.gov/project/ACTIVATE> (ACTIVATE Science Team, 2020). MERRA-2 mean sea surface temperature data are taken from the 2d, 1-Hourly, Time-Averaged, Single-Level, Assimilation, Surface Flux Diagnostics V5.12.4 (M2T1NXFLX) product found at https://disc.gsfc.nasa.gov/datasets/M2T1NXFLX_5.12.4/summary (doi.org/10.5067/7MCPBJ41Y0K6). GOES-16 data are from https://asdc.larc.nasa.gov/ACTIVATE/ACTIVATE-Satellite_1 (doi: 10.5067/ASDC/SUBORBITAL/ACTIVATE-Satellite_1).

Author Contribution

SD performed all analyses with input from all co-authors. SD, JH, RF, CH, JR, and AS prepared manuscript with all co-authors involved in review/editing. TS, DH, SS, and CR conducted flight scientist duties on the King Air and helped with preparation and deployment of dropsondes. JH, RF, MF, CH, BC, DH, SS, TS, and EC were responsible for the

HSRL-2 instrumentation and KT, CR, and HV were responsible for the NCAR AVAPS dropsonde instrumentation collected and subsequent archival of surface wind speed data sets needed to conduct this analysis. JH, JR, YH, RF, CH, and BC all contributed with formulation of HSRL-2 retrieval algorithm.

Competing Interests

The authors declare that they have no conflict of interest.

Disclaimer

Publisher's note: Copernicus Publications remains neutral with regard to jurisdictional claims in published maps and institutional affiliations.

Acknowledgements

The work was funded by ACTIVATE, a NASA Earth Venture Suborbital-3 (EVS-3) investigation funded by NASA's Earth Science Division and managed through the Earth System Science Pathfinder Program Office. We thank pilots and aircraft maintenance personnel of NASA Langley Research Services Directorate for successfully conducting ACTIVATE flights. The MERRA-2 1-Hourly, Time-Averaged, Single-Level, Assimilation, Surface Flux Diagnostics V5.12.4 (M2T1NXFLX) data used in this effort were acquired as part of the activities of NASA's Science Mission Directorate and are archived and distributed by the Goddard Earth Sciences (GES) Data and Information Services Center (DISC).

Financial support

University of Arizona investigators were funded by NASA grant no. 80NSSC19K0442.

References

ACTIVATE Science Team: Aerosol Cloud meTeorology Interactions oVer the western ATlantic Experiment Data [dataset], doi.org/10.5067/SUBORBITAL/ACTIVATE/DATA001, 2020.

Aldhaif, A. M., Lopez, D. H., Dadashazar, H., and Sorooshian, A.: Sources, frequency, and chemical nature of dust events impacting the United States East Coast, *Atmospheric Environment*, 231, 117456, <https://doi.org/10.1016/j.atmosenv.2020.117456>, 2020.

Bedka, K. M., Nehrir, A. R., Kavaya, M., Barton-Grimley, R., Beaubien, M., Carroll, B., Collins, J., Cooney, J., Emmitt, G. D., Greco, S., Kooi, S., Lee, T., Liu, Z., Rodier, S., and Skofronick-Jackson, G.: Airborne lidar observations of wind, water vapor, and aerosol profiles during the NASA Aeolus calibration and validation (Cal/Val) test flight campaign, *Atmos. Meas. Tech.*, 14, 4305-4334, 10.5194/amt-14-4305-2021, 2021.

Bellouin, N., Quaas, J., Gryspeerdt, E., Kinne, S., Stier, P., Watson-Parris, D., Boucher, O., Carslaw, K. S., Christensen, M., Daniau, A.-L., Dufresne, J.-L., Feingold, G., Fiedler, S., Forster, P., Gettelman, A., Haywood, J. M., Lohmann, U., Malavelle, F., Mauritsen, T., McCoy, D. T., Myhre, G., Mülmenstädt, J., Neubauer, D., Possner, A., Rugenstein, M., Sato, Y., Schulz, M., Schwartz, S. E., Sourdeval, O., Storelvmo, T., Toll, V., Winker, D., and Stevens, B.: Bounding Global Aerosol Radiative Forcing of Climate Change, *Reviews of Geophysics*, 58, e2019RG000660, <https://doi.org/10.1029/2019RG000660>, 2020.

Brunke, M. A., Cutler, L., Urzua, R. D., Corral, A. F., Crosbie, E., Hair, J., Hostetler, C., Kirschler, S., Larson, V., Li, X.-Y., Ma, P.-L., Minke, A., Moore, R., Robinson, C. E., Scarino, A. J., Schlosser, J., Shook, M., Sorooshian, A., Lee Thornhill, K., Voigt, C., Wan, H., Wang, H., Winstead, E., Zeng, X., Zhang, S., and Ziemba, L. D.: Aircraft Observations of Turbulence in Cloudy and Cloud-Free Boundary Layers Over the Western North Atlantic Ocean From ACTIVATE and Implications for the Earth System Model Evaluation and Development, *Journal of Geophysical Research: Atmospheres*, 127, e2022JD036480, <https://doi.org/10.1029/2022JD036480>, 2022.

Burton, S. P., Ferrare, R. A., Hostetler, C. A., Hair, J. W., Rogers, R. R., Obland, M. D., Butler, C. F., Cook, A. L., Harper, D. B., and Froyd, K. D.: Aerosol classification using airborne High Spectral Resolution Lidar measurements – methodology and examples, *Atmos. Meas. Tech.*, 5, 73-98, 10.5194/amt-5-73-2012, 2012.

Burton, S. P., Hostetler, C. A., Cook, A. L., Hair, J. W., Seaman, S. T., Scola, S., Harper, D. B., Smith, J. A., Fenn, M. A., Ferrare, R. A., Saide, P. E., Chemyakin, E. V., and Müller, D.: Calibration of a high spectral resolution lidar using a Michelson interferometer, with data examples from ORACLES, *Appl. Opt.*, 57, 6061-6075, 10.1364/AO.57.006061, 2018.

Carvalho, D.: An Assessment of NASA's GMAO MERRA-2 Reanalysis Surface Winds, *Journal of Climate*, 32, 8261-8281, <https://doi.org/10.1175/JCLI-D-19-0199.1>, 2019.

Chemyakin, E., Stamnes, S., Hair, J., Burton, S. P., Bell, A., Hostetler, C., Ferrare, R., Chowdhary, J., Moore, R., Ziemba, L., Crosbie, E., Robinson, C., Shook, M., Thornhill, L., Winstead, E., Hu, Y., van Diedenhoven, B., and Cairns, B.: Efficient single-scattering look-up table for lidar and polarimeter water cloud studies, *Opt. Lett.*, 48, 13-16, 10.1364/OL.474282, 2023.

Chen, J., Wang, H., Li, X., Painemal, D., Sorooshian, A., Thornhill, K. L., Robinson, C., and Shingler, T.: Impact of Meteorological Factors on the Mesoscale Morphology of Cloud Streets during a Cold-Air Outbreak over the Western North Atlantic, *Journal of the Atmospheric Sciences*, 79, 2863-2879, <https://doi.org/10.1175/JAS-D-22-0034.1>, 2022.

Christoudias, T., Pozzer, A., and Lelieveld, J.: Influence of the North Atlantic Oscillation on air pollution transport, *Atmos. Chem. Phys.*, 12, 869-877, 10.5194/acp-12-869-2012, 2012.

Corral, A. F., Choi, Y., Crosbie, E., Dadashazar, H., DiGangi, J. P., Diskin, G. S., Fenn, M., Harper, D. B., Kirschler, S., Liu, H., Moore, R. H., Nowak, J. B., Scarino, A. J., Seaman, S., Shingler, T., Shook, M. A., Thornhill, K. L., Voigt,

C., Zhang, B., Ziemba, L. D., and Sorooshian, A.: Cold Air Outbreaks Promote New Particle Formation Off the U.S. East Coast, *Geophysical Research Letters*, 49, e2021GL096073, <https://doi.org/10.1029/2021GL096073>, 2022.

Cox, C. and Munk, W.: Measurement of the Roughness of the Sea Surface from Photographs of the Sun's Glitter, *J. Opt. Soc. Am.*, 44, 838-850, 10.1364/JOSA.44.000838, 1954.

Creilson, J. K., Fishman, J., and Wozniak, A. E.: Intercontinental transport of tropospheric ozone: a study of its seasonal variability across the North Atlantic utilizing tropospheric ozone residuals and its relationship to the North Atlantic Oscillation, *Atmos. Chem. Phys.*, 3, 2053-2066, 10.5194/acp-3-2053-2003, 2003.

Dadashazar, H., Painemal, D., Alipanah, M., Brunke, M., Chellappan, S., Corral, A. F., Crosbie, E., Kirschler, S., Liu, H., Moore, R. H., Robinson, C., Scarino, A. J., Shook, M., Sinclair, K., Thornhill, K. L., Voigt, C., Wang, H., Winstead, E., Zeng, X., Ziemba, L., Zuidema, P., and Sorooshian, A.: Cloud drop number concentrations over the western North Atlantic Ocean: seasonal cycle, aerosol interrelationships, and other influential factors, *Atmos. Chem. Phys.*, 21, 10499-10526, 10.5194/acp-21-10499-2021, 2021.

Dierssen, H. M.: Hyperspectral Measurements, Parameterizations, and Atmospheric Correction of Whitecaps and Foam From Visible to Shortwave Infrared for Ocean Color Remote Sensing, *Frontiers in Earth Science*, 7, 10.3389/feart.2019.00014, 2019.

Ferrare, R., Hair, J., Hostetler, C., Shingler, T., Burton, S. P., Fenn, M., Clayton, M., Scarino, A. J., Harper, D., Seaman, S., Cook, A., Crosbie, E., Winstead, E., Ziemba, L., Thornhill, L., Robinson, C., Moore, R., Vaughan, M., Sorooshian, A., Schlosser, J. S., Liu, H., Zhang, B., Diskin, G., DiGangi, J., Nowak, J., Choi, Y., Zuidema, P., and Chellappan, S.: Airborne HSRL-2 measurements of elevated aerosol depolarization associated with non-spherical sea salt, *Frontiers in Remote Sensing*, 4, 10.3389/frsen.2023.1143944, 2023.

Gelaro, R., McCarty, W., Suárez, M. J., Todling, R., Molod, A., Takacs, L., Randles, C. A., Darmenov, A., Bosilovich, M. G., Reichle, R., Wargan, K., Coy, L., Cullather, R., Draper, C., Akella, S., Buchard, V., Conaty, A., da Silva, A. M., Gu, W., Kim, G.-K., Koster, R., Lucchesi, R., Merkova, D., Nielsen, J. E., Partyka, G., Pawson, S., Putman, W., Rienecker, M., Schubert, S. D., Sienkiewicz, M., and Zhao, B.: The Modern-Era Retrospective Analysis for Research and Applications, Version 2 (MERRA-2), *Journal of Climate*, 30, 5419-5454, <https://doi.org/10.1175/JCLI-D-16-0758.1>, 2017.

GMAO: MERRA-2 tavg1_2d_flux_Nx: 2d, 1-Hourly, Time-Averaged, Single-Level, Assimilation, Surface Flux Diagnostics V5.12.4 [dataset], 2015.

Gordon, H. R. and Wang, M.: Influence of oceanic whitecaps on atmospheric correction of ocean-color sensors, *Appl. Opt.*, 33, 7754-7763, 10.1364/AO.33.007754, 1994.

Hair, J. W., Hostetler, C. A., Cook, A. L., Harper, D. B., Ferrare, R. A., Mack, T. L., Welch, W., Izquierdo, L. R., and Hovis, F. E.: Airborne High Spectral Resolution Lidar for profiling aerosol optical properties, *Appl. Opt.*, 47, 6734-6752, 10.1364/AO.47.006734, 2008.

Hu, Y., Stamnes, K., Vaughan, M., Pelon, J., Weimer, C., Wu, D., Cisewski, M., Sun, W., Yang, P., Lin, B., Omar, A., Flittner, D., Hostetler, C., Treppe, C., Winker, D., Gibson, G., and Santa-Maria, M.: Sea surface wind speed estimation from space-based lidar measurements, *Atmos. Chem. Phys.*, 8, 3593-3601, 10.5194/acp-8-3593-2008, 2008.

Josset, D., Pelon, J., and Hu, Y.: Multi-Instrument Calibration Method Based on a Multiwavelength Ocean Surface Model, *IEEE Geoscience and Remote Sensing Letters*, 7, 195-199, 10.1109/LGRS.2009.2030906, 2010a.

Josset, D., Pelon, J., Protat, A., and Flamant, C.: New approach to determine aerosol optical depth from combined CALIPSO and CloudSat ocean surface echoes, *Geophysical Research Letters*, 35, <https://doi.org/10.1029/2008GL033442>, 2008.

Josset, D., Zhai, P.-W., Hu, Y., Pelon, J., and Lucker, P. L.: Lidar equation for ocean surface and subsurface, *Opt. Express*, 18, 20862-20875, 10.1364/OE.18.020862, 2010b.

Kiliyanpilakkil, V. P. and Meskhidze, N.: Deriving the effect of wind speed on clean marine aerosol optical properties using the A-Train satellites, *Atmos. Chem. Phys.*, 11, 11401-11413, 10.5194/acp-11-11401-2011, 2011.

Kirschler, S., Voigt, C., Anderson, B., Campos Braga, R., Chen, G., Corral, A. F., Crosbie, E., Dadashazar, H., Ferrare, R. A., Hahn, V., Hendricks, J., Kaufmann, S., Moore, R., Pöhlker, M. L., Robinson, C., Scarino, A. J., Schollmayer, D., Shook, M. A., Thornhill, K. L., Winstead, E., Ziemba, L. D., and Sorooshian, A.: Seasonal updraft speeds change cloud droplet number concentrations in low-level clouds over the western North Atlantic, *Atmos. Chem. Phys.*, 22, 8299-8319, 10.5194/acp-22-8299-2022, 2022.

Koepke, P.: Effective reflectance of oceanic whitecaps, *Appl. Opt.*, 23, 1816-1824, 10.1364/AO.23.001816, 1984.

Labzovskii, L. D., van Zadelhoff, G. J., Tilstra, L. G., de Kloe, J., Donovan, D. P., and Stoffelen, A.: High sensitivity of Aeolus UV surface returns to surface reflectivity, *Scientific Reports*, 13, 17552, 10.1038/s41598-023-44525-5, 2023.

Lamb, P. J. and Pepler, R. A.: North Atlantic Oscillation: Concept and an Application, *Bulletin of the American Meteorological Society*, 68, 1218-1225, [https://doi.org/10.1175/1520-0477\(1987\)068<1218:NAOCAA>2.0.CO;2](https://doi.org/10.1175/1520-0477(1987)068<1218:NAOCAA>2.0.CO;2), 1987.

Li, Q., Jacob, D. J., Bey, I., Palmer, P. I., Duncan, B. N., Field, B. D., Martin, R. V., Fiore, A. M., Yantosca, R. M., Parrish, D. D., Simmonds, P. G., and Oltmans, S. J.: Transatlantic transport of pollution and its effects on surface

ozone in Europe and North America, *Journal of Geophysical Research: Atmospheres*, 107, ACH 4-1-ACH 4-21, <https://doi.org/10.1029/2001JD001422>, 2002.

Li, X.-Y., Wang, H., Chen, J., Endo, S., George, G., Cairns, B., Chellappan, S., Zeng, X., Kirschler, S., Voigt, C., Sorooshian, A., Crosbie, E., Chen, G., Ferrare, R. A., Gustafson, W. I., Hair, J. W., Kleb, M. M., Liu, H., Moore, R., Painemal, D., Robinson, C., Scarino, A. J., Shook, M., Shingler, T. J., Thornhill, K. L., Tornow, F., Xiao, H., Ziemba, L. D., and Zuidema, P.: Large-Eddy Simulations of Marine Boundary Layer Clouds Associated with Cold-Air Outbreaks during the ACTIVATE Campaign. Part I: Case Setup and Sensitivities to Large-Scale Forcings, *Journal of the Atmospheric Sciences*, 79, 73-100, <https://doi.org/10.1175/JAS-D-21-0123.1>, 2022.

Li, Z., Lemmerz, C., Paffrath, U., Reitebuch, O., and Witschas, B.: Airborne Doppler Lidar Investigation of Sea Surface Reflectance at a 355-nm Ultraviolet Wavelength, *Journal of Atmospheric and Oceanic Technology*, 27, 693-704, <https://doi.org/10.1175/2009JTECHA1302.1>, 2010.

Mardi, A. H., Dadashazar, H., Painemal, D., Shingler, T., Seaman, S. T., Fenn, M. A., Hostetler, C. A., and Sorooshian, A.: Biomass Burning Over the United States East Coast and Western North Atlantic Ocean: Implications for Clouds and Air Quality, *Journal of Geophysical Research: Atmospheres*, 126, e2021JD034916, <https://doi.org/10.1029/2021JD034916>, 2021.

Martin, C. and Suhr, I.: NCAR/EOL Atmospheric Sounding Processing ENvironment (ASPEN) software. Version 3.4.5. [dataset], 2021.

Moore, K. D., Voss, K. J., and Gordon, H. R.: Spectral reflectance of whitecaps: Their contribution to water-leaving radiance, *Journal of Geophysical Research: Oceans*, 105, 6493-6499, <https://doi.org/10.1029/1999JC900334>, 2000.

Murphy, A. and Hu, Y.: Retrieving Aerosol Optical Depth and High Spatial Resolution Ocean Surface Wind Speed From CALIPSO: A Neural Network Approach, *Frontiers in Remote Sensing*, 1, 10.3389/frsen.2020.614029, 2021.

Nair, A. K. M. and Rajeev, K.: Multiyear CloudSat and CALIPSO Observations of the Dependence of Cloud Vertical Distribution on Sea Surface Temperature and Tropospheric Dynamics, *Journal of Climate*, 27, 672-683, <https://doi.org/10.1175/JCLI-D-13-00062.1>, 2014.

Neukermans, G., Harmel, T., Galí, M., Rudorff, N., Chowdhary, J., Dubovik, O., Hostetler, C., Hu, Y., Jamet, C., Knobelspiesse, K., Lehahn, Y., Litvinov, P., Sayer, A. M., Ward, B., Boss, E., Koren, I., and Miller, L. A.: Harnessing remote sensing to address critical science questions on ocean-atmosphere interactions, *Elementa: Science of the Anthropocene*, 6, 10.1525/elementa.331, 2018.

Painemal, D., Corral, A. F., Sorooshian, A., Brunke, M. A., Chellappan, S., Afzali Gorooh, V., Ham, S.-H., O'Neill, L., Smith Jr., W. L., Tselioudis, G., Wang, H., Zeng, X., and Zuidema, P.: An Overview of Atmospheric Features Over the Western North Atlantic Ocean and North American East Coast—Part 2: Circulation, Boundary Layer, and

Clouds, *Journal of Geophysical Research: Atmospheres*, 126, e2020JD033423, <https://doi.org/10.1029/2020JD033423>, 2021.

Painemal, D., Chellappan, S., Smith Jr., W. L., Spangenberg, D., Park, J. M., Ackerman, A., Chen, J., Crosbie, E., Ferrare, R., Hair, J., Kirschler, S., Li, X.-Y., McComiskey, A., Moore, R. H., Sanchez, K., Sorooshian, A., Tornow, F., Voigt, C., Wang, H., Winstead, E., Zeng, X., Ziemba, L., and Zuidema, P.: Wintertime Synoptic Patterns of Midlatitude Boundary Layer Clouds Over the Western North Atlantic: Climatology and Insights From In Situ ACTIVATE Observations, *Journal of Geophysical Research: Atmospheres*, 128, e2022JD037725, <https://doi.org/10.1029/2022JD037725>, 2023.

Paiva, V., Kampel, M., and Camayo, R.: Comparison of Multiple Surface Ocean Wind Products with Buoy Data over Blue Amazon (Brazilian Continental Margin), *Advances in Meteorology*, 2021, 6680626, 10.1155/2021/6680626, 2021.

Ricker, W. E.: Linear Regressions in Fishery Research, *Journal of the Fisheries Research Board of Canada*, 30, 409-434, 10.1139/f73-072, 1973.

Scarino, A. J., Obland, M. D., Fast, J. D., Burton, S. P., Ferrare, R. A., Hostetler, C. A., Berg, L. K., Lefer, B., Haman, C., Hair, J. W., Rogers, R. R., Butler, C., Cook, A. L., and Harper, D. B.: Comparison of mixed layer heights from airborne high spectral resolution lidar, ground-based measurements, and the WRF-Chem model during CalNex and CARES, *Atmos. Chem. Phys.*, 14, 5547-5560, 10.5194/acp-14-5547-2014, 2014.

Schlosser, J. S., Stamnes, S., Burton, S. P., Cairns, B., Crosbie, E., Van Diedenhoven, B., Diskin, G., Dmitrovic, S., Ferrare, R., Hair, J. W., Hostetler, C. A., Hu, Y., Liu, X., Moore, R. H., Shingler, T., Shook, M. A., Thornhill, K. L., Winstead, E., Ziemba, L., and Sorooshian, A.: Polarimeter + Lidar-Derived Aerosol Particle Number Concentration, *Frontiers in Remote Sensing*, 3, 10.3389/frsen.2022.885332, 2022.

Schulien, J. A., Behrenfeld, M. J., Hair, J. W., Hostetler, C. A., and Twardowski, M. S.: Vertically- resolved phytoplankton carbon and net primary production from a high spectral resolution lidar, *Opt. Express*, 25, 13577-13587, 10.1364/OE.25.013577, 2017.

Seethala, C., Zuidema, P., Edson, J., Brunke, M., Chen, G., Li, X.-Y., Painemal, D., Robinson, C., Shingler, T., Shook, M., Sorooshian, A., Thornhill, L., Tornow, F., Wang, H., Zeng, X., and Ziemba, L.: On Assessing ERA5 and MERRA2 Representations of Cold-Air Outbreaks Across the Gulf Stream, *Geophysical Research Letters*, 48, e2021GL094364, <https://doi.org/10.1029/2021GL094364>, 2021.

Sorooshian, A., Corral, A. F., Braun, R. A., Cairns, B., Crosbie, E., Ferrare, R., Hair, J., Kleb, M. M., Hossein Mardi, A., Maring, H., McComiskey, A., Moore, R., Painemal, D., Scarino, A. J., Schlosser, J., Shingler, T., Shook, M., Wang, H., Zeng, X., Ziemba, L., and Zuidema, P.: Atmospheric Research Over the Western North Atlantic Ocean

Region and North American East Coast: A Review of Past Work and Challenges Ahead, *Journal of Geophysical Research: Atmospheres*, 125, e2019JD031626, <https://doi.org/10.1029/2019JD031626>, 2020.

Sorooshian, A., Anderson, B., Bauer, S. E., Braun, R. A., Cairns, B., Crosbie, E., Dadashazar, H., Diskin, G., Ferrare, R., Flagan, R. C., Hair, J., Hostetler, C., Jonsson, H. H., Kleb, M. M., Liu, H., MacDonald, A. B., McComiskey, A., Moore, R., Painemal, D., Russell, L. M., Seinfeld, J. H., Shook, M., Smith, W. L., Thornhill, K., Tselioudis, G., Wang, H., Zeng, X., Zhang, B., Ziemba, L., and Zuidema, P.: Aerosol–Cloud–Meteorology Interaction Airborne Field Investigations: Using Lessons Learned from the U.S. West Coast in the Design of ACTIVATE off the U.S. East Coast, *Bulletin of the American Meteorological Society*, 100, 1511-1528, <https://doi.org/10.1175/BAMS-D-18-0100.1>, 2019.

Sorooshian, A., Alexandrov, M. D., Bell, A. D., Bennett, R., Betito, G., Burton, S. P., Buzanowicz, M. E., Cairns, B., Chemyakin, E. V., Chen, G., Choi, Y., Collister, B. L., Cook, A. L., Corral, A. F., Crosbie, E. C., van Dierenhoven, B., DiGangi, J. P., Diskin, G. S., Dmitrovic, S., Edwards, E. L., Fenn, M. A., Ferrare, R. A., van Gilst, D., Hair, J. W., Harper, D. B., Hilario, M. R. A., Hostetler, C. A., Jester, N., Jones, M., Kirschler, S., Kleb, M. M., Kusterer, J. M., Leavor, S., Lee, J. W., Liu, H., McCauley, K., Moore, R. H., Nied, J., Notari, A., Nowak, J. B., Painemal, D., Phillips, K. E., Robinson, C. E., Scarino, A. J., Schlosser, J. S., Seaman, S. T., Seethala, C., Shingler, T. J., Shook, M. A., Sinclair, K. A., Smith Jr, W. L., Spangenberg, D. A., Stammes, S. A., Thornhill, K. L., Voigt, C., Vömel, H., Wasilewski, A. P., Wang, H., Winstead, E. L., Zeider, K., Zeng, X., Zhang, B., Ziemba, L. D., and Zuidema, P.: Spatially-coordinated airborne data and complementary products for aerosol, gas, cloud, and meteorological studies: The NASA ACTIVATE dataset, *ESSD*, 2023, 1-79, 10.5194/essd-2023-109, 2023.

Sun, K., Dai, G., Wu, S., Reitebuch, O., Baars, H., Liu, J., and Zhang, S.: Correlation between marine aerosol optical properties and wind fields over remote oceans with use of spaceborne lidar observations, *EGUsphere*, 2023, 1-34, 10.5194/egusphere-2023-433, 2023.

Thornhill, K. L., Anderson, B. E., Barrick, J. D. W., Bagwell, D. R., Friesen, R., and Lenschow, D. H.: Air motion intercomparison flights during Transport and Chemical Evolution in the Pacific (TRACE-P)/ACE-ASIA, *Journal of Geophysical Research: Atmospheres*, 108, <https://doi.org/10.1029/2002JD003108>, 2003.

Tornow, F., Ackerman, A. S., Fridlind, A. M., Cairns, B., Crosbie, E. C., Kirschler, S., Moore, R. H., Painemal, D., Robinson, C. E., Seethala, C., Shook, M. A., Voigt, C., Winstead, E. L., Ziemba, L. D., Zuidema, P., and Sorooshian, A.: Dilution of Boundary Layer Cloud Condensation Nucleus Concentrations by Free Tropospheric Entrainment During Marine Cold Air Outbreaks, *Geophysical Research Letters*, 49, e2022GL098444, <https://doi.org/10.1029/2022GL098444>, 2022.

van Dierenhoven, B., Hasekamp, O. P., Cairns, B., Schuster, G. L., Stammes, S., Shook, M. A., and Ziemba, L. D.: Remote sensing of aerosol water fraction, dry size distribution and soluble fraction using multi-angle, multi-spectral polarimetry, *EGUsphere*, 2022, 1-41, 10.5194/egusphere-2022-670, 2022.

Venkata, S. L. and Reagan, J. A.: Aerosol Retrievals from CALIPSO Lidar Ocean Surface Returns, *Remote Sensing*, 8, 1006, 2016.

Vömel, H. and Dunion, J.: Chapter 10 - Aircraft dropsonde campaigns, in: *Field Measurements for Passive Environmental Remote Sensing*, edited by: Nalli, N. R., Elsevier, 185-194, <https://doi.org/10.1016/B978-0-12-823953-7.00021-6>, 2023.

Vömel, H., Goodstein, M., Tudor, L., Witte, J., Fuchs-Stone, Ž., Sentić, S., Raymond, D., Martinez-Claros, J., Juračić, A., Maithel, V., and Whitaker, J. W.: High-resolution in situ observations of atmospheric thermodynamics using dropsondes during the Organization of Tropical East Pacific Convection (OTREC) field campaign, *Earth Syst. Sci. Data*, 13, 1107-1117, 10.5194/essd-13-1107-2021, 2021.

Whitlock, C. H., Bartlett, D. S., and Gurganus, E. A.: Sea foam reflectance and influence on optimum wavelength for remote sensing of ocean aerosols, *Geophysical Research Letters*, 9, 719-722, 1982.

Wu, C. and Yu, J. Z.: Evaluation of linear regression techniques for atmospheric applications: the importance of appropriate weighting, *Atmos. Meas. Tech.*, 11, 1233-1250, 10.5194/amt-11-1233-2018, 2018.

Wu, J.: Mean square slopes of the wind-disturbed water surface, their magnitude, directionality, and composition, *Radio Science*, 25, 37-48, <https://doi.org/10.1029/RS025i001p00037>, 1990.

APPENDIX B: CLOSING THE GAP BETWEEN IN-SITU AND REMOTELY SENSED AEROSOL PARTICLE PROPERTIES

The following article will be submitted to the journal Atmospheric Measurement Techniques (AMT).

Closing the gap between in-situ and remotely sensed aerosol particle properties

Sanja Dmitrovic¹, Joseph S. Schlosser^{2,3,*}, Ryan Bennett⁴, Brian Cairns⁵, Gao Chen², Brian L. Collister², Johnathan W. Hair², Michael Jones^{2,6}, Michael A. Shook², Armin Sorooshian^{1,7,8}, Kenneth L. Thornhill^{2,6}, Luke D. Ziemba², Snorre Stamnes²

¹University of Arizona, James C. Wyant College of Optical Sciences, Tucson, AZ 85721, USA

²NASA Langley Research Center, Hampton, VA 23681, USA

³NASA Postdoctoral Program, NASA Langley Research Center, Hampton, VA 23681, USA

⁴Bay Area Environmental Research Institute, Moffett Field, CA 94035, USA

⁵NASA Goddard Institute for Space Studies, New York, NY 10025, USA

⁶Analytical Mechanics Associates, Hampton, VA 23681, USA

⁷University of Arizona, Department of Hydrology and Atmospheric Sciences, Tucson, AZ 85721, USA

⁸University of Arizona, Department of Chemical and Environmental Engineering, Tucson, AZ 85721, USA

*These authors contributed equally to this work.

Correspondence to: Armin Sorooshian (armin@arizona.edu)

Abstract. Remote sensing platforms such as lidars and polarimeters are increasingly used to understand atmospheric aerosols and their role in critical marine atmospheric boundary layer (MABL) processes. Therefore, it is important to ensure their retrievals of aerosol optical and microphysical properties are consistent with measurements taken by in-situ instruments (i.e., external closure analysis). However, in-situ instruments 1) provide dry ($< 40\%$ RH) aerosol measurements while remote sensors retrieve aerosol properties at ambient RH and 2) can only sample fine-mode particles (particle diameter $D < 5 \mu\text{m}$) due to aircraft sampling inlet cutoffs, making the two data sets difficult to compare. To address these limitations, we introduce the In Situ Aerosol Retrieval Algorithm (ISARA), which converts dry in-situ aerosol data into ambient, humidified data for both fine- and coarse-mode aerosol particles. We leverage the NASA Aerosol Cloud meTeorology Interactions oVer the western ATlantic Experiment (ACTIVATE) field campaign data set to perform this closure study due to the numerous and robust statistics collected as well as the presence of diverse aerosol, cloud, and meteorological conditions in the study region. We compare airborne aerosol retrievals of HSRL-2 total ambient aerosol extinction at 532 nm (ϵ_{532nm}), jointly-retrieved HSRL-2 + RSP aerosol particle number concentration (N_a), RSP fine-mode aerosol effective radius ($r_{eff,f}$), and fine-mode and total single scattering albedo (SSA_f, SSA_t) at 555 nm with corresponding measurements from ACTIVATE's in-situ instruments. We demonstrate that 1) for marine environments, appropriate a priori assumptions for coarse-mode aerosol allow for at least partially successful closure between in-situ measurements and lidar/polarimetric retrievals and 2) successful, systematic closure is possible between in-situ and RSP aerosol data, which has not been shown in the literature to date.

1 Introduction

Researchers extensively study atmospheric aerosol particles due to these particles' ability to scatter and absorb solar radiation and act as seeds by which cloud droplets form (i.e., cloud condensation nuclei (CCN)). Since these particles are involved in such important atmospheric processes, various ground, airborne, and spaceborne instruments are

deployed to measure their optical and microphysical characteristics. As these instruments vary greatly in terms of design and each has its own error characteristics, it is important to verify that measurements from such diverse instrument platforms agree with one another (i.e., closure analysis) and ultimately the global climate models they are assimilated into. This study focuses on external closure, where airborne in-situ and remote sensing (i.e., lidar, polarimeter) measurements are compared with one another. This type of analysis is critical because it can i) validate the accuracy and uncertainty of satellite and airborne lidar and polarimetric products, ii) create improved a priori aerosol particle properties to better constrain satellite retrievals, and iii) improve process studies by establishing new applications for lidar and polarimetric remote sensing products such as deriving hygroscopicity (κ) (Petters and Kreidenweis, 2007). The two remote sensors highlighted in this study are NASA's Second Generation High Spectral Resolution Lidar (HSRL-2) and Research Scanning Polarimeter (RSP), which are advanced airborne remote sensors that provide vertically-resolved and column retrievals of aerosol optical and microphysical properties. Details on these instruments will be provided in Sect. 2.2.

There previously have been successful efforts to perform closure between airborne in-situ and HSRL-2/RSP aerosol particle data. For example, airborne HSRL-2 extinction and backscatter measurements and HSRL-2-retrieved aerosol effective radius were evaluated using collocated in-situ aerosol products (Müller et al., 2014; Sawamura et al., 2017; Pistone et al., 2019). Also, evaluations of RSP retrievals of aerosol optical and microphysical properties have been performed using AERONET retrievals (Wu et al., 2015; Fu et al., 2020). There have also been a limited number of case studies successfully making comparisons between RSP retrievals and airborne in-situ data from the ARCTAS (Knobelspiesse et al., 2011) and ORACLES field campaigns (Pistone et al., 2019). However, the fine- and coarse-mode aerosol microphysical properties from RSP have not been systematically evaluated against in-situ aerosol data to date.

One main difficulty of performing external closure is that in-situ instruments typically dry aerosol particles to a relative humidity RH of $\leq 40\%$ using silica gel or Nafion before measurement to simplify their analysis (Sorooshian et al., 2023). However, lidars and polarimeters retrieve particle properties without altering their RH (i.e., measurements at ambient conditions). Variations in RH significantly alter aerosol physical and optical characteristics, making dry and ambient data sets difficult to compare. The other major difficulty of closure analysis is that in-situ instruments cannot efficiently sample coarse-mode particles due to limitations in the inlet cutoff diameter (i.e., typical cutoff particle diameter (D) of $5 \mu\text{m}$) and transmission efficiency challenges in tubing leading to in situ instruments. In addition to the coarse-mode sampling limitations, the fine-mode particles can also be lost between the external inlet and the inlets of the instruments. There have been efforts to retrieve in-situ ambient aerosol properties to enable external closure studies (i.e., Sawamura et al. (2017)), but these studies tend to assume there is no significant coarse-mode contribution when calculating these properties and therefore limit their calculations to fine-mode aerosol particles only. Coarse-mode species such as dry sea salt and dust are difficult to consider because they tend to have D greater than $5 \mu\text{m}$ and are generally non-spherical. Also, dry sea salt is non-absorbing and can have large values of κ (Sorribas et al., 2015) while dust has a complex refractive index (CRI) that is dependent on wavelength (Voshchinnikov and Farafonov, 1993; Veselovskii et al., 2010; Wagner et al., 2012; Sorribas et al., 2015), further contributing to difficulties in in-situ instruments measuring these species.

To improve upon these previous efforts in retrieving ambient in-situ aerosol properties, we introduce the In Situ Aerosol Retrieval Algorithm (ISARA), a forward optical model based on the Modeled Optical Properties of Ensembles of Aerosol Particles (MOPSMAP) package (Gasteiger and Wiegner, 2018). This program retrieves ambient in-situ optical and microphysical properties of aerosol particles at any user-specified wavelength. The main advantage of ISARA is that it can consider the contribution of coarse-mode aerosol species when calculating ambient aerosol properties. This algorithm is applied to data collected during the NASA Aerosol Cloud meTeorology Interactions oVer the western ATlantic Experiment (ACTIVATE) field campaign, a mission dedicated to characterizing aerosol-cloud-meteorology interactions by using two spatially-synchronized aircraft to provide systematic and simultaneous airborne measurements (Sorooshian et al., 2019). The robustness and diversity of the ACTIVATE data set allows us to perform external closure between in-situ, lidar, and polarimetric measurements for a variety of aerosol particle species.

Section 2 provides a detailed discussion of the methods used to perform external closure in the following order: 1) ACTIVATE mission, 2) Cloud filtering of in-situ data, 3) ISARA methodology including retrieval descriptions for dry imaginary refractive index (IRI) and hygroscopicity (κ), 4) HSRL-2 and RSP data processing including cloud filtering of remote sensing data and matching HSRL-2 data to the RSP resolution, 5) collocation of in-situ data to the remote sensing data, and 6) statistical analysis to perform in-situ and remote sensing comparisons. Section 3 presents results of the statistical analysis performed on the remote sensing - in-situ comparisons for ACTIVATE's 2020 - 2022 data set followed by selected ACTIVATE case studies. Section 4 summarizes the key points of this study and suggests potential avenues for future work.

2 Methods

2.1 ACTIVATE Mission Description

The ACTIVATE dataset provides a rich dataset to investigate numerous atmospheric processes over the western North Atlantic Ocean, including aerosol-cloud interactions that represent the largest uncertainty in estimates of total anthropogenic radiative forcing (Field et al., 2014). ACTIVATE featured 162 coordinated science flights across six ACTIVATE deployments that occurred between 14 February 2020 and 18 June 2022. The six ACTIVATE deployments occurred between the following dates:

1. 14 February – 12 March 2020,
- 90 2. 13 August – 30 September 2020,
3. 27 January – 2 April 2021,
4. 13 May – 30 June 2021,
5. 30 November 2021 – 29 March 2022,
6. 3 May 2022 – 18 June 2022.

During the first five and a half ACTIVATE deployments, these joint flights were conducted out of the NASA Langley Research Center in Virginia. The final half of the sixth ACTIVATE deployment featured Bermuda as the base of operations. The ACTIVATE methodology and dataset are described in more detail in Sorooshian et al. (2023).

ACTIVATE follows a small number of previous studies that aim to study aerosol-cloud interactions in the dynamic western North Atlantic environment (Quinn et al., 2019; Sorooshian et al., 2020; Dadashazar et al., 2021a; Dadashazar et al., 2021b; Corral et al., 2021; Painemal et al., 2021). An important feature of the ACTIVATE data set is the extensive collocated advanced passive and active remote sensing and in-situ data, which have a flight duration of 3.3 hours. The ACTIVATE aircraft executed flights that can be broadly categorized into two mission types: “process studies” and “statistical surveys”. This study focuses on statistical survey flights, where the lower-flying HU-25 Falcon aircraft collected data at various vertical levels in and above the marine boundary layer (MBL) (Sorooshian et al., 2023). Simultaneously, the higher-flying King Air at approximately 9 km would conduct remote sensing and launch dropsondes while being spatially coordinated with the Falcon. These flights comprised 90% of missions and allowed for the efficient in-situ characterization of gas, cloud, aerosol and meteorological quantities of the MBL across multiple flights and deployments (Dadashazar et al., 2022; Sorooshian et al., 2023). The spatial coordination of the two aircraft during the statistical surveys is ideal for the type of validation that this study aims to accomplish.

2.2 Remote Sensing Instrument Descriptions

The HSRL-2 is an active lidar remote sensor that provides vertically-resolved profiles of various aerosol and cloud properties for campaigns such as The Cloud, Aerosol and Monsoon Processes Philippines Experiment (CAMP2Ex), Deriving Information on Surface Conditions from Column and VERTically Resolved Observations Relevant to Air Quality (DISCOVER-AQ), and ACTIVATE (Hair et al., 2008; Sawamura et al., 2017; Burton et al., 2016; Reid et al., 2023; Sorooshian et al., 2023). Unlike standard elastic backscatter lidars such as Cloud-Aerosol Lidar with Orthogonal Polarization (CALIOP), the HSRL-2 has the ability to measure aerosol backscatter and extinction separately (Hair et al., 2008; Burton et al., 2016; Burton et al., 2018). Therefore, HSRL-2 measurements of total ambient backscatter and extinction at 532 nm serve as the gold standard (Sawamura et al., 2017). The HSRL-2 products include ambient vertically-resolved lidar backscattering and extinction coefficients and ambient linear depolarization ratio (LDR) at wavelengths of 355, 532, and 1064 nm (Fernald, 1984; Hair et al., 2008; Burton et al., 2018). The HSRL-2 field of view is 1 mrad, which corresponds to a 9 m footprint for an aircraft at 9 km altitude.

In contrast, the RSP is a passive polarimetric remote sensor that uses highly accurate multispectral and hyperangular photopolarimetric measurements to characterize aerosol and cloud properties (Cairns et al., 1999; Cairns et al., 2003). The aerosol products are based on an optimal estimate using the Research Scanning Polarimeter Microphysical Aerosol Properties from Polarimetry (RSP-MAPP) algorithm (Stamnes et al., 2018). Fine- and coarse-mode aerosol optical and microphysical properties are retrieved using seven channels that measure the total and polarized radiance across the visible-shortwave spectrum (wavelength = 410 – 2250 nm) with over 100 viewing angles between $\pm 55^\circ$. The RSP has a field of view of 14 mrad, which results in a 126 m footprint for an aircraft at 9 km altitude. As a result, the RSP provides accurate column-averaged retrievals of aerosol microphysical and optical properties such as fine-mode aerosol effective radius ($r_{eff,f}$) and fine-mode and total single scattering albedo (SSA_f, SSA_t) at 555 nm. The

relevant King Air measurements are described in Table 1 along with their associated vertical resolutions, temporal resolutions, and uncertainties.

Table 1: Summary of King Air payload including High Spectral Resolution Lidar – generation 2 (HSRL-2) and Research Scanning Polarimeter (RSP) measurements with associated resolutions and uncertainties.

Instrument	Parameter Description	Vertical/Temporal Resolution	Uncertainty
High Spectral Resolution Lidar -generation 2 (HSRL-2)	Total ambient aerosol particle extinction coefficient at 355, 532, and 1064 nm	175 m/10 s	-
	Total ambient extinction coefficient at 355, 532, and 1064 nm	175 m/10 s	-
	Total ambient linear depolarization ratio (LDR) at 355, 532, and 1064 nm	175 m/10 s	20%
Research Scanning Polarimeter (RSP)	Column-averaged total and fine-mode aerosol effective radius (r_{eff})	-/4.167 s	0.02 and 0.15 μm
	Column-averaged total and fine-mode single scattering albedo at 555 nm (SSA_t, SSA_f)	-/4.167 s	0.04 and 0.02

2.3 In-Situ Instrument Descriptions

The in-situ N_a measurements are taken from the Scanning Mobility Particle Sizer (SMPS) (Model 3085 DMA, Model 3776 CPC, and Model 3088 Neutralizer; TSI, Inc.) and Laser Aerosol Spectrometer (LAS) (Model 3340, TSI, Inc.) (Sorooshian et al., 2023). The SMPS measures concentrations of particles with dry particle diameter (D) ranging in sizes from 2.97 to 94 nm at a 45 Hz temporal resolution. The LAS measures concentrations of particles with dry D ranging in sizes from 94 to 7500 nm at a 1 Hz temporal resolution. The LAS sampled particles that were actively dried with a 6" Perma Pure Monotube Dryer 700 for all but 30 flights. The 30 flights between May 14 and June 30 2021 used ram heating to passively dry the particles before measurement. The N_a measurements provided by the LAS and SMPS are provided at standard temperature and pressure (273.15 K and 1013 mb). While the LAS has a measurement range up to 7500 nm, the maximum cutoff D of the sample inlet prevents the measurement of particles with ambient D greater than 5000 nm (Mcnaughton et al., 2007; Chen et al., 2011). To account for potential hygroscopic effects, we only include particles with dry optical D up to 3488 nm in this analysis. It is noted that the LAS particle sizing is

calibrated using an assumed dry CRI and shape. The systematic error introduced by assuming dry *CRI* and particle shape is minimized by performing the LAS calibration with respect to spherical ammonium sulfate particles with dry CRI of $1.53+0 \times i$, which is among the most common aerosol species (Ebert et al., 2004; Sawamura et al., 2017). The SMPS asymmetry factor is normalized such that the highest channel of the SMPS and the lowest channel of the LAS have similar number concentrations.

The in-situ optical measurements are taken by the nephelometer (Model 3563, TSI) and the tricolor Particle Soot Absorption Photometer (PSAP) (Radiance Research) (Sorooshian et al., 2023). The nephelometer measures dry particle scattering coefficients at 450, 550, and 700 nm at a 1 Hz temporal resolution while the PSAP measures dry absorption coefficients at 470, 532, and 660 nm at a 1 Hz temporal resolution. Note that the scattering measurements were made using two nephelometers in parallel, one dry ($< 40\%$ RH) and one wet ($\sim 85\%$ RH). This parallel deployment allows for scattering coefficients to be adjusted to any RH up to saturation (99%) through the computation of the hygroscopic growth function ($f(RH)$).

Measurements of ambient liquid water content (*LWC*) and cloud drop number concentration (N_d) are used to classify in-situ data as cloud-free, ambiguous, or cloud. This classification becomes important because ISARA retrievals are performed for cloud-free cases. Ambient *LWC* and N_d are both derived from ambient particle size distribution measured by a Cloud Droplet Probe (CDP) (Droplet Measurement Technologies) (Sinclair et al., 2019). The CDP can measure particles in the ambient *D* size range of 2000 – 50000 nm. Note that the N_d derived by the CDP is noted by N_{CDP} throughout this paper. In this study, measurements where *LWC* is between 0.001 and 0.02 g m⁻³ and N_d is between 5 and 50 cm⁻³ are classified as ambiguous (i.e., not entirely cloud-free). Therefore, measurements are considered cloud-free where *LWC* and N_d are less than 0.001 g m⁻³ and 5 cm⁻³, respectively. The ambient aerosol particle size distribution measured by the CDP also helps account for coarse aerosol particles when calculating the final properties of the ambient aerosol particles (see Sect. 2.4). *RH* measured from the Diode Laser Hygrometer (DLH) is also used to derive ambient aerosol properties (Diskin et al., 2002). The relevant Falcon measurements are described in Table 2 along with their associated size ranges, temporal resolutions, and uncertainties.

Table 2: Summary of relevant Falcon payload instruments with associated size ranges, time resolutions, and uncertainties.

Instrument	Parameter Description	Size Range (nm)	Native Time Resolution (s)	Systematic Uncertainty	Random Uncertainty
Scanning Mobility Particle Sizer (SMPS) (Model 3085 DMA, Model 3776 CPC, and Model 3088 Neutralizer; TSI, Inc.)	Dry size-resolved particle number concentration (n_o)	2.94 – 94.0	45	20%	-
Laser Aerosol Spectrometer (LAS) (Model 3340, TSI, Inc.)	Dry size-resolved particle number concentration (n_o)	93.9 - 3162	1	20%	-
Nephelometer (Model 3563, TSI, Inc.)	Dry scattering coefficients at 450, 550, and 700 nm	< 5000	1	20%	2 Mm ⁻¹
Tricolor Particle Soot Absorption Photometer (PSAP) (Radiance Research)	Dry absorption coefficients at 470, 532, and 660 nm	< 5000	1	15%	-
Cloud Droplet Probe (CDP) (Droplet Measurement Technologies)	Liquid water content (LWC), cloud drop number concentration (N_d), coarse-mode ambient n_o	2000 - 50000	1	20%	-

2.4 In Situ Aerosol Retrieval Algorithm (ISARA) Description

The first step of this algorithm is to match all in-situ data to the lowest time resolution among the suite of instruments. In the case of ACTIVATE, the SMPS has the lowest time resolution (45 s). The data merge is handled by the NASA Airborne Science Data for Atmospheric Composition online merge tool (www-air.larc.nasa.gov). Computation of scattering and absorption coefficients (C_{scat} , C_{abs}) is accomplished using MOPSMAP (Bohren and Huffman, 2008; Gasteiger and Wiegner, 2018). MOPSMAP relies on Mie theory to perform these calculations, which assumes that the aerosol particle is a homogeneous dielectric sphere with a complex refractive index (CRI). An aerosol particle's CRI is a complex number that is defined as follows:

$$CRI = RRI + IRI \times i \quad (1)$$

where RRI and IRI are the real and imaginary components of CRI , respectively. MOPSMAP first calculates spectral scattering and absorption efficiencies (Q_{scat}, Q_{abs}) using information such as CRI and then multiplies them by an aerosol particle size distribution inputted by the user to calculate C_{scat} and C_{abs} (Eq. 2).

$$C_{scat,abs}(\lambda) = \int_{d \log D} \left[\frac{\pi D^2}{4} \cdot Q_{scat,abs}(\lambda, CRI, D) \cdot n(D) \right] d \log D. \quad (2)$$

where D is particle diameter, λ is the wavelength of the measurement source, and $n(D)d \log D$ is the logarithmic particle size distribution. Although MOPSMAP is a robust package for calculating optical coefficients, its optical properties do not account for hygroscopicity and therefore cannot calculate these properties in ambient, introducing the need for ISARA. The first main step of the ISARA retrieval is calculating a total dry CRI since this is a critical parameter for Q and C as mentioned previously. Since RRI is set as a constant (1.55), this step focuses on retrieving IRI . Eq. 2 is rewritten as follows to denote the calculation of dry parameters (Eq. 3):

$$C_{scat,abs,dry}(\lambda) = \int_{d \log D_{dry}} \left[\frac{\pi D_{dry}^2}{4} \cdot Q_{scat,abs}(\lambda, CRI_{dry}, D_{dry}) \cdot n_o(D_{dry}) \right] d \log D_{dry}. \quad (3)$$

To provide the dry size distribution, the user inputs stitched LAS and SMPS size distribution data to represent the full range of aerosol particle sizes measured in ACTIVATE. Then, $C_{scat,dry}$ and $C_{abs,dry}$ are calculated by iterating through dry IRI from 0.0001 to 0.08 in increments of 0.001, values representative of typical aerosol particles in the ACTIVATE region. After C_{scat} and C_{abs} are calculated, ISARA retrieves a final value of total dry IRI (\overline{IRI}) by taking the average of all IRI values where the corresponding computed C_{scat} is within 20% and C_{abs} is within 1 Mm^{-1} of measured C_{scat} and C_{abs} , respectively ($\Delta C_{scat} < 20\%$ and $\Delta C_{abs} < 1 \text{ Mm}^{-1}$) (adapted from Sawamura et al. (2017)). A summary of this retrieval step is provided below (Fig. 1).

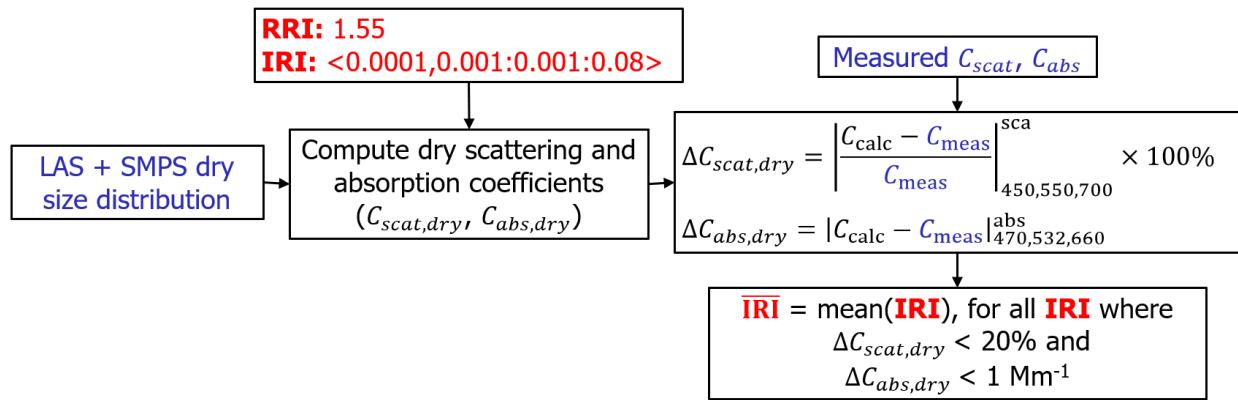


Figure 1: Flow chart of the dry imaginary refractive index (IRI) retrieval procedure. Blue text represents measured values, black text represents MOPSMAP-calculated values, and red text represents when ISARA makes retrieval. C_{calc} refers to calculated $C_{scat,dry}$ and $C_{abs,dry}$ while C_{meas} refers to $C_{scat,dry}$ and $C_{abs,dry}$ from the nephelometer and PSAP instruments.

Now that total dry *IRI* has been calculated, it is then necessary to retrieve the hygroscopicity parameter κ . Since the retrieval of κ relies on the same Mie theory principles as the previous step, Eq. 3 is rewritten to represent wet (i.e., humidified) parameters (Eq. 4).

$$C_{scat,wet}(\lambda) = \int_{d\log D_{wet}} \left[\frac{\pi D_{wet}^2}{4} \cdot Q_{scat}(\lambda, CRI(g), D_{wet}) \cdot n_o(D_{wet}) \right] d\log D_{wet}. \quad (4)$$

For spherical particles, both *CRI* and *D* are related to κ by the hygroscopic growth factor (*g*), which is defined as the ratio between humidified *D* (D_{wet}) and dry *D* (D_{dry}) (Eq. 3).

$$g = \frac{\text{Humidified Diameter}}{\text{Dry Diameter}} = \frac{D_{wet}}{D_{dry}}. \quad (5)$$

g is related to κ by RH via the following parameterization from Petters and Kreidenweis (2007):

$$\frac{RH}{\exp\left(\frac{A}{D_{dry}g}\right)} = \frac{g^3 - 1}{g^3 - (1 - \kappa)}, \quad (6)$$

where *A* is the water activity of the aerosol particle. Water activity is a temperature-dependent function defined as follows:

$$A = \frac{4\sigma_w M_w}{RT\rho_w}, \quad (7)$$

where σ_w , M_w , *R*, *T*, and ρ_w are surface tension of water, molecular weight of water, ideal gas constant, temperature, and the density of water, respectively. The values of σ_w , ρ_w , and *T* are assumed to be 0.072 J m⁻², 1000 kg m⁻³, and 298.15 K, respectively (Petters and Kreidenweis, 2007). For particles larger than 90 nm, this equation becomes (Zieger et al., 2013):

$$\left(\frac{D_{wet}}{D_{dry}}\right)^3 = g^3 = 1 + \kappa * \frac{RH}{100 - RH}. \quad (8)$$

Eq. 8 allows for the dry size distribution from the LAS and SMPS to be converted into an ambient size distribution (0 – 99% RH) using RH measurements from the DLH as introduced in Sect. 2.3. Visually, hygroscopic growth results in the size distribution being shifted to the right by *GF* if the size distribution is graphed with diameter on the x-axis. However, the size distribution width and effective variance remain unchanged. To account for the impact that water has on CRI_{dry} , CRI_{wet} is assumed to be the volume-weighted average between CRI_{dry} and the *CRI* of water (CRI_{H_2O}). The volume-weighted mixing model is used because it is found to be the most robust of a variety of possible mixing models by Nessler et al. (2005). The volume-weighted average of humidified *CRI* is defined as:

$$CRI_{wet} = CRI_{dry} \cdot \frac{V_{dry}}{V} + CRI_{H_2O} \cdot \frac{V_{H_2O}}{V}, \quad (9)$$

where V is humidified particle volume and CRI_{H_2O} equals $1.33 + 0 \cdot i$ (Hale and Query, 1973). For spherical aerosol particles, the dry volume (V_{dry}) is equal to $\frac{1}{6}\pi D_{dry}^3$ and V is equal to $\frac{1}{6}\pi D^3$. The difference between V and V_{dry} is the volume of water (V_{H_2O}) that has accumulated around the particle due to humidification (i.e., $V_{H_2O} = V - V_{dry}$). The following expression (Eq. 10) is used to compute CRI as a function of g (and consequently κ from Eq. 8) and accounts for fine-mode particles that have restructured during the humidification process prior to the nephelometer measurement of the humidified C_{scat} :

$$CRI(g) \approx \frac{g^3 \cdot CRI_{dry} + CRI_{H_2O} \cdot (g^3 - 1)}{g^3} \quad (10)$$

Note that Eq. 10 is used for instances where $f(RH) \geq 1$. If $f(RH) < 1$, ISARA uses CRI_{dry} calculated in the previous step (Fig. 1). Then, $C_{scat,wet}$ is calculated by iterating through κ from 0.01 to 1.40 in increments of 0.01, also a range typical of ACTIVATE's measured aerosol particles. After $C_{scat,wet}$ is calculated, it is also necessary to obtain measured $C_{scat,wet}$ from the nephelometer to compute $\Delta C_{scat,wet}$ and take the average of all κ (similar to the last step of Fig. 1). However, this measurement cannot be taken directly from the nephelometer since ACTIVATE only has measurements of dry C_{scat} and $f(RH)$, which is defined as the ratio between $C_{scat,wet}$ ($RH \cong 80\%$) and $C_{scat,dry}$ ($RH \cong 20\%$). To obtain measured $C_{scat,wet}$, $C_{scat,dry}$ from the dry nephelometer is multiplied by $f(RH)$ derived from the tandem nephelometers as detailed in Sect. 2.3. After this step is performed, the smallest κ values are taken for computed $C_{scat,wet}$ within 1% of measured $C_{scat,wet}$ ($\Delta C_{scat,wet} < 1\%$). All of these κ values are then averaged to yield a final retrieval for total κ ($\bar{\kappa}$). A summary of this retrieval process is summarized below (Fig. 2).

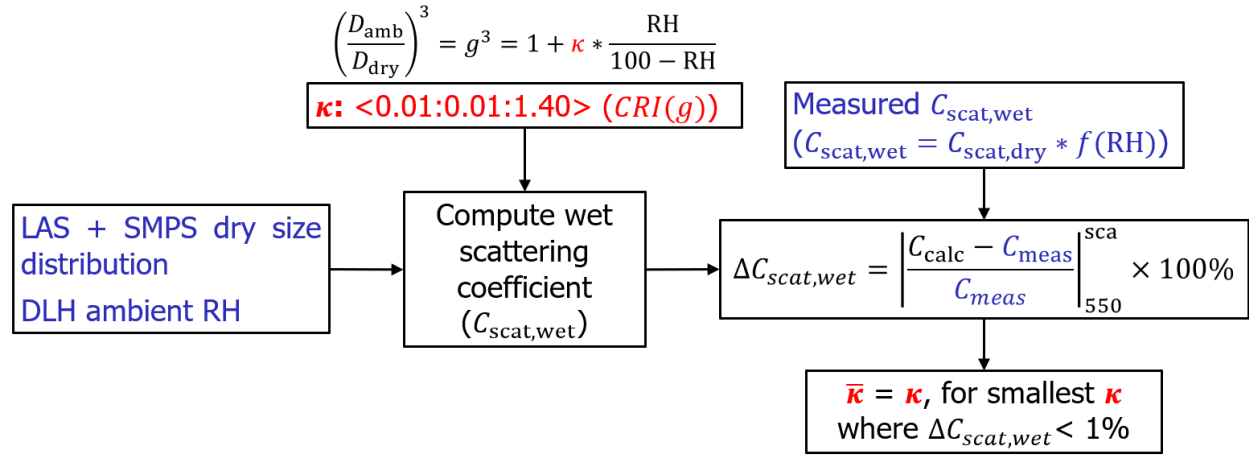


Figure 2: Flow chart of hygroscopicity parameter (κ) retrieval procedure. Blue text represents measured values, black text represents MOPSMAP-calculated values, and red text represents when ISARA makes retrieval. C_{calc} refers to calculated $C_{scat,wet}$ while C_{meas} refers to $C_{scat,wet}$ from tandem nephelometers ($f(RH)$ calculation).

Now that total IRI and κ have been calculated, ISARA inputs these parameters into the Mie theory relation (Eq. 2) to calculate ambient scattering and absorption coefficients ($C_{scat,amb}$, $C_{abs,amb}$) (Eq. 11).

$$C_{scat,abs,amb}(\lambda) = \int_{d\log D_{amb}} \left[\frac{\pi D_{amb}^2}{4} \cdot Q_{scat,abs}(\lambda, CRI, \kappa, D_{amb}) \cdot n_o(D_{amb}) \right] d\log D_{amb}. \quad (11)$$

With final calculations of $C_{scat,amb}$ and $C_{abs,amb}$, ISARA can now retrieve secondary aerosol optical properties such as extinction (ϵ) and single-scattering albedo (SSA) and microphysical properties such as number concentration (N_a) and effective radius (r_{eff}). Note that this retrieval process is relevant for aerosol particles with $D < 5 \mu\text{m}$. For coarse-mode ($D > 5 \mu\text{m}$) particles, ISARA makes retrievals using size distribution data from the CDP and assuming the CRI of water (CRI_{H_2O}) instead.

2.5 Collocation Process and Statistical Validation

The platform collocation process for this work is explained in complete detail in Schlosser et al. (2024), but is summarized in this section. Additionally, this section provides a summary of the methods used to obtain columnar average values for in-situ data for comparison with the RSP data, which is described in detail in Schlosser et al. (2022).

The ISARA-derived ambient extinction data were matched to the native HSRL-2 resolution of 10 s by implementing the collocation data files produced as part of Schlosser et al. (2024). Additional spatiotemporal constraints of 15 km and 6 min were also applied. The in-situ data are then binned and averaged to the HSRL-2 altitude grid. The ambient N_a data are averaged in a similar fashion; however, these data are matched with valid RSP and HSRL-2 profiles. The in-situ data are weighted by extinction when averaged.

In order to validate the RSP parameters of total N_a and SSA as well as fine-mode r_{eff} , the ISARA-derived products are grouped to both vertical profiles and level legs where the Falcon aircraft was flying at a single altitude for more than three minutes. Once grouped, the data are weighted by extinction and averaged.

To quantify the agreement between remotely-sensed and ISARA-derived in-situ measurements of aerosol properties, correlation coefficient (r), mean relative bias (MRB), range-normalized mean absolute deviation ($NMAD$), and range-normalized root-mean-square deviation ($NRMSD$) are used. Each of these metrics is written as follows:

$$r = \frac{\sum_{j=1}^{n_p} [(X(j) - \bar{X}) * (Y(j) - \bar{Y})]}{\sqrt{\sum_{j=1}^{n_p} [X(j) - \bar{X}]^2 * \sum_{j=1}^{n_p} [Y(j) - \bar{Y}]^2}}, \quad (12)$$

$$MRB = \frac{Y(j) - X(j)}{Y(j) + X(j)} * 2 * 100\%, \quad (13)$$

$$NMAD = \frac{100\%}{\max(X) - \min(X)} * \frac{\sum_{j=1}^{n_p} |Y(j) - X(j)|}{n_p}, \quad (14)$$

$$NRMSD = \frac{100\%}{\max(X) - \min(X)} * \sqrt{\frac{\sum_{j=1}^{n_p} |Y(j) - X(j)|^2}{n_p}}, \quad (15)$$

where $X(j)$ and $Y(j)$ are the set of in-situ and remote sensing aerosol measurements, respectively, n_p is the total number of points for each data set, and \bar{X} and \bar{Y} are the mean of $X(j)$ and $Y(j)$, respectively. The mean error (mean \pm

standard deviation) of each instrument platform retrieval is also used to determine the degree of closure success for a particular aerosol property.

When performing the closure analysis, ISARA in-situ retrievals and HSRL-2 measurements are successful for a given ambient aerosol property if *NMAD* is less than 15%, *MRB* is less than 30%, and *r* is greater than 0.5. Closure between ISARA in-situ measurements and RSP retrievals is considered successful for a given ambient aerosol property if the mean values are within the RSP uncertainty values for that property listed in Table 1. If the results are close to these metrics, they are considered “partially successful”, and otherwise they are considered unsuccessful.

3 Results and Discussion

After performing the procedures detailed in Sect. 2, ISARA-derived in-situ measurements of aerosol properties can be compared to coincident HSRL-2 and RSP retrievals in the ACTIVATE data set. First, HSRL-2 and in-situ measurements of total ambient aerosol extinction at 532 nm (ϵ_{532nm}) are compared (Fig. 3).

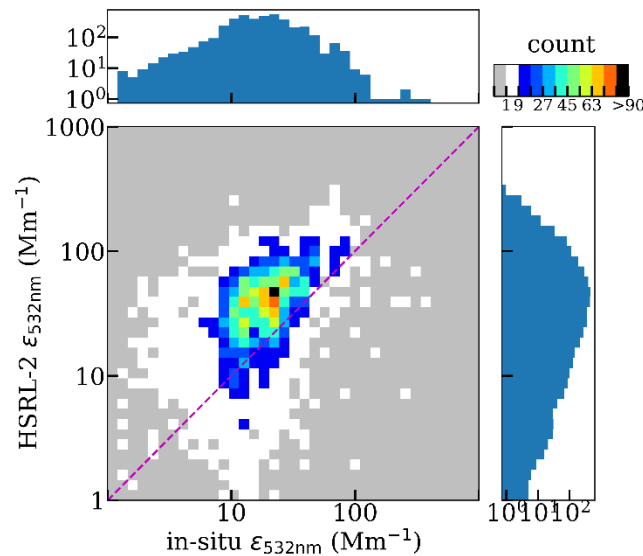


Figure 3: Scatterplot of 3983 data points comparing HSRL-2-retrieved values versus ISARA-derived in-situ values for total ambient aerosol extinction at 532 nm (ϵ_{532nm}) for 2020 – 2022 ACTIVATE data. Also shown on the perimeter of the scatterplot are histograms to show the distribution of each variable. The goodness of fit statistics are: $r = 0.47$, $MRB = 54\%$, $NMAD = 7\%$, and $NRMSD = 10\%$.

HSRL-2 and in-situ measurements of ϵ_{532nm} are moderately correlated with an r of 0.47 (Fig. 3). The MRB value of 54% shows that the HSRL-2 data is biased quite high relative to in-situ data, showing that the HSRL-2 retrieves higher values of ϵ_{532nm} than the in-situ instruments throughout the ACTIVATE campaign. This result is also seen in Sawamura et al. (2017), even though ISARA considers coarse-mode aerosol in its calculations whereas the algorithm in Sawamura et al. (2017) only considers fine-mode aerosol. This discrepancy with the remote sensors is likely due to particle losses innate to in-situ sampling as previously mentioned. Although in-situ values are lower than those from the HSRL-2, strong agreement and low variability are evident from the $NMAD$ of 7% and $NRMSD$ of 10%,

respectively. Therefore, these results indicate that the HSRL-2 and in-situ ε_{532nm} data are closed with partial success. Next, we compare jointly-retrieved HSRL-2 – RSP and in-situ aerosol number concentration (N_a) (Fig. 4).

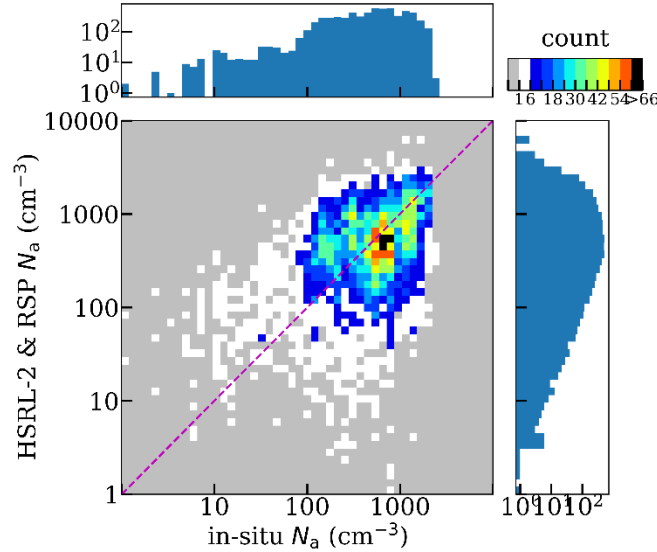


Figure 4: Scatterplots of 6257 data points of jointly-retrieved HSRL-2 - RSP-retrieved values versus ISARA-derived in-situ values for aerosol particle number concentration (N_a) from 2020 – 2022 ACTIVATE data along with histograms to show the distribution of each variable. The goodness of fit statistics are: $r = 0.38$, $MRB = -4\%$, $NMAD = 7\%$, and $NRMSD = 9\%$.

These comparisons show a r of 0.38, MRB of -4%, $NMAD$ of 7%, and $NRMSD$ of 9% (Fig. 4). These results have a much lower bias than shown in the ε_{532nm} comparisons, but show that the HSRL-2 + RSP product slightly underestimates in-situ N_a . Other than this lower bias, agreement in terms of $NMAD$ and variability in terms of $NRMSD$ is comparable to the ε_{532nm} results. Overall, the N_a comparisons are closed relatively successfully when compared to results of Schlosser et al. (2022)’s evaluation of HSRL-2 + RSP N_a using N_a measured by the LAS (N_{LAS}). Comparisons with ISARA-derived N_a have stronger performance in terms of $NMAD$ and $NRMSD$ than both vertically-resolved and column-averaged N_{LAS} (Schlosser et al. (2022)’s best results are $NMAD$ of 16% and $NRMSD$ of 24%). However, correlation for ISARA N_a comparisons is weaker compared to vertically-resolved N_{LAS} ones (best is 0.76 in Schlosser et al. (2022)) but comparable to the column-averaged N_{LAS} results (best is 0.36 in Schlosser et al. (2022)). Overall, these comparisons are deemed to be successfully closed. Now, comparisons of in-situ measurements with RSP retrievals are presented. First, the results of fine-mode aerosol effective radius ($r_{eff,f}$) comparisons are discussed (Fig. 5).

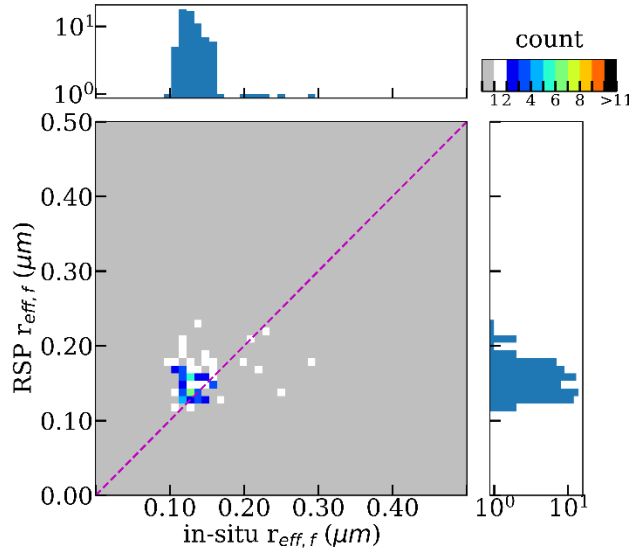


Figure 5: Scatterplots of 72 data points of RSP-retrieved values versus ISARA-derived in-situ values for fine-mode aerosol effective radius ($r_{eff,f}$) from 2020 – 2022 ACTIVATE data along with histograms to show the distribution of each variable. The goodness of fit statistics are: $r = 0.25$, $MRB = 12\%$, $NMAD = 15\%$, and $NRMSD = 21\%$. The mean error of the in-situ measurements is $0.14 \mu\text{m} \pm 0.03 \mu\text{m}$ and the mean error of the RSP retrievals is $0.15 \mu\text{m} \pm 0.02 \mu\text{m}$.

Based on the r of 0.25, MRB of 12%, $NMAD$ of 15%, and $NRMSD$ of 21%, comparisons of $r_{eff,f}$ are partially successful. It is also seen that the mean error between ISARA in-situ measurements and RSP retrievals is nearly identical. However, these results demonstrate lower bias than what is seen in the DISCOVER-AQ California results in Sawamura et al. (2017) (MRB of 12% versus -25%) and higher correlation than in the DISCOVER-AQ Texas results (r of 0.25 versus -0.05), though the author shows better correlation (r of 0.53 vs. 0.25) for DISCOVER-AQ California and slightly lower bias (MRB of 7% versus 12%). Note that the results of this study and Sawamura et al. (2017) are not necessarily one-to-one because Sawamura et al. (2017) uses HSRL-2 r_{eff} rather than RSP, but this work provides a preliminary basis of comparison for in-situ and remote sensing r_{eff} closure. Although the goodness of fit statistics in Fig. 5 indicate partial success, closure of $r_{eff,f}$ is considered successful because the in-situ mean error value ($0.14 \mu\text{m} \pm 0.03 \mu\text{m}$) is within the RSP uncertainty of $0.15 \mu\text{m}$. Lastly, comparisons of ISARA-derived in-situ measurements and RSP retrievals of fine-mode single scattering albedo (SSA_f) and total single scattering albedo (SSA_t) at 555 nm are presented (Fig. 6).

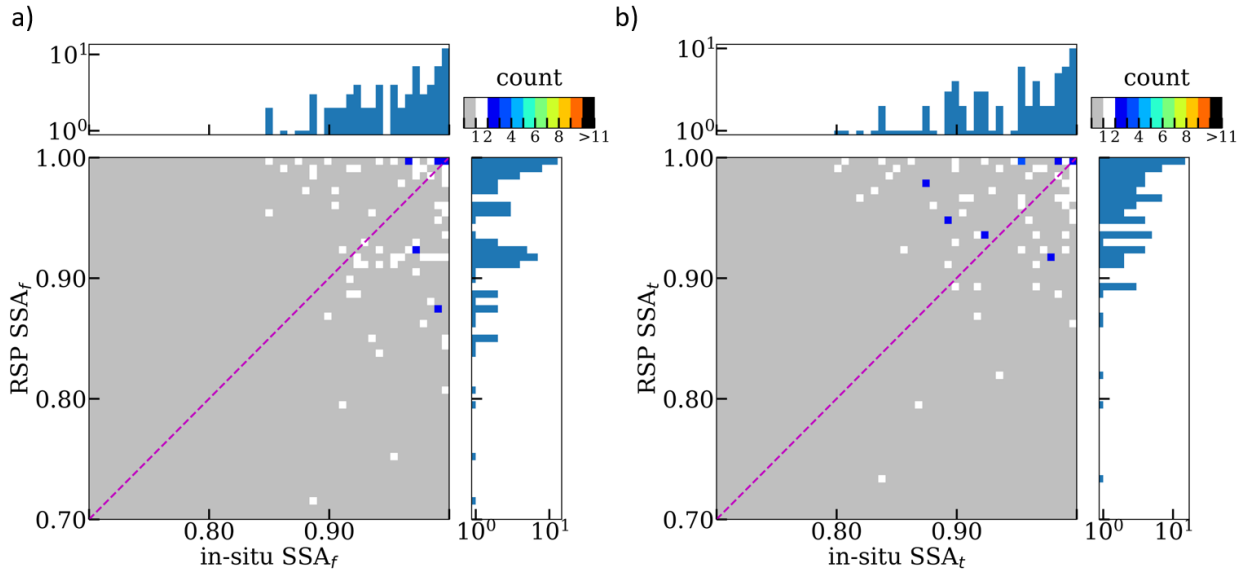


Figure 6: Scatterplots of 72 data points of RSP-retrieved values versus ISARA-derived in-situ values for a) fine-mode single scattering albedo (SSA_f) and b) total single scattering albedo (SSA_t) at 555 nm from 2020 – 2022 ACTIVATE data along with histograms to show the distribution of each variable. The goodness of fit statistics for panel a) are: $r = -0.09$, $MRB = 0\%$, $NMAD = 10\%$, and $NRMSD = 16\%$. The mean error of the in-situ measurements is 0.94 ± 0.08 and the mean error of the RSP is 0.94 ± 0.06 . The goodness of fit statistics for panel b) are: $r = -0.03$, $MRB = 0\%$, $NMAD = 1\%$, and $NRMSD = 15\%$. The mean error of the in-situ measurements is 0.93 ± 0.10 and the mean error of the RSP is 0.95 ± 0.05 .

Both SSA_f and SSA_t are not successful in terms of correlation ($r = -0.09, -0.03$), but are successful in terms of MRB (0%) and NMAD (10%). Success is also seen by ISARA and the RSP retrieving identical mean values for SSA_f (0.94) and near identical mean values for SSA_t (0.93 and 0.95). It is also important to note that ISARA in-situ retrievals appear to significantly improve the closure of fine-mode SSA against RSP in terms of the mean and standard deviation compared to in-situ aerosol products that use only $f(RH)$ to derive SSA (Fig. 7).

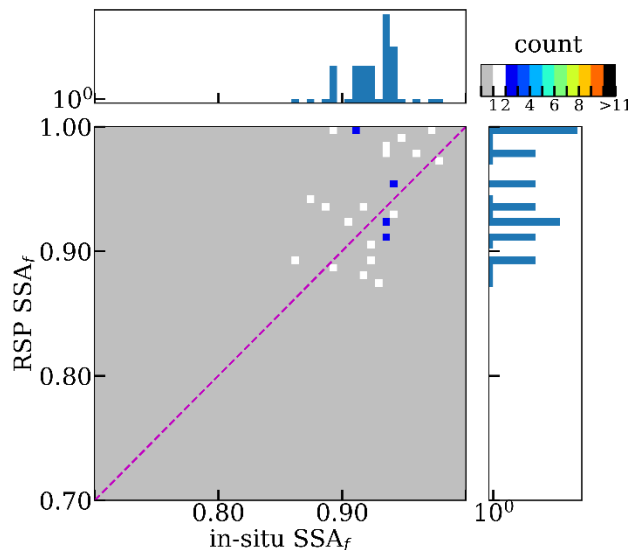


Figure 7: Scatterplots of 42 data points of RSP-retrieved versus measured in-situ values for fine-mode single scattering albedo (SSA_f) at 555 nm from 2020 – 2022 ACTIVATE data along with histograms to show the distribution of each variable.

The goodness of fit statistics are: $r = -0.15$, $MRB = 2\%$, $NMAD = 29\%$, and $NRMSD = 35\%$. The mean error of the in-situ measurements is 0.92 ± 0.04 and the mean error of the RSP is 0.94 ± 0.05 .

Fig. 6 shows slightly improved r (by 0.06) with MRB going to 0% and $NMAD$ improving by 19%, while $NRMSD$ improved by 19% for SSA_f . Mean retrieval errors also match more closely between in-situ measurements and RSP retrievals in Fig. 6 than in Fig. 7 (0.94 ± 0.08 vs. 0.92 ± 0.04). Overall, closure of SSA_f and SSA_t is considered successful since they are within the 0.02 and 0.04 RSP uncertainty values listed in Table 1.

4 Conclusions

This study introduces the In Situ Aerosol Retrieval Algorithm (ISARA) to enable external closure between in-situ and HSRL-2 and RSP remote sensing aerosol data from the NASA ACTIVATE field campaign. This algorithm adjusts dry in-situ aerosol measurements to ambient conditions (humidified) for both fine- and coarse-mode species. Closure analysis is performed on the following four ambient aerosol properties: total ambient aerosol extinction at 532 nm (ϵ_{532nm}), aerosol particle number concentration (N_a), fine-mode aerosol effective radius ($r_{eff,f}$), and fine-mode and total single scattering albedo at 555 nm (SSA_f, SSA_t). Comparisons of (ϵ_{532nm}) between HSRL-2 and ISARA-derived in-situ data show an $r = 0.47$, $MRB = 54\%$, $NMAD = 7\%$, and $NRMSD = 10\%$, which indicate partially successful closure. Results of closure between jointly-retrieved HSRL-2 and RSP N_a and ISARA-derived in-situ measurements yield an $r = 0.38$, $MRB = -4\%$, $NMAD = 7\%$, and $NRMSD = 9\%$. These results are considered to be closed with relatively high fidelity, especially when compared with findings in Schlosser et al. (2022). Comparisons of RSP $r_{eff,f}$, SSA_f , and SSA_t all demonstrate successful closure because the mean error of the in-situ measurements ($0.14 \mu\text{m} \pm 0.03 \mu\text{m}$, 0.94 ± 0.08 , and 0.94 ± 0.06 , respectively) is identical/nearly identical to that of the RSP retrievals ($0.15 \mu\text{m} \pm 0.02 \mu\text{m}$, 0.94 ± 0.06 , and 0.95 ± 0.05 , respectively) and fit within the RSP uncertainty estimates presented in Table 1 ($0.15 \mu\text{m}$, 0.02, and 0.04, respectively). However, the goodness of fit statistics, especially correlation coefficient (0.25, -0.09, -0.03, respectively), perform more weakly compared to ϵ_{532nm} and N_a results (0.47 and 0.38, respectively). Overall, this paper demonstrates that estimating the contribution of coarse-mode aerosol species allows for at least partial successful external closure of total ambient aerosol properties in the ACTIVATE region. Also, successful closure between in-situ and RSP ambient aerosol data is demonstrated for the first time in the literature.

Additional work is warranted to investigate how to improve goodness of fit statistics and increase the number of retrievals for $r_{eff,f}$, SSA_f , and SSA_t . Also, coarse-mode retrieval capabilities are hoped to be implemented into ISARA so that coarse-mode species can be examined and closed separately. For example, coarse-mode retrievals would allow for properties such as coarse-mode aerosol effective radius $r_{eff,c}$ to be calculated. It is ultimately hoped that ISARA will be used in many other field campaigns to advance airborne measurements of aerosol properties.

Code Availability

The ISARA codebase can be found at https://github.com/sdmitrovic/ISARA_code. A dedicated website for ISARA has been created, where instructions on how to download and use this code are found. The website is located at https://sdmitrovic.github.io/ISARA_code/ and updates are continuously being made.

Data Availability

ACTIVATE airborne data are available through <https://asdc.larc.nasa.gov/project/ACTIVATE>.

Author Contribution

SD and JS prepared manuscript with all co-authors involved in review and editing. JS, SD, and SS performed all closure analyses detailed in this study. All other authors provided input for the manuscript and/or participated in data collection and processing.

Competing Interests

The authors declare that they have no conflict of interest.

Disclaimer

Publisher's note: Copernicus Publications remains neutral with regard to jurisdictional claims in published maps and institutional affiliations.

Acknowledgements

Funding for this research was provided by the NASA ACTIVATE mission, a NASA Earth Venture Suborbital-3 (EVS-3) investigation funded by NASA's Earth Science Division and managed through the Earth System Science Pathfinder Program Office. A.S. was partially supported by ONR grant N00014-22-1-2733. J.S.S. was supported by the NASA Postdoctoral Program at NASA Langley Research Center, administered by Oak Ridge Associated Universities under contract with NASA. We wish to thank the pilots and aircraft maintenance personnel of NASA Langley Research Services Directorate for their work in conducting the ACTIVATE flights.

References

- Bohren, C. F. and Huffman, D. R.: Absorption and Scattering of Light by Small Particles, Wiley2008.
- Burton, S. P., Chemyakin, E., Liu, X., Knobelspiesse, K., Stamnes, S., Sawamura, P., Moore, R. H., Hostetler, C. A., and Ferrare, R. A.: Information content and sensitivity of the $3\beta + 2\alpha$ lidar measurement system for aerosol microphysical retrievals, *Atmos. Meas. Tech.*, 9, 5555-5574, 10.5194/amt-9-5555-2016, 2016.
- Burton, S. P., Hostetler, C. A., Cook, A. L., Hair, J. W., Seaman, S. T., Scola, S., Harper, D. B., Smith, J. A., Fenn, M. A., Ferrare, R. A., Saide, P. E., Chemyakin, E. V., and Müller, D.: Calibration of a high spectral resolution lidar using a Michelson interferometer, with data examples from ORACLES, *Appl. Opt.*, 57, 6061-6075, 10.1364/AO.57.006061, 2018.
- Cairns, B., Russell, E., and Travis, L.: Research Scanning Polarimeter: calibration and ground-based measurements, SPIE's International Symposium on Optical Science, Engineering, and Instrumentation, SPIE1999.

Cairns, B., Russell, E., LaVeigne, J., and Tennant, P.: Research scanning polarimeter and airborne usage for remote sensing of aerosols, *Optical Science and Technology, SPIE's 48th Annual Meeting, SPIE2003*.

Chen, G., Ziemba, L. D., Chu, D. A., Thornhill, K. L., Schuster, G. L., Winstead, E. L., Diskin, G. S., Ferrare, R. A., Burton, S. P., Ismail, S., Kooi, S. A., Omar, A. H., Slusher, D. L., Kleb, M. M., Reid, J. S., Twohy, C. H., Zhang, H., and Anderson, B. E.: Observations of Saharan dust microphysical and optical properties from the Eastern Atlantic during NAMMA airborne field campaign, *Atmos. Chem. Phys.*, 11, 723-740, 10.5194/acp-11-723-2011, 2011.

Corral, A. F., Braun, R. A., Cairns, B., Gorooh, V. A., Liu, H., Ma, L., Mardi, A. H., Painemal, D., Stamnes, S., van Diedenhoven, B., Wang, H., Yang, Y., Zhang, B., and Sorooshian, A.: An Overview of Atmospheric Features Over the Western North Atlantic Ocean and North American East Coast – Part 1: Analysis of Aerosols, Gases, and Wet Deposition Chemistry, *Journal of Geophysical Research: Atmospheres*, 126, e2020JD032592, <https://doi.org/10.1029/2020JD032592>, 2021.

Dadashazar, H., Alipanah, M., Hilario, M. R. A., Crosbie, E., Kirschler, S., Liu, H., Moore, R. H., Peters, A. J., Scarino, A. J., Shook, M., Thornhill, K. L., Voigt, C., Wang, H., Winstead, E., Zhang, B., Ziemba, L., and Sorooshian, A.: Aerosol responses to precipitation along North American air trajectories arriving at Bermuda, *Atmos. Chem. Phys.*, 21, 16121-16141, 10.5194/acp-21-16121-2021, 2021a.

Dadashazar, H., Crosbie, E., Choi, Y., Corral, A. F., DiGangi, J. P., Diskin, G. S., Dmitrovic, S., Kirschler, S., McCauley, K., Moore, R. H., Nowak, J. B., Robinson, C. E., Schlosser, J., Shook, M., Thornhill, K. L., Voigt, C., Winstead, E. L., Ziemba, L. D., and Sorooshian, A.: Analysis of MONARC and ACTIVATE Airborne Aerosol Data for Aerosol-Cloud Interaction Investigations: Efficacy of Stairstepping Flight Legs for Airborne In Situ Sampling, *Atmosphere*, 13, 1242, 2022.

Dadashazar, H., Painemal, D., Alipanah, M., Brunke, M., Chellappan, S., Corral, A. F., Crosbie, E., Kirschler, S., Liu, H., Moore, R. H., Robinson, C., Scarino, A. J., Shook, M., Sinclair, K., Thornhill, K. L., Voigt, C., Wang, H., Winstead, E., Zeng, X., Ziemba, L., Zuidema, P., and Sorooshian, A.: Cloud drop number concentrations over the western North Atlantic Ocean: seasonal cycle, aerosol interrelationships, and other influential factors, *Atmos. Chem. Phys.*, 21, 10499-10526, 10.5194/acp-21-10499-2021, 2021b.

Diskin, G., Podolske, J., Sachse, G., and Slate, T.: Open-path airborne tunable diode laser hygrometer, *International Symposium on Optical Science and Technology, SPIE2002*.

Ebert, M., Weinbruch, S., Hoffmann, P., and Ortner, H. M.: The chemical composition and complex refractive index of rural and urban influenced aerosols determined by individual particle analysis, *Atmospheric Environment*, 38, 6531-6545, <https://doi.org/10.1016/j.atmosenv.2004.08.048>, 2004.

Fernald, F. G.: Analysis of atmospheric lidar observations: some comments, *Appl. Opt.*, 23, 652-653, 10.1364/AO.23.000652, 1984.

Field, C., Barros, V., Dokken, D., Mach, K., Mastrandrea, M., Bilir, T., Chatterjee, M., Ebi, K., Estrada, Y., Genova, R., Girma, B., Kissel, E., Levy, A., MacCracken, S., Mastrandrea, P., and White, L.: IPCC, 2014: Summary for policymakers. *Climate Change 2014: Impacts, Adaptation, and Vulnerability*, Cambridge University Press, 2014.

Fu, G., Hasekamp, O., Rietjens, J., Smit, M., Di Noia, A., Cairns, B., Wasilewski, A., Diner, D., Seidel, F., Xu, F., Knobelspiesse, K., Gao, M., da Silva, A., Burton, S., Hostetler, C., Hair, J., and Ferrare, R.: Aerosol retrievals from different polarimeters during the ACEPOL campaign using a common retrieval algorithm, *Atmos. Meas. Tech.*, 13, 553-573, 10.5194/amt-13-553-2020, 2020.

Gasteiger, J. and Wiegner, M.: MOPSMAP v1.0: a versatile tool for the modeling of aerosol optical properties, *Geosci. Model Dev.*, 11, 2739-2762, 10.5194/gmd-11-2739-2018, 2018.

Hair, J. W., Hostetler, C. A., Cook, A. L., Harper, D. B., Ferrare, R. A., Mack, T. L., Welch, W., Izquierdo, L. R., and Hovis, F. E.: Airborne High Spectral Resolution Lidar for profiling aerosol optical properties, *Appl. Opt.*, 47, 6734-6752, 10.1364/AO.47.006734, 2008.

Knobelspiesse, K., Cairns, B., Ottaviani, M., Ferrare, R., Hair, J., Hostetler, C., Obland, M., Rogers, R., Redemann, J., Shinozuka, Y., Clarke, A., Freitag, S., Howell, S., Kapustin, V., and McNaughton, C.: Combined retrievals of boreal forest fire aerosol properties with a polarimeter and lidar, *Atmos. Chem. Phys.*, 11, 7045-7067, 10.5194/acp-11-7045-2011, 2011.

McNaughton, C. S., Clarke, A. D., Howell, S. G., Pinkerton, M., Anderson, B., Thornhill, L., Hudgins, C., Winstead, E., Dibb, J. E., Scheuer, E., and Maring, H.: Results from the DC-8 Inlet Characterization Experiment (DICE): Airborne Versus Surface Sampling of Mineral Dust and Sea Salt Aerosols, *Aerosol Science and Technology*, 41, 136-159, 10.1080/02786820601118406, 2007.

Müller, D., Hostetler, C. A., Ferrare, R. A., Burton, S. P., Chemyakin, E., Kolgotin, A., Hair, J. W., Cook, A. L., Harper, D. B., Rogers, R. R., Hare, R. W., Cleckner, C. S., Obland, M. D., Tomlinson, J., Berg, L. K., and Schmid, B.: Airborne Multiwavelength High Spectral Resolution Lidar (HSRL-2) observations during TCAP 2012: vertical profiles of optical and microphysical properties of a smoke/urban haze plume over the northeastern coast of the US, *Atmos. Meas. Tech.*, 7, 3487-3496, 10.5194/amt-7-3487-2014, 2014.

Nessler, R., Weingartner, E., and Baltensperger, U.: Effect of humidity on aerosol light absorption and its implications for extinction and the single scattering albedo illustrated for a site in the lower free troposphere, *Journal of Aerosol Science*, 36, 958-972, <https://doi.org/10.1016/j.jaerosci.2004.11.012>, 2005.

Painemal, D., Corral, A. F., Sorooshian, A., Brunke, M. A., Chellappan, S., Afzali Gorooh, V., Ham, S.-H., O'Neill, L., Smith Jr., W. L., Tselioudis, G., Wang, H., Zeng, X., and Zuidema, P.: An Overview of Atmospheric Features Over the Western North Atlantic Ocean and North American East Coast—Part 2: Circulation, Boundary Layer, and

Clouds, *Journal of Geophysical Research: Atmospheres*, 126, e2020JD033423, <https://doi.org/10.1029/2020JD033423>, 2021.

Petters, M. D. and Kreidenweis, S. M.: A single parameter representation of hygroscopic growth and cloud condensation nucleus activity, *Atmos. Chem. Phys.*, 7, 1961-1971, 10.5194/acp-7-1961-2007, 2007.

Pistone, K., Redemann, J., Doherty, S., Zuidema, P., Burton, S., Cairns, B., Cochrane, S., Ferrare, R., Flynn, C., Freitag, S., Howell, S. G., Kacenelenbogen, M., LeBlanc, S., Liu, X., Schmidt, K. S., Sedlacek Iii, A. J., Segal-Rozenhaimer, M., Shinozuka, Y., Stamnes, S., van Diedenhoven, B., Van Harten, G., and Xu, F.: Intercomparison of biomass burning aerosol optical properties from in situ and remote-sensing instruments in ORACLES-2016, *Atmos. Chem. Phys.*, 19, 9181-9208, 10.5194/acp-19-9181-2019, 2019.

Quinn, P. K., Bates, T. S., Coffman, D. J., Upchurch, L., Johnson, J. E., Moore, R., Ziemba, L., Bell, T. G., Saltzman, E. S., Graff, J., and Behrenfeld, M. J.: Seasonal Variations in Western North Atlantic Remote Marine Aerosol Properties, *Journal of Geophysical Research: Atmospheres*, 124, 14240-14261, <https://doi.org/10.1029/2019JD031740>, 2019.

Reid, J. S., Maring, H. B., Narisma, G. T., van den Heever, S., Di Girolamo, L., Ferrare, R., Lawson, P., Mace, G. G., Simpas, J. B., Tanelli, S., Ziemba, L., van Diedenhoven, B., Bruintjies, R., Bucholtz, A., Cairns, B., Cambaliza, M. O., Chen, G., Diskin, G. S., Flynn, J. H., Hostetler, C. A., Holz, R. E., Lang, T. J., Schmidt, K. S., Smith, G., Sorooshian, A., Thompson, E. J., Thornhill, K. L., Trepte, C., Wang, J., Woods, S., Yoon, S., Alexandrov, M., Alvarez, S., Amiot, C. G., Bennett, J. R., Brooks, M., Burton, S. P., Cayan, E., Chen, H., Collow, A., Crosbie, E., DaSilva, A., DiGangi, J. P., Flagg, D. D., Freeman, S. W., Fu, D., Fukada, E., Hilario, M. R. A., Hong, Y., Hristova-Veleva, S. M., Kuehn, R., Kowch, R. S., Leung, G. R., Loveridge, J., Meyer, K., Miller, R. M., Montes, M. J., Moum, J. N., Nenes, A., Nesbitt, S. W., Norgren, M., Nowotnick, E. P., Rauber, R. M., Reid, E. A., Rutledge, S., Schlosser, J. S., Sekiyama, T. T., Shook, M. A., Sokolowsky, G. A., Stamnes, S. A., Tanaka, T. Y., Wasilewski, A., Xian, P., Xiao, Q., Xu, Z., and Zavaleta, J.: The Coupling Between Tropical Meteorology, Aerosol Lifecycle, Convection, and Radiation during the Cloud, Aerosol and Monsoon Processes Philippines Experiment (CAMP2Ex), *Bulletin of the American Meteorological Society*, 104, E1179-E1205, <https://doi.org/10.1175/BAMS-D-21-0285.1>, 2023.

Sawamura, P., Moore, R. H., Burton, S. P., Chemyakin, E., Müller, D., Kolgotin, A., Ferrare, R. A., Hostetler, C. A., Ziemba, L. D., Beyersdorf, A. J., and Anderson, B. E.: HSRL-2 aerosol optical measurements and microphysical retrievals vs. airborne in situ measurements during DISCOVER-AQ 2013: an intercomparison study, *Atmos. Chem. Phys.*, 17, 7229-7243, 10.5194/acp-17-7229-2017, 2017.

Schlosser, J. S., Bennett, R., Cairns, B., Chen, G., Collister, B. L., Hair, J. W., Jones, M., Shook, M. A., Sorooshian, A., Thornhill, K. L., Ziemba, L. D., and Stamnes, S.: Maximizing the Volume of Collocated Data from Two Coordinated Suborbital Platforms, *Journal of Atmospheric and Oceanic Technology*, 41, 189-201, <https://doi.org/10.1175/JTECH-D-23-0001.1>, 2024.

Schlosser, J. S., Stamnes, S., Burton, S. P., Cairns, B., Crosbie, E., Van Dierenhoven, B., Diskin, G., Dmitrovic, S., Ferrare, R., Hair, J. W., Hostetler, C. A., Hu, Y., Liu, X., Moore, R. H., Shingler, T., Shook, M. A., Thornhill, K. L., Winstead, E., Ziemba, L., and Sorooshian, A.: Polarimeter + Lidar–Derived Aerosol Particle Number Concentration, *Frontiers in Remote Sensing*, 3, 10.3389/frsen.2022.885332, 2022.

Sinclair, K., van Dierenhoven, B., Cairns, B., Alexandrov, M., Moore, R., Crosbie, E., and Ziemba, L.: Polarimetric retrievals of cloud droplet number concentrations, *Remote Sensing of Environment*, 228, 227-240, <https://doi.org/10.1016/j.rse.2019.04.008>, 2019.

Sorooshian, A., Corral, A. F., Braun, R. A., Cairns, B., Crosbie, E., Ferrare, R., Hair, J., Kleb, M. M., Hossein Mardi, A., Maring, H., McComiskey, A., Moore, R., Painemal, D., Scarino, A. J., Schlosser, J., Shingler, T., Shook, M., Wang, H., Zeng, X., Ziemba, L., and Zuidema, P.: Atmospheric Research Over the Western North Atlantic Ocean Region and North American East Coast: A Review of Past Work and Challenges Ahead, *Journal of Geophysical Research: Atmospheres*, 125, e2019JD031626, <https://doi.org/10.1029/2019JD031626>, 2020.

Sorooshian, A., Anderson, B., Bauer, S. E., Braun, R. A., Cairns, B., Crosbie, E., Dadashazar, H., Diskin, G., Ferrare, R., Flagan, R. C., Hair, J., Hostetler, C., Jonsson, H. H., Kleb, M. M., Liu, H., MacDonald, A. B., McComiskey, A., Moore, R., Painemal, D., Russell, L. M., Seinfeld, J. H., Shook, M., Smith, W. L., Thornhill, K., Tselioudis, G., Wang, H., Zeng, X., Zhang, B., Ziemba, L., and Zuidema, P.: Aerosol–Cloud–Meteorology Interaction Airborne Field Investigations: Using Lessons Learned from the U.S. West Coast in the Design of ACTIVATE off the U.S. East Coast, *Bulletin of the American Meteorological Society*, 100, 1511-1528, <https://doi.org/10.1175/BAMS-D-18-0100.1>, 2019.

Sorooshian, A., Alexandrov, M. D., Bell, A. D., Bennett, R., Betito, G., Burton, S. P., Buzanowicz, M. E., Cairns, B., Sorooshian, A., Alexandrov, M. D., Bell, A. D., Bennett, R., Betito, G., Burton, S. P., Buzanowicz, M. E., Cairns, B., Chemyakin, E. V., Chen, G., Choi, Y., Collister, B. L., Cook, A. L., Corral, A. F., Crosbie, E. C., van Dierenhoven, B., DiGangi, J. P., Diskin, G. S., Dmitrovic, S., Edwards, E. L., Fenn, M. A., Ferrare, R. A., van Gilst, D., Hair, J. W., Harper, D. B., Hilario, M. R. A., Hostetler, C. A., Jester, N., Jones, M., Kirschler, S., Kleb, M. M., Kusterer, J. M., Leavor, S., Lee, J. W., Liu, H., McCauley, K., Moore, R. H., Nied, J., Notari, A., Nowak, J. B., Painemal, D., Phillips, K. E., Robinson, C. E., Scarino, A. J., Schlosser, J. S., Seaman, S. T., Seethala, C., Shingler, T. J., Shook, M. A., Sinclair, K. A., Smith Jr, W. L., Spangenberg, D. A., Stamnes, S. A., Thornhill, K. L., Voigt, C., Vömel, H., Wasilewski, A. P., Wang, H., Winstead, E. L., Zeider, K., Zeng, X., Zhang, B., Ziemba, L. D., and Zuidema, P.: Spatially-coordinated airborne data and complementary products for aerosol, gas, cloud, and meteorological studies: The NASA ACTIVATE dataset, *ESSD*, 2023, 1-79, 10.5194/essd-2023-109, 2023.

Sorribas, M., Olmo, F. J., Quirantes, A., Lyamani, H., Gil-Ojeda, M., Alados-Arboledas, L., and Horvath, H.: Role of spheroidal particles in closure studies for aerosol microphysical–optical properties, *Quarterly Journal of the Royal Meteorological Society*, 141, 2700-2707, <https://doi.org/10.1002/qj.2557>, 2015.

Stamnes, S., Hostetler, C., Ferrare, R., Burton, S., Liu, X., Hair, J., Hu, Y., Wasilewski, A., Martin, W., van Diedenhoven, B., Chowdhary, J., Cetinić, I., Berg, L. K., Stamnes, K., and Cairns, B.: Simultaneous polarimeter retrievals of microphysical aerosol and ocean color parameters from the “MAPP” algorithm with comparison to high-spectral-resolution lidar aerosol and ocean products, *Appl. Opt.*, 57, 2394-2413, 10.1364/AO.57.002394, 2018.

Veselovskii, I., Dubovik, O., Kolgotin, A., Lapyonok, T., Di Girolamo, P., Summa, D., Whiteman, D. N., Mishchenko, M., and Tanré, D.: Application of randomly oriented spheroids for retrieval of dust particle parameters from multiwavelength lidar measurements, *Journal of Geophysical Research: Atmospheres*, 115, <https://doi.org/10.1029/2010JD014139>, 2010.

Voshchinnikov, N. V. and Farafonov, V. G.: Optical properties of spheroidal particles, *Astrophysics and Space Science*, 204, 19-86, 10.1007/BF00658095, 1993.

Wagner, R., Ajtai, T., Kandler, K., Lieke, K., Linke, C., Müller, T., Schnaiter, M., and Vragel, M.: Complex refractive indices of Saharan dust samples at visible and near UV wavelengths: a laboratory study, *Atmos. Chem. Phys.*, 12, 2491-2512, 10.5194/acp-12-2491-2012, 2012.

Wu, L., Hasekamp, O., van Diedenhoven, B., and Cairns, B.: Aerosol retrieval from multiangle, multispectral photopolarimetric measurements: importance of spectral range and angular resolution, *Atmos. Meas. Tech.*, 8, 2625-2638, 10.5194/amt-8-2625-2015, 2015.

Zieger, P., Fierz-Schmidhauser, R., Weingartner, E., and Baltensperger, U.: Effects of relative humidity on aerosol light scattering: results from different European sites, *Atmos. Chem. Phys.*, 13, 10609-10631, 10.5194/acp-13-10609-2013, 2013.

APPENDIX C: AUTHOR'S PUBLICATIONS

Below is a complete list of the author's journal publications and conference presentations while enrolled as a Ph.D. student in the Sorooshian Group at the University of Arizona.

FIRST AUTHOR JOURNAL PUBLICATIONS

Dmitrovic, S., Schlosser, J.S., Bennett, R., Cairns, B., Chen, G., Collister, B.L., Hair, J.W., Jones, M., Reid, J.S., Shook, M.A., Sorooshian, A., Thornhill, K.L, Ziemba, L.D., and Stamnes, S.: Closing the gap between in-situ and remotely sensed aerosol particle properties, **in preparation for submission to Atmospheric Measurement Techniques (AMT) journal.**

Dmitrovic, S., Hair, J. W., Collister, B. L., Crosbie, E., Fenn, M. A., Ferrare, R. A., Harper, D. B., Hostetler, C. A., Hu, Y., Reagan, J. A., Robinson, C. E., Seaman, S. T., Shingler, T. J., Thornhill, K. L., Vömel, H., Zeng, X., and Sorooshian, A.: High Spectral Resolution Lidar – generation 2 (HSRL-2) Retrievals of Ocean Surface Wind Speed: Methodology and Evaluation, *Atmos. Meas. Tech.*, 2023, 1-33, 10.5194/egusphere-2023-1943, **accepted 15 April 2024.**

CONFERENCE POSTER PRESENTATIONS

Dmitrovic, S., Schlosser, J.S., Bennett, R., Cairns, B., Chen, G., Collister, B.L., Hair, J.W., Jones, M., Reid, J.S., Shook, M.A., Sorooshian, A., Thornhill, K.L., Ziemba, L.D., and Stamnes, S.: Advancing Field Campaign Data Quality Assurance Through Closure of In-Situ and Remote Sensing Data Sets, in *American Geophysical Union (AGU) Fall Meeting*, 11 – 15 December 2023.

Dmitrovic, S., Hair, J.W., Ferrare, R.A., Fenn, M.A., Hostetler, C.A., Thornhill, K.L., Robinson, C.E., Zeng, X., Reagan, J.A., and Sorooshian, A. “The Validation of Airborne High Spectral Resolution Lidar 2 (HSRL-2) Retrievals for the Estimation of Ocean Surface Wind Speeds,” in *American Geophysical Union (AGU) Fall Meeting*, 12 – 16 December 2022.

CO-AUTHORED JOURNAL PUBLICATIONS

Li, X., Wang, H., Christensen, M.W., Chen, J., Tang, S., Kirschler, S., Crosbie, E., Ziemba, L.D., Painemal, D., Corral, A., McCauley, K.A., **Dmitrovic, S.**, Sorooshian, A., Fenn, M.A., Schlosser, J., Stamnes, S., Hair, J., Cairns, B., Moore, R.H., Ferrare, R., Shook, M., Choi, Y.,

Diskin, G.S., DiGangi, J.P., Nowak, J.B., Robinson, C.E., Shingler, T., Thornhill, K.L., and Voigt, C.: Process Modeling of Aerosol-cloud Interaction in Summertime Precipitating Shallow Cumulus over the Western North Atlantic, ESS Open Archive, 10.22541/essoar.168748394.49974536/v1, 2023.

Sorooshian, A., Alexandrov, M. D., Bell, A. D., Bennett, R., Betito, G., Burton, S. P., Buzanowicz, M. E., Cairns, B., Chemyakin, E. V., Chen, G., Choi, Y., Collister, B. L., Cook, A. L., Corral, A. F., Crosbie, E. C., van Dierenhoven, B., DiGangi, J. P., Diskin, G. S., Dmitrovic, S., Edwards, E. L., Fenn, M. A., Ferrare, R. A., van Gilst, D., Hair, J. W., Harper, D. B., Hilario, M. R. A., Hostetler, C. A., Jester, N., Jones, M., Kirschler, S., Kleb, M. M., Kusterer, J. M., Leavor, S., Lee, J. W., Liu, H., McCauley, K., Moore, R. H., Nied, J., Notari, A., Nowak, J. B., Painemal, D., Phillips, K. E., Robinson, C. E., Scarino, A. J., Schlosser, J. S., Seaman, S. T., Seethala, C., Shingler, T. J., Shook, M. A., Sinclair, K. A., Smith Jr, W. L., Spangenberg, D. A., Stamnes, S. A., Thornhill, K. L., Voigt, C., Vömel, H., Wasilewski, A. P., Wang, H., Winstead, E. L., Zeider, K., Zeng, X., Zhang, B., Ziemba, L. D., and Zuidema, P.: Spatially-coordinated airborne data and complementary products for aerosol, gas, cloud, and meteorological studies: The NASA ACTIVATE dataset, ESSD, 2023, 1-79, 10.5194/essd-2023-109, 2023.

Shahnaz, R., Golamhasan, M., Saeed, J., Ali Mohammad, K., Sorooshian, A., **Dmitrovic, S.**, and Sapna, T.: On the Nature of Caspian Clouds, Journal of Meteorological Research, 37, 262-272, 10.1007/s13351-023-2167-x, 2023.

Dadashazar, H., Crosbie, E., Choi, Y., Corral, A. F., DiGangi, J. P., Diskin, G. S., **Dmitrovic, S.**, Kirschler, S., McCauley, K., Moore, R. H., Nowak, J. B., Robinson, C. E., Schlosser, J., Shook, M., Thornhill, K. L., Voigt, C., Winstead, E. L., Ziemba, L. D., and Sorooshian, A.: Analysis of MONARC and ACTIVATE Airborne Aerosol Data for Aerosol-Cloud Interaction Investigations: Efficacy of Stairstepping Flight Legs for Airborne In Situ Sampling, Atmosphere, 13, 1242, 2022.

Dadashazar, H., Corral, A. F., Crosbie, E., **Dmitrovic, S.**, Kirschler, S., McCauley, K., Moore, R., Robinson, C., Schlosser, J. S., Shook, M., Thornhill, K. L., Voigt, C., Winstead, E., Ziemba, L., and Sorooshian, A.: Organic enrichment in droplet residual particles relative to out of cloud

over the northwestern Atlantic: analysis of airborne ACTIVATE data, *Atmos. Chem. Phys.*, 22, 13897-13913, 10.5194/acp-22-13897-2022, 2022a.

Schlosser, J. S., Starnes, S., Burton, S. P., Cairns, B., Crosbie, E., Van Dierenhoven, B., Diskin, G., **Dmitrovic, S.**, Ferrare, R., Hair, J. W., Hostetler, C. A., Hu, Y., Liu, X., Moore, R. H., Shingler, T., Shook, M. A., Thornhill, K. L., Winstead, E., Ziemba, L., and Sorooshian, A.: Polarimeter + Lidar–Derived Aerosol Particle Number Concentration, *Frontiers in Remote Sensing*, 3, 10.3389/frsen.2022.885332, 2022.

DISSERTATION REFERENCES

Below is a list of references used in Chapters 1 and 2 of this dissertation. For the full list of references used in each manuscript, please refer to Appendix A and B.

ACTIVATE Science Team: Aerosol Cloud meteorology Interactions over the western Atlantic Experiment Data [dataset], doi.org/10.5067/SUBORBITAL/ACTIVATE/DATA001, 2020.

ACTIVATE – Aerosol Cloud meteorology Interactions over the western Atlantic Experiment: <https://www-air.larc.nasa.gov/missions/activate/index.html>, last

Aldhaif, A. M., Lopez, D. H., Dadashazar, H., and Sorooshian, A.: Sources, frequency, and chemical nature of dust events impacting the United States East Coast, *Atmospheric Environment*, 231, 117456, <https://doi.org/10.1016/j.atmosenv.2020.117456>, 2020.

Bedka, K. M., Nehrir, A. R., Kavaya, M., Barton-Grimley, R., Beaubien, M., Carroll, B., Collins, J., Cooney, J., Emmitt, G. D., Greco, S., Kooi, S., Lee, T., Liu, Z., Rodier, S., and Skofronick-Jackson, G.: Airborne lidar observations of wind, water vapor, and aerosol profiles during the NASA Aeolus calibration and validation (Cal/Val) test flight campaign, *Atmos. Meas. Tech.*, 14, 4305-4334, 10.5194/amt-14-4305-2021, 2021.

Bellouin, N., Quaas, J., Gryspeerdt, E., Kinne, S., Stier, P., Watson-Parris, D., Boucher, O., Carslaw, K. S., Christensen, M., Daniau, A.-L., Dufresne, J.-L., Feingold, G., Fiedler, S., Forster, P., Gettelman, A., Haywood, J. M., Lohmann, U., Malavelle, F., Mauritsen, T., McCoy, D. T., Myhre, G., Mülmenstädt, J., Neubauer, D., Possner, A., Rugenstein, M., Sato, Y., Schulz, M., Schwartz, S. E., Sourdeval, O., Storelvmo, T., Toll, V., Winker, D., and Stevens, B.: Bounding Global Aerosol Radiative Forcing of Climate Change, *Reviews of Geophysics*, 58, e2019RG000660, <https://doi.org/10.1029/2019RG000660>, 2020.

Bi, L., Lin, W., Wang, Z., Tang, X., Zhang, X., and Yi, B.: Optical Modeling of Sea Salt Aerosols: The Effects of Nonsphericity and Inhomogeneity, *Journal of Geophysical Research: Atmospheres*, 123, 543-558, 10.1002/2017jd027869, 2018.

Bohren, C. F. and Huffman, D. R.: *Absorption and Scattering of Light by Small Particles*, Wiley 2008.

Bourassa, M. A., Meissner, T., Cerovecki, I., Chang, P. S., Dong, X., De Chiara, G., Donlon, C., Dukhovskoy, D. S., Elya, J., Fore, A., Fewings, M. R., Foster, R. C., Gille, S. T., Haus, B. K., Hristova-Veleva, S., Holbach, H. M., Jelenak, Z., Knaff, J. A., Kranz, S. A., Manaster, A., Mazloff, M., Mears, C., Mouche, A., Portabella, M., Reul, N., Ricciardulli, L., Rodriguez, E., Sampson, C., Solis, D., Stoffelen, A., Stukel, M. R., Stiles, B., Weissman, D., and Wentz, F.: Remotely Sensed Winds and Wind Stresses for Marine Forecasting and Ocean Modeling, *Frontiers in Marine Science*, 6, 10.3389/fmars.2019.00443, 2019.

Brunke, M. A., Cutler, L., Urzua, R. D., Corral, A. F., Crosbie, E., Hair, J., Hostetler, C., Kirschler, S., Larson, V., Li, X.-Y., Ma, P.-L., Minke, A., Moore, R., Robinson, C. E., Scarino, A. J., Schlosser, J., Shook, M., Sorooshian, A., Lee Thornhill, K., Voigt, C., Wan, H., Wang, H., Winstead, E., Zeng, X., Zhang, S., and Ziemba, L. D.: Aircraft Observations of Turbulence in Cloudy and Cloud-Free Boundary Layers Over the Western North Atlantic Ocean From ACTIVATE and Implications for the Earth System Model Evaluation and Development, *Journal of Geophysical Research: Atmospheres*, 127, e2022JD036480, <https://doi.org/10.1029/2022JD036480>, 2022.

Burton, S. P., Chemyakin, E., Liu, X., Knobelspiesse, K., Stamnes, S., Sawamura, P., Moore, R. H., Hostetler, C. A., and Ferrare, R. A.: Information content and sensitivity of the $3\beta + 2\alpha$ lidar measurement system for aerosol microphysical retrievals, *Atmos. Meas. Tech.*, 9, 5555-5574, 10.5194/amt-9-5555-2016, 2016.

Burton, S. P., Ferrare, R. A., Hostetler, C. A., Hair, J. W., Rogers, R. R., Obland, M. D., Butler, C. F., Cook, A. L., Harper, D. B., and Froyd, K. D.: Aerosol classification using airborne High Spectral Resolution Lidar measurements – methodology and examples, *Atmos. Meas. Tech.*, 5, 73-98, 10.5194/amt-5-73-2012, 2012.

Burton, S. P., Hostetler, C. A., Cook, A. L., Hair, J. W., Seaman, S. T., Scola, S., Harper, D. B., Smith, J. A., Fenn, M. A., Ferrare, R. A., Saide, P. E., Chemyakin, E. V., and Müller, D.: Calibration of a high spectral resolution lidar using a Michelson interferometer, with data examples from ORACLES, *Appl. Opt.*, 57, 6061-6075, 10.1364/AO.57.006061, 2018.

Cairns, B., Russell, E., and Travis, L.: Research Scanning Polarimeter: calibration and ground-based measurements, SPIE's International Symposium on Optical Science, Engineering, and Instrumentation, SPIE1999.

Cairns, B., Russell, E., LaVeigne, J., and Tennant, P.: Research scanning polarimeter and airborne usage for remote sensing of aerosols, Optical Science and Technology, SPIE's 48th Annual Meeting, SPIE2003.

Carvalho, D.: An Assessment of NASA's GMAO MERRA-2 Reanalysis Surface Winds, Journal of Climate, 32, 8261-8281, <https://doi.org/10.1175/JCLI-D-19-0199.1>, 2019.

Chemyakin, E., Stamnes, S., Hair, J., Burton, S. P., Bell, A., Hostetler, C., Ferrare, R., Chowdhary, J., Moore, R., Ziemba, L., Crosbie, E., Robinson, C., Shook, M., Thornhill, L., Winstead, E., Hu, Y., van Dienenhoven, B., and Cairns, B.: Efficient single-scattering look-up table for lidar and polarimeter water cloud studies, Opt. Lett., 48, 13-16, 10.1364/OL.474282, 2023.

Chen, G., Ziemba, L. D., Chu, D. A., Thornhill, K. L., Schuster, G. L., Winstead, E. L., Diskin, G. S., Ferrare, R. A., Burton, S. P., Ismail, S., Kooi, S. A., Omar, A. H., Slusher, D. L., Kleb, M. M., Reid, J. S., Twohy, C. H., Zhang, H., and Anderson, B. E.: Observations of Saharan dust microphysical and optical properties from the Eastern Atlantic during NAMMA airborne field campaign, Atmos. Chem. Phys., 11, 723-740, 10.5194/acp-11-723-2011, 2011.

Chen, J., Wang, H., Li, X., Painemal, D., Sorooshian, A., Thornhill, K. L., Robinson, C., and Shingler, T.: Impact of Meteorological Factors on the Mesoscale Morphology of Cloud Streets during a Cold-Air Outbreak over the Western North Atlantic, Journal of the Atmospheric Sciences, 79, 2863-2879, <https://doi.org/10.1175/JAS-D-22-0034.1>, 2022.

Christoudias, T., Pozzer, A., and Lelieveld, J.: Influence of the North Atlantic Oscillation on air pollution transport, Atmos. Chem. Phys., 12, 869-877, 10.5194/acp-12-869-2012, 2012.

Colón-Robles, M., Rauber, R. M., and Jensen, J. B.: Influence of low-level wind speed on droplet spectra near cloud base in trade wind cumulus, Geophysical Research Letters, 33, <https://doi.org/10.1029/2006GL027487>, 2006.

Corral, A. F., Braun, R. A., Cairns, B., Gorrooh, V. A., Liu, H., Ma, L., Mardi, A. H., Painemal, D., Stamnes, S., van Dierenhoven, B., Wang, H., Yang, Y., Zhang, B., and Sorooshian, A.: An Overview of Atmospheric Features Over the Western North Atlantic Ocean and North American East Coast – Part 1: Analysis of Aerosols, Gases, and Wet Deposition Chemistry, *Journal of Geophysical Research: Atmospheres*, 126, e2020JD032592, <https://doi.org/10.1029/2020JD032592>, 2021.

Corral, A. F., Choi, Y., Crosbie, E., Dadashazar, H., DiGangi, J. P., Diskin, G. S., Fenn, M., Harper, D. B., Kirschler, S., Liu, H., Moore, R. H., Nowak, J. B., Scarino, A. J., Seaman, S., Shingler, T., Shook, M. A., Thornhill, K. L., Voigt, C., Zhang, B., Ziemba, L. D., and Sorooshian, A.: Cold Air Outbreaks Promote New Particle Formation Off the U.S. East Coast, *Geophysical Research Letters*, 49, e2021GL096073, <https://doi.org/10.1029/2021GL096073>, 2022.

Cox, C. and Munk, W.: Measurement of the Roughness of the Sea Surface from Photographs of the Sun's Glitter, *J. Opt. Soc. Am.*, 44, 838-850, 10.1364/JOSA.44.000838, 1954.

Creilson, J. K., Fishman, J., and Wozniak, A. E.: Intercontinental transport of tropospheric ozone: a study of its seasonal variability across the North Atlantic utilizing tropospheric ozone residuals and its relationship to the North Atlantic Oscillation, *Atmos. Chem. Phys.*, 3, 2053-2066, 10.5194/acp-3-2053-2003, 2003.

Dadashazar, H., Alipanah, M., Hilario, M. R. A., Crosbie, E., Kirschler, S., Liu, H., Moore, R. H., Peters, A. J., Scarino, A. J., Shook, M., Thornhill, K. L., Voigt, C., Wang, H., Winstead, E., Zhang, B., Ziemba, L., and Sorooshian, A.: Aerosol responses to precipitation along North American air trajectories arriving at Bermuda, *Atmos. Chem. Phys.*, 21, 16121-16141, 10.5194/acp-21-16121-2021, 2021a.

Dadashazar, H., Crosbie, E., Choi, Y., Corral, A. F., DiGangi, J. P., Diskin, G. S., Dmitrovic, S., Kirschler, S., McCauley, K., Moore, R. H., Nowak, J. B., Robinson, C. E., Schlosser, J., Shook, M., Thornhill, K. L., Voigt, C., Winstead, E. L., Ziemba, L. D., and Sorooshian, A.: Analysis of MONARC and ACTIVATE Airborne Aerosol Data for Aerosol-Cloud Interaction Investigations: Efficacy of Stairstepping Flight Legs for Airborne In Situ Sampling, *Atmosphere*, 13, 1242, 2022.

Dadashazar, H., Painemal, D., Alipanah, M., Brunke, M., Chellappan, S., Corral, A. F., Crosbie, E., Kirschler, S., Liu, H., Moore, R. H., Robinson, C., Scarino, A. J., Shook, M., Sinclair, K., Thornhill, K. L., Voigt, C., Wang, H., Winstead, E., Zeng, X., Ziemba, L., Zuidema, P., and Sorooshian, A.: Cloud drop number concentrations over the western North Atlantic Ocean: seasonal cycle, aerosol interrelationships, and other influential factors, *Atmos. Chem. Phys.*, 21, 10499-10526, 10.5194/acp-21-10499-2021, 2021b.

Dierssen, H. M.: Hyperspectral Measurements, Parameterizations, and Atmospheric Correction of Whitecaps and Foam From Visible to Shortwave Infrared for Ocean Color Remote Sensing, *Frontiers in Earth Science*, 7, 10.3389/feart.2019.00014, 2019.

Diskin, G., Podolske, J., Sachse, G., and Slate, T.: Open-path airborne tunable diode laser hygrometer, *International Symposium on Optical Science and Technology, SPIE2002*.

Ebert, M., Weinbruch, S., Hoffmann, P., and Ortner, H. M.: The chemical composition and complex refractive index of rural and urban influenced aerosols determined by individual particle analysis, *Atmospheric Environment*, 38, 6531-6545, <https://doi.org/10.1016/j.atmosenv.2004.08.048>, 2004.

Fernald, F. G.: Analysis of atmospheric lidar observations: some comments, *Appl. Opt.*, 23, 652-653, 10.1364/AO.23.000652, 1984.

Fernández, P., Speich, S., Borgnino, M., Meroni, A. N., Desbiolles, F., and Pasquero, C.: On the importance of the atmospheric coupling to the small-scale ocean in the modulation of latent heat flux, *Frontiers in Marine Science*, 10, 10.3389/fmars.2023.1136558, 2023.

Ferrare, R., Hair, J., Hostetler, C., Shingler, T., Burton, S. P., Fenn, M., Clayton, M., Scarino, A. J., Harper, D., Seaman, S., Cook, A., Crosbie, E., Winstead, E., Ziemba, L., Thornhill, L., Robinson, C., Moore, R., Vaughan, M., Sorooshian, A., Schlosser, J. S., Liu, H., Zhang, B., Diskin, G., DiGangi, J., Nowak, J., Choi, Y., Zuidema, P., and Chellappan, S.: Airborne HSRL-2 measurements of elevated aerosol depolarization associated with non-spherical sea salt, *Frontiers in Remote Sensing*, 4, 10.3389/frsen.2023.1143944, 2023.

Field, C., Barros, V., Dokken, D., Mach, K., Mastrandrea, M., Bilir, T., Chatterjee, M., Ebi, K., Estrada, Y., Genova, R., Girma, B., Kissel, E., Levy, A., MacCracken, S., Mastrandrea, P., and White, L.: IPCC, 2014: Summary for policymakers. *Climate Change 2014: Impacts, Adaptation, and Vulnerability*, Cambridge University Press, 2014.

Fu, G., Hasekamp, O., Rietjens, J., Smit, M., Di Noia, A., Cairns, B., Wasilewski, A., Diner, D., Seidel, F., Xu, F., Knobelspiesse, K., Gao, M., da Silva, A., Burton, S., Hostetler, C., Hair, J., and Ferrare, R.: Aerosol retrievals from different polarimeters during the ACEPOL campaign using a common retrieval algorithm, *Atmos. Meas. Tech.*, 13, 553-573, 10.5194/amt-13-553-2020, 2020.

Garbe, C. S., Rutgersson, A., Boutin, J., de Leeuw, G., Delille, B., Fairall, C. W., Gruber, N., Hare, J., Ho, D. T., Johnson, M. T., Nightingale, P. D., Pettersson, H., Piskozub, J., Sahlée, E., Tsai, W.-t., Ward, B., Woolf, D. K., and Zappa, C. J.: Transfer Across the Air-Sea Interface, in: *Ocean-Atmosphere Interactions of Gases and Particles*, edited by: Liss, P. S., and Johnson, M. T., Springer Berlin Heidelberg, Berlin, Heidelberg, 55-112, 10.1007/978-3-642-25643-1_2, 2014.

Gasteiger, J. and Wiegner, M.: MOPSMAP v1.0: a versatile tool for the modeling of aerosol optical properties, *Geosci. Model Dev.*, 11, 2739-2762, 10.5194/gmd-11-2739-2018, 2018.

Gasteiger, J., Wiegner, M., Groß, S., Freudenthaler, V., Toledano, C., Tesche, M., and Kandler, K.: Modelling lidar-relevant optical properties of complex mineral dust aerosols, *Tellus B: Chemical and Physical Meteorology*, 63, 725-741, 10.1111/j.1600-0889.2011.00559.x, 2011.

Gelaro, R., McCarty, W., Suárez, M. J., Todling, R., Molod, A., Takacs, L., Randles, C. A., Darmenov, A., Bosilovich, M. G., Reichle, R., Wargan, K., Coy, L., Cullather, R., Draper, C., Akella, S., Buchard, V., Conaty, A., da Silva, A. M., Gu, W., Kim, G.-K., Koster, R., Lucchesi, R., Merkova, D., Nielsen, J. E., Partyka, G., Pawson, S., Putman, W., Rienecker, M., Schubert, S. D., Sienkiewicz, M., and Zhao, B.: The Modern-Era Retrospective Analysis for Research and Applications, Version 2 (MERRA-2), *Journal of Climate*, 30, 5419-5454, <https://doi.org/10.1175/JCLI-D-16-0758.1>, 2017.

GMAO: MERRA-2 tavg1_2d_flux_Nx: 2d, 1-Hourly, Time-Averaged, Single-Level, Assimilation, Surface Flux Diagnostics V5.12.4 [dataset], 2015.

Gordon, H. R. and Wang, M.: Influence of oceanic whitecaps on atmospheric correction of ocean-color sensors, *Appl. Opt.*, 33, 7754-7763, 10.1364/AO.33.007754, 1994.

Gui, K., Che, H., Li, L., Zheng, Y., Zhang, L., Zhao, H., Zhong, J., Yao, W., Liang, Y., Wang, Y., and Zhang, X.: The Significant Contribution of Small-Sized and Spherical Aerosol Particles to the Decreasing Trend in Total Aerosol Optical Depth over Land from 2003 to 2018, *Engineering*, 16, 82-92, <https://doi.org/10.1016/j.eng.2021.05.017>, 2022.

Hair, J. W., Hostetler, C. A., Cook, A. L., Harper, D. B., Ferrare, R. A., Mack, T. L., Welch, W., Izquierdo, L. R., and Hovis, F. E.: Airborne High Spectral Resolution Lidar for profiling aerosol optical properties, *Appl. Opt.*, 47, 6734-6752, 10.1364/AO.47.006734, 2008.

Hale, G. M. and Querry, M. R.: Optical Constants of Water in the 200-nm to 200- μm Wavelength Region, *Appl. Opt.*, 12, 555, 10.1364/ao.12.000555, 1973.

Hu, Y., Stamnes, K., Vaughan, M., Pelon, J., Weimer, C., Wu, D., Cisewski, M., Sun, W., Yang, P., Lin, B., Omar, A., Flittner, D., Hostetler, C., Trepte, C., Winker, D., Gibson, G., and Santa-Maria, M.: Sea surface wind speed estimation from space-based lidar measurements, *Atmos. Chem. Phys.*, 8, 3593-3601, 10.5194/acp-8-3593-2008, 2008.

Huang, Z., Yu, X., Liu, Q., Maki, T., Alam, K., Wang, Y., Xue, F., Tang, S., Du, P., Dong, Q., Wang, D., and Huang, J.: Bioaerosols in the atmosphere: A comprehensive review on detection methods, concentration and influencing factors, *Science of The Total Environment*, 912, 168818, <https://doi.org/10.1016/j.scitotenv.2023.168818>, 2024.

Josset, D., Pelon, J., and Hu, Y.: Multi-Instrument Calibration Method Based on a Multiwavelength Ocean Surface Model, *IEEE Geoscience and Remote Sensing Letters*, 7, 195-199, 10.1109/LGRS.2009.2030906, 2010a.

Josset, D., Pelon, J., Protat, A., and Flamant, C.: New approach to determine aerosol optical depth from combined CALIPSO and CloudSat ocean surface echoes, *Geophysical Research Letters*, 35, <https://doi.org/10.1029/2008GL033442>, 2008.

Josset, D., Zhai, P.-W., Hu, Y., Pelon, J., and Lucker, P. L.: Lidar equation for ocean surface and subsurface, *Opt. Express*, 18, 20862-20875, 10.1364/OE.18.020862, 2010b.

Kahnert, M. and Kanngießer, F.: Optical properties of marine aerosol: modelling the transition from dry, irregularly shaped crystals to brine-coated, dissolving salt particles, *Journal of Quantitative Spectroscopy and Radiative Transfer*, 295, 108408, <https://doi.org/10.1016/j.jqsrt.2022.108408>, 2023.

Kiliyanpilakkil, V. P. and Meskhidze, N.: Deriving the effect of wind speed on clean marine aerosol optical properties using the A-Train satellites, *Atmos. Chem. Phys.*, 11, 11401-11413, 10.5194/acp-11-11401-2011, 2011.

Kirschler, S., Voigt, C., Anderson, B., Campos Braga, R., Chen, G., Corral, A. F., Crosbie, E., Dadashazar, H., Ferrare, R. A., Hahn, V., Hendricks, J., Kaufmann, S., Moore, R., Pöhlker, M. L., Robinson, C., Scarino, A. J., Schollmayer, D., Shook, M. A., Thornhill, K. L., Winstead, E., Ziemba, L. D., and Sorooshian, A.: Seasonal updraft speeds change cloud droplet number concentrations in low-level clouds over the western North Atlantic, *Atmos. Chem. Phys.*, 22, 8299-8319, 10.5194/acp-22-8299-2022, 2022.

Knobelspiesse, K., Cairns, B., Ottaviani, M., Ferrare, R., Hair, J., Hostetler, C., Obland, M., Rogers, R., Redemann, J., Shinozuka, Y., Clarke, A., Freitag, S., Howell, S., Kapustin, V., and McNaughton, C.: Combined retrievals of boreal forest fire aerosol properties with a polarimeter and lidar, *Atmos. Chem. Phys.*, 11, 7045-7067, 10.5194/acp-11-7045-2011, 2011.

Koepke, P.: Effective reflectance of oceanic whitecaps, *Appl. Opt.*, 23, 1816-1824, 10.1364/AO.23.001816, 1984.

Labzovskii, L. D., van Zadelhoff, G. J., Tilstra, L. G., de Kloe, J., Donovan, D. P., and Stoffelen, A.: High sensitivity of Aeolus UV surface returns to surface reflectivity, *Scientific Reports*, 13, 17552, 10.1038/s41598-023-44525-5, 2023.

Lamb, P. J. and Pepler, R. A.: North Atlantic Oscillation: Concept and an Application, *Bulletin of the American Meteorological Society*, 68, 1218-1225, [https://doi.org/10.1175/1520-0477\(1987\)068<1218:NAOCAA>2.0.CO;2](https://doi.org/10.1175/1520-0477(1987)068<1218:NAOCAA>2.0.CO;2), 1987.

Li, Q., Jacob, D. J., Bey, I., Palmer, P. I., Duncan, B. N., Field, B. D., Martin, R. V., Fiore, A. M., Yantosca, R. M., Parrish, D. D., Simmonds, P. G., and Oltmans, S. J.: Transatlantic transport of

pollution and its effects on surface ozone in Europe and North America, *Journal of Geophysical Research: Atmospheres*, 107, ACH 4-1-ACH 4-21, <https://doi.org/10.1029/2001JD001422>, 2002.

Li, X.-Y., Wang, H., Chen, J., Endo, S., George, G., Cairns, B., Chellappan, S., Zeng, X., Kirschler, S., Voigt, C., Sorooshian, A., Crosbie, E., Chen, G., Ferrare, R. A., Gustafson, W. I., Hair, J. W., Kleb, M. M., Liu, H., Moore, R., Painemal, D., Robinson, C., Scarino, A. J., Shook, M., Shingler, T. J., Thornhill, K. L., Tornow, F., Xiao, H., Ziemba, L. D., and Zuidema, P.: Large-Eddy Simulations of Marine Boundary Layer Clouds Associated with Cold-Air Outbreaks during the ACTIVATE Campaign. Part I: Case Setup and Sensitivities to Large-Scale Forcings, *Journal of the Atmospheric Sciences*, 79, 73-100, <https://doi.org/10.1175/JAS-D-21-0123.1>, 2022.

Li, Z., Lemmerz, C., Paffrath, U., Reitebuch, O., and Witschas, B.: Airborne Doppler Lidar Investigation of Sea Surface Reflectance at a 355-nm Ultraviolet Wavelength, *Journal of Atmospheric and Oceanic Technology*, 27, 693-704, <https://doi.org/10.1175/2009JTECHA1302.1>, 2010.

Maetzler, C.: MATLAB Functions for Mie Scattering and Absorption,

Mardi, A. H., Dadashazar, H., Painemal, D., Shingler, T., Seaman, S. T., Fenn, M. A., Hostetler, C. A., and Sorooshian, A.: Biomass Burning Over the United States East Coast and Western North Atlantic Ocean: Implications for Clouds and Air Quality, *Journal of Geophysical Research: Atmospheres*, 126, e2021JD034916, <https://doi.org/10.1029/2021JD034916>, 2021.

Martin, C. and Suhr, I.: NCAR/EOL Atmospheric Sounding Processing ENvironment (ASPEN) software. Version 3.4.5. [dataset], 2021.

McNaughton, C. S., Clarke, A. D., Howell, S. G., Pinkerton, M., Anderson, B., Thornhill, L., Hudgins, C., Winstead, E., Dibb, J. E., Scheuer, E., and Maring, H.: Results from the DC-8 Inlet Characterization Experiment (DICE): Airborne Versus Surface Sampling of Mineral Dust and Sea Salt Aerosols, *Aerosol Science and Technology*, 41, 136-159, 10.1080/02786820601118406, 2007.

Moore, K. D., Voss, K. J., and Gordon, H. R.: Spectral reflectance of whitecaps: Their contribution to water-leaving radiance, *Journal of Geophysical Research: Oceans*, 105, 6493-6499, <https://doi.org/10.1029/1999JC900334>, 2000.

Müller, D., Hostetler, C. A., Ferrare, R. A., Burton, S. P., Chemyakin, E., Kolgotin, A., Hair, J. W., Cook, A. L., Harper, D. B., Rogers, R. R., Hare, R. W., Cleckner, C. S., Obland, M. D., Tomlinson, J., Berg, L. K., and Schmid, B.: Airborne Multiwavelength High Spectral Resolution Lidar (HSRL-2) observations during TCAP 2012: vertical profiles of optical and microphysical properties of a smoke/urban haze plume over the northeastern coast of the US, *Atmos. Meas. Tech.*, 7, 3487-3496, [10.5194/amt-7-3487-2014](https://doi.org/10.5194/amt-7-3487-2014), 2014.

Murphy, A. and Hu, Y.: Retrieving Aerosol Optical Depth and High Spatial Resolution Ocean Surface Wind Speed From CALIPSO: A Neural Network Approach, *Frontiers in Remote Sensing*, 1, [10.3389/frsen.2020.614029](https://doi.org/10.3389/frsen.2020.614029), 2021.

Nair, A. K. M. and Rajeev, K.: Multiyear CloudSat and CALIPSO Observations of the Dependence of Cloud Vertical Distribution on Sea Surface Temperature and Tropospheric Dynamics, *Journal of Climate*, 27, 672-683, <https://doi.org/10.1175/JCLI-D-13-00062.1>, 2014.

Nessler, R., Weingartner, E., and Baltensperger, U.: Effect of humidity on aerosol light absorption and its implications for extinction and the single scattering albedo illustrated for a site in the lower free troposphere, *Journal of Aerosol Science*, 36, 958-972, <https://doi.org/10.1016/j.jaerosci.2004.11.012>, 2005.

Neukermans, G., Harmel, T., Galí, M., Rudorff, N., Chowdhary, J., Dubovik, O., Hostetler, C., Hu, Y., Jamet, C., Knobelspiesse, K., Lehahn, Y., Litvinov, P., Sayer, A. M., Ward, B., Boss, E., Koren, I., and Miller, L. A.: Harnessing remote sensing to address critical science questions on ocean-atmosphere interactions, *Elementa: Science of the Anthropocene*, 6, [10.1525/elementa.331](https://doi.org/10.1525/elementa.331), 2018.

Painemal, D., Corral, A. F., Sorooshian, A., Brunke, M. A., Chellappan, S., Afzali Gorooh, V., Ham, S.-H., O'Neill, L., Smith Jr., W. L., Tselioudis, G., Wang, H., Zeng, X., and Zuidema, P.: An Overview of Atmospheric Features Over the Western North Atlantic Ocean and North American East Coast—Part 2: Circulation, Boundary Layer, and Clouds, *Journal of Geophysical Research: Atmospheres*, 126, e2020JD033423, <https://doi.org/10.1029/2020JD033423>, 2021.

Painemal, D., Chellappan, S., Smith Jr., W. L., Spangenberg, D., Park, J. M., Ackerman, A., Chen, J., Crosbie, E., Ferrare, R., Hair, J., Kirschler, S., Li, X.-Y., McComiskey, A., Moore, R. H., Sanchez, K., Sorooshian, A., Tornow, F., Voigt, C., Wang, H., Winstead, E., Zeng, X., Ziemba, L.,

and Zuidema, P.: Wintertime Synoptic Patterns of Midlatitude Boundary Layer Clouds Over the Western North Atlantic: Climatology and Insights From In Situ ACTIVATE Observations, *Journal of Geophysical Research: Atmospheres*, 128, e2022JD037725, <https://doi.org/10.1029/2022JD037725>, 2023.

Paiva, V., Kampel, M., and Camayo, R.: Comparison of Multiple Surface Ocean Wind Products with Buoy Data over Blue Amazon (Brazilian Continental Margin), *Advances in Meteorology*, 2021, 6680626, 10.1155/2021/6680626, 2021.

Palm, S. P., Hagan, D., Schwemmer, G., and Melfi, S. H.: Inference of Marine Atmospheric Boundary Layer Moisture and Temperature Structure Using Airborne Lidar and Infrared Radiometer Data, *Journal of Applied Meteorology*, 37, 308-324, <https://doi.org/10.1175/1520-0450-37.3.308>, 1998.

Papadimas, C. D., Hatzianastassiou, N., Matsoukas, C., Kanakidou, M., Mihalopoulos, N., and Vardavas, I.: The direct effect of aerosols on solar radiation over the broader Mediterranean basin, *Atmos. Chem. Phys.*, 12, 7165-7185, 10.5194/acp-12-7165-2012, 2012.

Petters, M. D. and Kreidenweis, S. M.: A single parameter representation of hygroscopic growth and cloud condensation nucleus activity, *Atmos. Chem. Phys.*, 7, 1961-1971, 10.5194/acp-7-1961-2007, 2007.

Pistone, K., Redemann, J., Doherty, S., Zuidema, P., Burton, S., Cairns, B., Cochrane, S., Ferrare, R., Flynn, C., Freitag, S., Howell, S. G., Kacenelenbogen, M., LeBlanc, S., Liu, X., Schmidt, K. S., Sedlacek Iii, A. J., Segal-Rozenhaimer, M., Shinozuka, Y., Stamnes, S., van Diedenhoven, B., Van Harten, G., and Xu, F.: Intercomparison of biomass burning aerosol optical properties from in situ and remote-sensing instruments in ORACLES-2016, *Atmos. Chem. Phys.*, 19, 9181-9208, 10.5194/acp-19-9181-2019, 2019.

Prytherch, J. and Yelland, M. J.: Wind, Convection and Fetch Dependence of Gas Transfer Velocity in an Arctic Sea-Ice Lead Determined From Eddy Covariance CO₂ Flux Measurements, *Global Biogeochemical Cycles*, 35, e2020GB006633, <https://doi.org/10.1029/2020GB006633>, 2021.

Quinn, P. K., Bates, T. S., Coffman, D. J., Upchurch, L., Johnson, J. E., Moore, R., Ziemba, L., Bell, T. G., Saltzman, E. S., Graff, J., and Behrenfeld, M. J.: Seasonal Variations in Western North Atlantic Remote Marine Aerosol Properties, *Journal of Geophysical Research: Atmospheres*, 124, 14240-14261, <https://doi.org/10.1029/2019JD031740>, 2019.

Reid, J. S., Jonsson, H. H., Smith, M. H., and Smirnov, A.: Evolution of the vertical profile and flux of large sea-salt particles in a coastal zone, *Journal of Geophysical Research: Atmospheres*, 106, 12039-12053, <https://doi.org/10.1029/2000JD900848>, 2001.

Reid, J. S., Maring, H. B., Narisma, G. T., van den Heever, S., Di Girolamo, L., Ferrare, R., Lawson, P., Mace, G. G., Simpas, J. B., Tanelli, S., Ziemba, L., van Diedenhoven, B., Brientjes, R., Bucholtz, A., Cairns, B., Cambaliza, M. O., Chen, G., Diskin, G. S., Flynn, J. H., Hostetler, C. A., Holz, R. E., Lang, T. J., Schmidt, K. S., Smith, G., Sorooshian, A., Thompson, E. J., Thornhill, K. L., Trepte, C., Wang, J., Woods, S., Yoon, S., Alexandrov, M., Alvarez, S., Amiot, C. G., Bennett, J. R., Brooks, M., Burton, S. P., Cayanan, E., Chen, H., Collow, A., Crosbie, E., DaSilva, A., DiGangi, J. P., Flagg, D. D., Freeman, S. W., Fu, D., Fukada, E., Hilario, M. R. A., Hong, Y., Hristova-Veleva, S. M., Kuehn, R., Kowch, R. S., Leung, G. R., Loveridge, J., Meyer, K., Miller, R. M., Montes, M. J., Moum, J. N., Nenes, A., Nesbitt, S. W., Norgren, M., Nowottnick, E. P., Rauber, R. M., Reid, E. A., Rutledge, S., Schlosser, J. S., Sekiyama, T. T., Shook, M. A., Sokolowsky, G. A., Stamnes, S. A., Tanaka, T. Y., Wasilewski, A., Xian, P., Xiao, Q., Xu, Z., and Zavaleta, J.: The Coupling Between Tropical Meteorology, Aerosol Lifecycle, Convection, and Radiation during the Cloud, Aerosol and Monsoon Processes Philippines Experiment (CAMP2Ex), *Bulletin of the American Meteorological Society*, 104, E1179-E1205, <https://doi.org/10.1175/BAMS-D-21-0285.1>, 2023.

Ricker, W. E.: Linear Regressions in Fishery Research, *Journal of the Fisheries Research Board of Canada*, 30, 409-434, 10.1139/f73-072, 1973.

Sawamura, P., Moore, R. H., Burton, S. P., Chemyakin, E., Müller, D., Kolgotin, A., Ferrare, R. A., Hostetler, C. A., Ziemba, L. D., Beyersdorf, A. J., and Anderson, B. E.: HSRL-2 aerosol optical measurements and microphysical retrievals vs. airborne in situ measurements during DISCOVER-AQ 2013: an intercomparison study, *Atmos. Chem. Phys.*, 17, 7229-7243, 10.5194/acp-17-7229-2017, 2017.

Scarino, A. J., Obland, M. D., Fast, J. D., Burton, S. P., Ferrare, R. A., Hostetler, C. A., Berg, L. K., Lefer, B., Haman, C., Hair, J. W., Rogers, R. R., Butler, C., Cook, A. L., and Harper, D. B.: Comparison of mixed layer heights from airborne high spectral resolution lidar, ground-based measurements, and the WRF-Chem model during CalNex and CARES, *Atmos. Chem. Phys.*, 14, 5547-5560, 10.5194/acp-14-5547-2014, 2014.

Schlosser, J. S., Dadashazar, H., Edwards, E.-L., Hossein Mardi, A., Prabhakar, G., Stahl, C., Jonsson, H. H., and Sorooshian, A.: Relationships Between Supermicrometer Sea Salt Aerosol and Marine Boundary Layer Conditions: Insights From Repeated Identical Flight Patterns, *Journal of Geophysical Research: Atmospheres*, 125, e2019JD032346, <https://doi.org/10.1029/2019JD032346>, 2020.

Schlosser, J. S., Bennett, R., Cairns, B., Chen, G., Collister, B. L., Hair, J. W., Jones, M., Shook, M. A., Sorooshian, A., Thornhill, K. L., Ziemba, L. D., and Stamnes, S.: Maximizing the Volume of Collocated Data from Two Coordinated Suborbital Platforms, *Journal of Atmospheric and Oceanic Technology*, 41, 189-201, <https://doi.org/10.1175/JTECH-D-23-0001.1>, 2024.

Schlosser, J. S., Stamnes, S., Burton, S. P., Cairns, B., Crosbie, E., Van Diedenhoven, B., Diskin, G., Dmitrovic, S., Ferrare, R., Hair, J. W., Hostetler, C. A., Hu, Y., Liu, X., Moore, R. H., Shingler, T., Shook, M. A., Thornhill, K. L., Winstead, E., Ziemba, L., and Sorooshian, A.: Polarimeter + Lidar-Derived Aerosol Particle Number Concentration, *Frontiers in Remote Sensing*, 3, 10.3389/frsen.2022.885332, 2022.

GISS Research Scanning Polarimeter, last

Schulien, J. A., Behrenfeld, M. J., Hair, J. W., Hostetler, C. A., and Twardowski, M. S.: Vertically-resolved phytoplankton carbon and net primary production from a high spectral resolution lidar, *Opt. Express*, 25, 13577-13587, 10.1364/OE.25.013577, 2017.

Seethala, C., Zuidema, P., Edson, J., Brunke, M., Chen, G., Li, X.-Y., Painemal, D., Robinson, C., Shingler, T., Shook, M., Sorooshian, A., Thornhill, L., Tornow, F., Wang, H., Zeng, X., and Ziemba, L.: On Assessing ERA5 and MERRA2 Representations of Cold-Air Outbreaks Across the Gulf Stream, *Geophysical Research Letters*, 48, e2021GL094364, <https://doi.org/10.1029/2021GL094364>, 2021.

Sinclair, K., van Dierenhoven, B., Cairns, B., Alexandrov, M., Moore, R., Crosbie, E., and Ziemba, L.: Polarimetric retrievals of cloud droplet number concentrations, *Remote Sensing of Environment*, 228, 227-240, <https://doi.org/10.1016/j.rse.2019.04.008>, 2019.

Sorooshian, A., Corral, A. F., Braun, R. A., Cairns, B., Crosbie, E., Ferrare, R., Hair, J., Kleb, M. M., Hossein Mardi, A., Maring, H., McComiskey, A., Moore, R., Painemal, D., Scarino, A. J., Schlosser, J., Shingler, T., Shook, M., Wang, H., Zeng, X., Ziemba, L., and Zuidema, P.: Atmospheric Research Over the Western North Atlantic Ocean Region and North American East Coast: A Review of Past Work and Challenges Ahead, *Journal of Geophysical Research: Atmospheres*, 125, e2019JD031626, <https://doi.org/10.1029/2019JD031626>, 2020.

Sorooshian, A., Anderson, B., Bauer, S. E., Braun, R. A., Cairns, B., Crosbie, E., Dadashazar, H., Diskin, G., Ferrare, R., Flagan, R. C., Hair, J., Hostetler, C., Jonsson, H. H., Kleb, M. M., Liu, H., MacDonald, A. B., McComiskey, A., Moore, R., Painemal, D., Russell, L. M., Seinfeld, J. H., Shook, M., Smith, W. L., Thornhill, K., Tselioudis, G., Wang, H., Zeng, X., Zhang, B., Ziemba, L., and Zuidema, P.: Aerosol–Cloud–Meteorology Interaction Airborne Field Investigations: Using Lessons Learned from the U.S. West Coast in the Design of ACTIVATE off the U.S. East Coast, *Bulletin of the American Meteorological Society*, 100, 1511-1528, <https://doi.org/10.1175/BAMS-D-18-0100.1>, 2019.

Sorooshian, A., Alexandrov, M. D., Bell, A. D., Bennett, R., Betito, G., Burton, S. P., Buzanowicz, M. E., Cairns, B., Chemyakin, E. V., Chen, G., Choi, Y., Collister, B. L., Cook, A. L., Corral, A. F., Crosbie, E. C., van Dierenhoven, B., DiGangi, J. P., Diskin, G. S., Dmitrovic, S., Edwards, E. L., Fenn, M. A., Ferrare, R. A., van Gilst, D., Hair, J. W., Harper, D. B., Hilario, M. R. A., Hostetler, C. A., Jester, N., Jones, M., Kirschler, S., Kleb, M. M., Kusterer, J. M., Leavor, S., Lee, J. W., Liu, H., McCauley, K., Moore, R. H., Nied, J., Notari, A., Nowak, J. B., Painemal, D., Phillips, K. E., Robinson, C. E., Scarino, A. J., Schlosser, J. S., Seaman, S. T., Seethala, C., Shingler, T. J., Shook, M. A., Sinclair, K. A., Smith Jr, W. L., Spangenberg, D. A., Stamnes, S. A., Thornhill, K. L., Voigt, C., Vömel, H., Wasilewski, A. P., Wang, H., Winstead, E. L., Zeider, K., Zeng, X., Zhang, B., Ziemba, L. D., and Zuidema, P.: Spatially-coordinated airborne data and complementary products for aerosol, gas, cloud, and meteorological studies: The NASA ACTIVATE dataset, *ESSD*, 2023, 1-79, 10.5194/essd-2023-109, 2023.

Sorribas, M., Olmo, F. J., Quirantes, A., Lyamani, H., Gil-Ojeda, M., Alados-Arboledas, L., and Horvath, H.: Role of spheroidal particles in closure studies for aerosol microphysical–optical properties, *Quarterly Journal of the Royal Meteorological Society*, 141, 2700-2707, <https://doi.org/10.1002/qj.2557>, 2015.

Stamnes, S., Hostetler, C., Ferrare, R., Burton, S., Liu, X., Hair, J., Hu, Y., Wasilewski, A., Martin, W., van Diedenhoven, B., Chowdhary, J., Cetinić, I., Berg, L. K., Stamnes, K., and Cairns, B.: Simultaneous polarimeter retrievals of microphysical aerosol and ocean color parameters from the “MAPP” algorithm with comparison to high-spectral-resolution lidar aerosol and ocean products, *Appl. Opt.*, 57, 2394-2413, 10.1364/AO.57.002394, 2018.

Sun, K., Dai, G., Wu, S., Reitebuch, O., Baars, H., Liu, J., and Zhang, S.: Correlation between marine aerosol optical properties and wind fields over remote oceans with use of spaceborne lidar observations, *EGUsphere*, 2023, 1-34, 10.5194/egusphere-2023-433, 2023.

Tang, M., Zhang, H., Gu, W., Gao, J., Jian, X., Shi, G., Zhu, B., Xie, L., Guo, L., Gao, X., Wang, Z., Zhang, G., and Wang, X.: Hygroscopic Properties of Saline Mineral Dust From Different Regions in China: Geographical Variations, Compositional Dependence, and Atmospheric Implications, *Journal of Geophysical Research: Atmospheres*, 124, 10844-10857, 10.1029/2019jd031128, 2019.

Thornhill, K. L., Anderson, B. E., Barrick, J. D. W., Bagwell, D. R., Friesen, R., and Lenschow, D. H.: Air motion intercomparison flights during Transport and Chemical Evolution in the Pacific (TRACE-P)/ACE-ASIA, *Journal of Geophysical Research: Atmospheres*, 108, <https://doi.org/10.1029/2002JD003108>, 2003.

Tornow, F., Ackerman, A. S., Fridlind, A. M., Cairns, B., Crosbie, E. C., Kirschler, S., Moore, R. H., Painemal, D., Robinson, C. E., Seethala, C., Shook, M. A., Voigt, C., Winstead, E. L., Ziemba, L. D., Zuidema, P., and Sorooshian, A.: Dilution of Boundary Layer Cloud Condensation Nucleus Concentrations by Free Tropospheric Entrainment During Marine Cold Air Outbreaks, *Geophysical Research Letters*, 49, e2022GL098444, <https://doi.org/10.1029/2022GL098444>, 2022.

TSI, I.: Series 3080 Electrostatic Classifiers Operation and Service Manual, 2009.

TSI, I.: Laser Aerosol Spectrometer Model 3340 Operation and Service Manual, 2015.

Twomey, S. A., Piepgrass, M., and Wolfe, T. L.: An assessment of the impact of pollution on global cloud albedo, *Tellus B*, 36B, 356-366, <https://doi.org/10.1111/j.1600-0889.1984.tb00254.x>, 1984.

Uin, J.: Integrating Nephelometer Instrument Handbook, United States, Medium: ED; Size: 16 p., 10.2172/1246075, 2016.

van Diedenhoven, B., Hasekamp, O. P., Cairns, B., Schuster, G. L., Stammes, S., Shook, M. A., and Ziemba, L. D.: Remote sensing of aerosol water fraction, dry size distribution and soluble fraction using multi-angle, multi-spectral polarimetry, *EGUsphere*, 2022, 1-41, 10.5194/egusphere-2022-670, 2022.

Venkata, S. L. and Reagan, J. A.: Aerosol Retrievals from CALIPSO Lidar Ocean Surface Returns, *Remote Sensing*, 8, 1006, 2016.

Veselovskii, I., Dubovik, O., Kolgotin, A., Lapyonok, T., Di Girolamo, P., Summa, D., Whiteman, D. N., Mishchenko, M., and Tanré, D.: Application of randomly oriented spheroids for retrieval of dust particle parameters from multiwavelength lidar measurements, *Journal of Geophysical Research: Atmospheres*, 115, <https://doi.org/10.1029/2010JD014139>, 2010.

Virkkula, A., Ahlquist, N. C., Covert, D. S., Arnott, W. P., Sheridan, P. J., Quinn, P. K., and Coffman, D. J.: Modification, Calibration and a Field Test of an Instrument for Measuring Light Absorption by Particles, *Aerosol Science and Technology*, 39, 68-83, 10.1080/027868290901963, 2005.

Vömel, H. and Dunion, J.: Chapter 10 - Aircraft dropsonde campaigns, in: *Field Measurements for Passive Environmental Remote Sensing*, edited by: Nalli, N. R., Elsevier, 185-194, <https://doi.org/10.1016/B978-0-12-823953-7.00021-6>, 2023.

Vömel, H., Sorooshian, A., Robinson, C., Shingler, T. J., Thornhill, K. L., and Ziemba, L. D.: Dropsonde observations during the Aerosol Cloud meteorology Interactions over the western Atlantic Experiment, *Sci Data*, 10, 753, 10.1038/s41597-023-02647-5, 2023.

Vömel, H., Goodstein, M., Tudor, L., Witte, J., Fuchs-Stone, Ž., Sentić, S., Raymond, D., Martinez-Claros, J., Juračić, A., Maithel, V., and Whitaker, J. W.: High-resolution in situ observations of atmospheric thermodynamics using dropsondes during the Organization of Tropical East Pacific Convection (OTREC) field campaign, *Earth Syst. Sci. Data*, 13, 1107-1117, 10.5194/essd-13-1107-2021, 2021.

Voshchinnikov, N. V. and Farafonov, V. G.: Optical properties of spheroidal particles, *Astrophysics and Space Science*, 204, 19-86, 10.1007/BF00658095, 1993.

Wagner, R., Ajtai, T., Kandler, K., Lieke, K., Linke, C., Müller, T., Schnaiter, M., and Vragel, M.: Complex refractive indices of Saharan dust samples at visible and near UV wavelengths: a laboratory study, *Atmos. Chem. Phys.*, 12, 2491-2512, 10.5194/acp-12-2491-2012, 2012.

Whitlock, C. H., Bartlett, D. S., and Gurganus, E. A.: Sea foam reflectance and influence on optimum wavelength for remote sensing of ocean aerosols, *Geophysical Research Letters*, 9, 719-722, 1982.

Wiedensohler, A., Birmili, W., Putaud, J.-P., and Ogren, J.: Recommendations for Aerosol Sampling, in: *Aerosol Science*, 45-59, <https://doi.org/10.1002/9781118682555.ch3>, 2013.

Wilson, J. C. and Jonsson, H.: Measurement of Cloud and Aerosol Particles from Aircraft, in: *Aerosol Measurement*, 655-665, <https://doi.org/10.1002/9781118001684.ch29>, 2011.

Wu, C. and Yu, J. Z.: Evaluation of linear regression techniques for atmospheric applications: the importance of appropriate weighting, *Atmos. Meas. Tech.*, 11, 1233-1250, 10.5194/amt-11-1233-2018, 2018.

Wu, J.: Mean square slopes of the wind-disturbed water surface, their magnitude, directionality, and composition, *Radio Science*, 25, 37-48, <https://doi.org/10.1029/RS025i001p00037>, 1990.

Wu, L., Hasekamp, O., van Diedenhoven, B., and Cairns, B.: Aerosol retrieval from multiangle, multispectral photopolarimetric measurements: importance of spectral range and angular resolution, *Atmos. Meas. Tech.*, 8, 2625-2638, 10.5194/amt-8-2625-2015, 2015.

Zieger, P., Fierz-Schmidhauser, R., Weingartner, E., and Baltensperger, U.: Effects of relative humidity on aerosol light scattering: results from different European sites, *Atmos. Chem. Phys.*, 13, 10609-10631, 10.5194/acp-13-10609-2013, 2013.

Zieger, P., Väisänen, O., Corbin, J. C., Partridge, D. G., Bastelberger, S., Mousavi-Fard, M., Rosati, B., Gysel, M., Krieger, U. K., Leck, C., Nenes, A., Riipinen, I., Virtanen, A., and Salter, M. E.: Revising the hygroscopicity of inorganic sea salt particles, *Nature Communications*, 8, 15883, 10.1038/ncomms15883, 2017.